Super-Gaussian Transport Theory and Field Generating Instability in Laser-Plasmas

Contact *j.bissell07@imperial.ac.uk*

J. J. Bissell and R. J. Kingham

Blackett Laboratory
Imperial College London
SW7 2BZ

1 Introduction

Accurate prediction of plasma transport is essential to the success of long-pulse (100ps-10ns) experiments, such as those at the National Ignition Facility in the United States.[i] Transport is commonly modelled using magnetohydrodynamics (MHD) - an approach based on the fluid equations and closed using Braginskii's classical transport theory, i.e., assuming that the electron distribution function is close to a Gaussian.[ii,iii,iv] However, for laser intensities in the range 10^{14}-10^{15}Wcm^{-2} (typical of long-pulse experiments), heating is dominated by inverse bremsstrahlung, and this mechanism tends to distort the distribution function away from a Gaussian by preferentially transmitting energy to slower, more collisional electrons. In fact, the distribution function f_0 tends to a super-Gaussian; that is, $f_0(v)\propto\exp[-(v/\alpha_e v_T)^m]$, where v is the electron velocity, $m\in[2,5]$, α_e is a function of m, and $v_T=(2T_e/m_e)^{1/2}$ is the thermal velocity, with T_e and m_e as the electron temperature and mass respectively.[v,vi] Notice that when m=2 we recover the usual Gaussian form. The super-Gaussian power m is calculated from the ion atomic number Z and the electron quiver velocity $v_{osc.}$ using the formula of Matte *et al.*,[vi]

$$m = 2 + \frac{3}{1+1.66/a_M^{\,0.724}}, \quad \text{where} \quad a_M = Z(v_{osc.}/v_T)^2. \qquad (1)$$

Recently, Ridgers *et al.* have shown that a super-Gaussian may be used as the basis for re-deriving the transport theory, and gave expressions for the electric field **E** and heat-flow **q** to account for I.B. effects in fluid codes, thus mitigating the need for expensive kinetic calculations.[vii] Ridgers's modified transport equations are

$$en_e\mathbf{E} = -\underline{\underline{\gamma^c}}\cdot\nabla P_e + \mathbf{j}\times\mathbf{B} + \frac{m_e}{e\tau_B}\underline{\underline{\alpha^c}}\cdot\mathbf{j} - n_e\underline{\underline{\beta^c}}\cdot\nabla T_e \qquad (2)$$

and

$$\mathbf{q} = -\frac{n_e\tau_B T_e}{m_e}\underline{\underline{\kappa^c}}\cdot\nabla T_e - \underline{\underline{\psi'}}\cdot\mathbf{j}\frac{T_e}{e} - \frac{\tau_B T_e}{m_e}\underline{\underline{\phi^c}}\cdot\nabla P_e, \qquad (3)$$

where e is the electronic charge, n_e is the electron number density, $P_e=n_eT_e$ is the isotropic pressure, **j** is the current, **B** is the magnetic field flux-density and $\tau_B=c_B\tau_T$ is the Braginkii collision time, which is proportional to the thermal collision time $\tau_T=(4\pi v_T^3)/(n_i[Ze^2/\varepsilon_0 m_e]^2\log\Lambda_{ei})$ by the factor $c_B=3\pi^{1/2}/4$, where n_i is the ion number density, ε_0 is the permittivity of free space and $\log\Lambda_{ei}\approx 8$ is the Coulomb logarithm. Ridgers used the Lorentz approximation, so the transport coefficients $\underline{\underline{\alpha^c}}$, $\underline{\underline{\beta^c}}$, $\underline{\underline{\kappa^c}}$, $\underline{\underline{\psi^c}}=(\underline{\underline{\psi'}}-[5/2]\underline{\underline{\mathbf{I}}})$, $\underline{\underline{\gamma^c}}$ and $\underline{\underline{\phi^c}}$ are dimensionless functions of both m and the Hall Parameter $\chi=\omega_L\tau_B$ only, where $\omega_L=(e|\mathbf{B}|/m_e)$ is the electron thermal Larmor frequency.[vii] Note that classical transport theory, for which $\underline{\underline{\beta^c}}=\underline{\underline{\psi^c}}$ and $\underline{\underline{\gamma^c}}=\underline{\underline{\phi^c}}=\underline{\underline{\mathbf{I}}}$ (the identity tensor), is recovered when m=2. The resistivity $\underline{\underline{\alpha^c}}$, conductivity $\underline{\underline{\kappa^c}}$, and thermoelectric tensors $\underline{\underline{\beta^c}}$ and $\underline{\underline{\psi^c}}$ may thus be termed `old' coefficients, whose values are modified depending on the super-Gaussian power $m$, while $\underline{\underline{\gamma^c}}$ and $\underline{\underline{\phi^c}}$ are `new' coefficients describing novel I.B. effects. The magnetic field provides a natural reference direction for the transport so that a general coefficient $\underline{\underline{\eta}}$ may be written in terms of three components $\eta_\perp$, $\eta_\parallel$ and $\eta_\wedge$, *viz*

$$\underline{\underline{\eta}} = \eta_\parallel\mathbf{b}(\mathbf{b}\cdot\mathbf{s}) + \eta_\perp\mathbf{b}\times(\mathbf{s}\times\mathbf{b}) + \eta_\wedge\mathbf{b}\times\mathbf{s}, \qquad (4)$$

where $\mathbf{b}=\mathbf{B}/|\mathbf{B}|$ is a unit vector in the direction of the magnetic field and **s** is the driving force behind the transport. Convention dictates that in the case of the resistivity $\underline{\underline{\alpha^c}}$, for which the driving force is $\mathbf{s}=\mathbf{j}$, the final term in this expression takes a negative rather than positive sign. Note that only the $\eta_\perp$ components are unique $\eta_\wedge$, because $\eta_\parallel=\eta_\perp(\chi=0)$.[iii,iv,vii]

Ridgers demonstrated the applicability of the super-Gaussian transport theory, and noted modifications to the `old' coefficients; however, he did not consider the implications of the new terms.[vii] Consequently, the first part of this report is devoted to an exploration of some of the ways super-Gaussians might be expected to modify transport in magnetized plasmas. We shall show that the addition of `new' coefficients has two principle consequences: first, the suppression of traditional transport phenomena; and second, the introduction of new effects. Indeed, we shall demonstrate that transport is strongly affected by super-Gaussian effects in the limit of low χ, suggesting that the theory may be most relevant to the seeding and evolution of magnetic fields in otherwise un-magnetized conditions. For this reason, later sections are devoted to a discussion of its consequences for the well-known field generating thermal instability.[viii,ix,x]

2 Super-Gaussian Effects in the Induction Equation

Using the chain rule to write $\nabla P_e=n_e\nabla T_e+T_e\nabla n_e$, the consequences of the $\underline{\underline{\gamma^c}}$ coefficient may be considered by looking at its contribution to the induction equation, found after substituting equation (2) into Faraday's Law, i.e.,

$$\frac{\partial\mathbf{B}}{\partial t} = -\nabla\times\mathbf{E} = \nabla\times\left[\frac{T_e\underline{\underline{\gamma^c}}}{en_e}\cdot\nabla n_e - \mathbf{j}\times\mathbf{B} - \frac{m_e\underline{\underline{\alpha^c}}}{e^2 n_e\tau_B}\cdot\mathbf{j} + \left(\underline{\underline{\beta^c}}+\underline{\underline{\gamma^c}}\right)\frac{\nabla T_e}{e}\right]. \qquad (5)$$

The final term in this equation represents the Nernst effect,[xi] that is, advection of the magnetic field down temperature gradients. Retaining just this term, applying the expansion of equation (4), and keeping only the cross-field parts, we find

$$\frac{\partial\mathbf{B}}{\partial t} = \nabla\times(\mathbf{v}_N\times\mathbf{B}), \quad \text{where} \quad \mathbf{v}_N = -\frac{c_B}{2\chi}\frac{\lambda_T^{\,2}}{\tau_B}(\beta_\wedge+\gamma_\wedge)\frac{\nabla T_e}{T_e} \qquad (6)$$

is the Nernst advection velocity and $\lambda_T=v_T\tau_T$ is the thermal mean-free-path (c.f. A. Nishiguchi *et al.*[xi]). The $\beta_\wedge$ coefficient (which is positive) is reduced in the super-Gaussian theory; however, because $\gamma_\wedge$ is negative, the Nernst velocity is further suppressed by the new coefficient. Indeed, for the case where m=5, when $\gamma_\wedge$ is of a similar order to $\beta_\wedge$, we see as much as a five-fold reduction in the Nernst velocity $\mathbf{v}_N$ in the low χ limit (see figure 1).

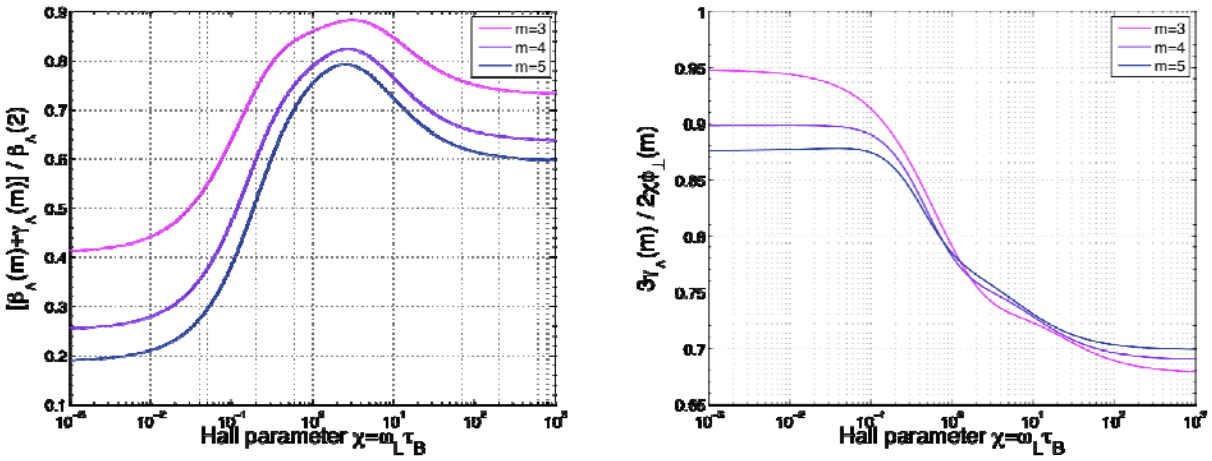

Fig. 1: Suppression of the Nernst effect (left-hand plot) visualised by plotting $[\beta_\wedge(m)+\gamma_\wedge(m)]/\beta_\wedge(2)$ as a function of χ for different values of super-Gaussian power m. Notice that the ratio is 0.2 in the limit of low χ implying suppression by a factor of five. The right-hand plot shows the ratio $3\gamma_\wedge/2\chi\phi_\perp$ as a function of χ and suggests an interpretation for the new advection effect described later (see discussion of $\underline{\underline{\phi}}^c$ coefficient).

For a Cartesian x-y geometry, with perpendicular fields $\mathbf{B}=B\mathbf{z}$ such that $\mathbf{B}\cdot\nabla f=\mathbf{B}\cdot\mathbf{A}=0$ for scalar and vector quantities f and $\mathbf{A}$ respectively, the contribution to the electric field from terms in $\underline{\underline{\gamma}}^c\cdot\nabla n_e$ is

$$-\mathbf{E}=\frac{\gamma_\perp T_e}{en_e}\nabla n_e-\frac{\gamma_\wedge T_e}{en_e}\nabla n_e\times\mathbf{b}. \qquad (7)$$

Taking the curl of the first term on the right-hand-side, and neglecting gradients in $\gamma_\perp$ we thus have a new expression for magnetic field generation due to $\nabla T_e\times\nabla n_e$, i.e.,

$$\frac{\partial\mathbf{B}}{\partial t}=\gamma_\perp\frac{\nabla T_e\times\nabla n_e}{en_e}, \qquad (8)$$

(c.f. M. G. Haines[xii]). For super-Gaussian power m=5, $\gamma_\perp\in[0.7,1.0]$, and the new coefficient thus suppresses magnetic field generation by as much as ~30%.

Furthermore, taking the curl of the second term we have

$$\frac{\partial\mathbf{B}}{\partial t}=\nabla\times(\mathbf{v}_\gamma\times\mathbf{B}),\quad\text{where}\quad\mathbf{v}_\gamma=-\frac{c_B}{2\chi}\frac{\lambda_T^{\,2}}{\tau_B}\gamma_\wedge\frac{\nabla n_e}{n_e}, \qquad (9)$$

that is, an advection equation with advection velocity $\mathbf{v}_\gamma$, a phenomena that shall be referred to as the gamma advection effect. This novel advection phenomena is directly analogous to the Nernst effect described above; however, in this case, because $\gamma_\wedge$ is negative, advection by $\mathbf{v}_\gamma\propto\nabla n_e$ is in the direction of increasing density. A physical interpretation of this is found by considering the super-Gaussian modifications to the heat-flow equation, and it is to this that we now turn.

3 Super-Gaussian Heat-Flow Effects

Neglecting Ohmic heating, the energy equation may be written

$$\frac{3}{2}\frac{\partial(n_eT_e)}{\partial t}+\nabla\cdot\mathbf{q}=\dot{U}_L, \qquad (10)$$

where the term on the right-hand-side represents the rate of change of internal energy due to laser heating. Terms in the heat-flow equation may thus be interpreted by considering the rate of change of energy due to the divergence of the flux $\mathbf{q}$. This means that the conductivity term in $\underline{\underline{\kappa}}^c$ describes thermal diffusion, through the term in $\kappa_\perp$, and a flux of energy perpendicular to both the magnetic field and temperature gradients ∇T_e, through the term in $\kappa_\wedge$. This latter effect is called the Righi-Leduc heat-flow, and is responsible for driving the field generating thermal instability mentioned in the introduction.[viii,ix,x]

By expanding terms in the pressure gradient, as we did when discussing the Nernst effect we find

$$\mathbf{q}=-\frac{n_e\tau_BT_e}{m_e}\left(\underline{\underline{\kappa}}^c+\underline{\underline{\phi}}^c\right)\nabla T_e-\underline{\underline{\psi}}'\cdot\mathbf{j}\frac{T_e}{e}-\frac{\tau_BT^2{}_e}{m_e}\underline{\underline{\phi}}^c\cdot\nabla n_e. \qquad (11)$$

Consequently, the new $\underline{\underline{\phi}}^c$ coefficient may be thought of as having two effects: first, it modifies the traditional conductivity so that $\underline{\underline{\kappa}}^c\rightarrow\underline{\underline{\kappa}}^c+\underline{\underline{\phi}}^c$; and second, it introduces a new heat flow term described by

$$\mathbf{q}=\mathbf{q}_n-\frac{\tau_BT^2{}_e}{m_e}\phi_\wedge\mathbf{b}\times\nabla n_e,\quad\text{where}\quad\mathbf{q}_n=-\frac{\tau_BT^2{}_e}{m_e}\phi_\perp\nabla n_e. \qquad (12)$$

The $\underline{\underline{\phi}}^c$ coefficient is made up of negative components (unlike $\underline{\underline{\kappa}}^c$ which is positive) so that its introduction leads to suppression of both thermal diffusion, by up to ~80%, and the Righi-Leduc heat-flow, by up to ~90% (see figure 2).

The heat-flow $\mathbf{q}_n$ associated with $\phi_\perp$ also has consequences for plasma transport, and provides us with a physical picture for interpreting the new gamma advection effect. Indeed, combining the definition $\mathbf{v}_\gamma$ in equation (9) with that $\mathbf{q}_n$ of in equation (12), we find

$$\mathbf{v}_\gamma=\frac{\gamma_\wedge}{\chi\phi_\perp}\frac{\mathbf{q}_n}{P_e}\approx\frac{2}{3}\frac{\mathbf{q}_n}{P_e}, \qquad (13)$$

where the approximate expression has been derived by noticing that $3\gamma_\wedge/2\chi\phi_\perp\approx1$ for all values of χ (see right-hand-plot in figure 1). Thus, the gamma advection effect represents advection of the magnetic field by the heat-flow associated with $\mathbf{q}_n$, in a fashion directly analogous to the heat-flow advection interpretation of the Nernst effect.[xi]

4 Summary of Super-Gaussian Transport Effects

In the previous sections we have seen that the super-Gaussian transport theory acts to suppress classical effects, especially in the case of strong inverse bremsstrahlung for which m=5. In addition, the extended theory introduces new phenomena. These effects may be summarised as follows:

- Suppression of the Nernst effect by up to ~80%.
- Suppression of the $\nabla T_e\times\nabla n_e$, source term by up to ~30%.
- Introduction of a novel advection effect in the direction ∇n_e.
- Suppression of the diffusive heat-flow by up to ~80%.
- Suppression of the Righi-Leduc heat-flow by up to ~90%.

In each of these cases, the classical transport effects are reduced most heavily in the limit of low χ.

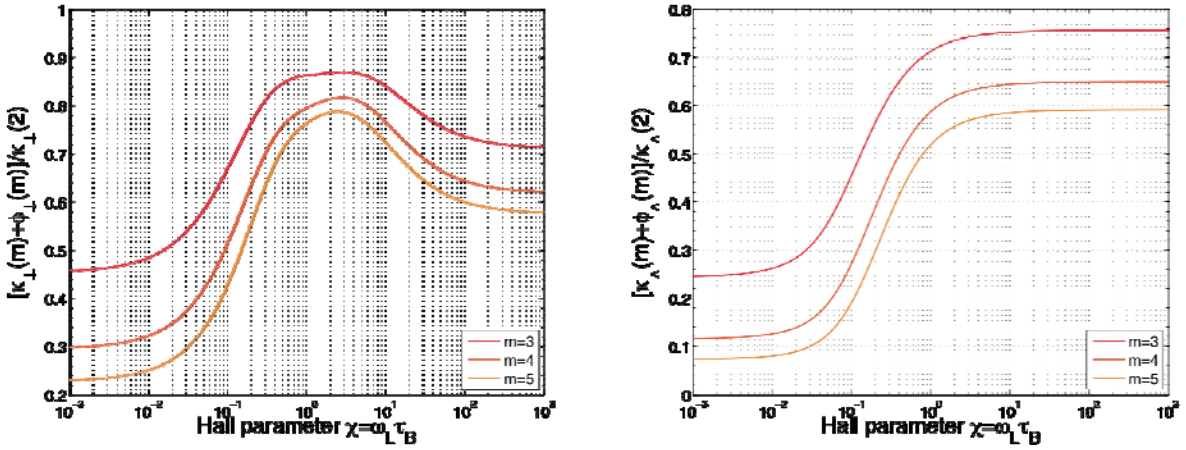

Fig. 2: Suppression of the diffusive conductivity (left-hand plot) and the Righi-Leduc heat-flow (right-hand plot) visualised by plotting the respective ratios $[\kappa_\perp(m)+\kappa_\perp(m)]/\kappa_\perp(2)$ and $[\kappa_\wedge(m)+\kappa_\wedge(m)]/\kappa_\wedge(2)$ against χ for different values of super-Gaussian power m. These plots indicate suppression of thermal diffusion by ~80% and the Righi-Leduc heat-flow by ~90% when m=5.

5 Field Generating Thermal Instability

The preceding summary emphasizes the particular relevance of super-Gaussian transport theory when magnetic fields are weak (low χ), suggesting that it may have important consequences for the seeding and evolution of magnetic fields in otherwise un-magnetized conditions. For this reason, the following sections are devoted to examining the impact of the theory on the field generating thermal instability mentioned in the introducion; a context in which the Righi-Leduc heat-flow and the $\nabla T_e\times\nabla n_e$ field generation mechanism, both suppressed by inverse bremsstrahlung, are essential.[viii,ix,x] Indeed, because the super-Gaussian theory predicts the reduction in magnitude of effects responsible for both the growth and damping of unstable waves, such an analysis is particularly useful as a means of assessing the combined impact of the theory.

Perturbation Analysis

After neglecting hydrodynamics, so that $\partial n_e/\partial t=0$, using Ampére's $\nabla\times\mathbf{B}=\mu_0\mathbf{j}$ to relate the magnetic field and the current, and substituting for the heat-flow in the energy equation, equations (5) and (10) provide a complete description of the temporal variation of the principle quantities T_e and $\mathbf{B}$. In zeroth-order we assume temperature and number density profiles of the form $T_0=T_0(x,t)$ and $n_e=n_e(x,t)$, so that the gradients of these quantities are along the x-axis of the system only. Consequently, we can define temperature and density length-scales, l_T and l_n respectively, such that

$$\frac{1}{l_T}=\frac{1}{T_0}\frac{\partial T_0}{\partial x} \quad \text{and} \quad \frac{1}{l_n}=\frac{1}{n_0}\frac{\partial n_0}{\partial x}. \tag{14}$$

In this way, we implicitly assume that the heating profile of the laser is also parallel to the x-axis. Finally, we assume that the plasma is un-magnetized, i.e., $\mathbf{B}_0=\mathbf{0}$. To the zeroth-order solutions we add wavelike perturbations with wavenumber k and frequency ω such that

$$T_e=T_0+\delta T\exp i(ky-\omega t) \quad \text{and} \quad \mathbf{B}=\delta B\exp i(ky-\omega t)\mathbf{z}, \tag{15}$$

where δT and δB are complex. Hence, assuming the local conditions $|kl_{T,n}|>>1$ and $\partial(l_{T,n}{}^{-1})/\partial x=0$, substituting the perturbed forms into the energy and induction equations, and subtracting the zeroth-order solutions, we find that to first-order

$$\Omega+D_T iK^2=-C_E\left(\frac{e\lambda_T{}^2}{\tau_T}\frac{\delta B}{\delta T}\right)K \tag{16}$$

and

$$\Omega+D_R iK^2-iN=C_I\left(\frac{\tau_T}{e\lambda_T{}^2}\frac{\delta T}{\delta B}\right)K, \tag{17}$$

where λ_T and τ_T are functions of the zeroth-order quanitites and we have made use of an additional set of dimensionless parameters defined by

$$\begin{aligned}
&\Omega=\omega\tau_T, \quad K=\lambda_T k, \quad D_T=\frac{c_B}{3}(\kappa_\parallel+\phi_\parallel), \quad D_R=\frac{\alpha_\parallel}{c_B\Lambda^2},\\
&\Lambda=\frac{\lambda_T}{\delta}, \quad C_E=\frac{c_B{}^2}{6L_T}\left(\frac{\partial(\kappa_\wedge+\phi_\wedge)}{\partial\chi}+\frac{L_T}{L_n}\frac{\partial\phi_\wedge}{\partial\chi}\right), \quad C_I=\frac{\gamma_\parallel}{L_n},\\
&N=N_\beta+N_\gamma, \quad N_\beta=\frac{c_B}{2}\frac{\partial(\beta_\wedge+\gamma_\wedge)}{\partial\chi}\frac{\lambda_T{}^2}{\tau_T T_0}\frac{\partial}{\partial x}\left(\tau_T\frac{\partial T_0}{\partial x}\right),\\
&N_\gamma=\frac{c_B}{2}\frac{\partial\gamma_\wedge}{\partial\chi}\frac{\lambda_T{}^2}{\tau_T n_0}\frac{\partial}{\partial x}\left(\tau_T\frac{\partial n_0}{\partial x}\right), \quad L_T=\frac{l_T}{\lambda_T} \quad \text{and} \quad L_n=\frac{l_n}{\lambda_T}.
\end{aligned} \tag{18}$$

Notice here that D_T and D_R represented the dimensionless thermal and resistive diffusion coefficients respectively, and that $\delta=c/\omega_{pe}$ is the collisionless skin-depth, where c is the speed of light and $\omega_{pe}=(n_e e^2/m_e\varepsilon_0)^{1/2}$ is the plasma frequency.

The coefficients C_E and C_I are coupling terms between the energy equation and induction equation respectively: C_E due to the Righi-Leduc heat-flow arising from the generated field, and C_I from $\nabla\delta T\times\nabla n_e$ field generation itself. Finally, the advection term N represents the combined effect of magnetic field advection by both the Nernst effect (denoted by N_β) and the new gamma advection effect (denoted N_γ). Eliminating δT and δB from equations (15) and (16), and solving the resultant quadratic in Ω, we arrive at the dispersion relation

$$\begin{aligned}
\Omega=\frac{i}{2}\Big\{&-\left[(D_T+D_R)K^2-N\right]\\
&\pm\sqrt{\left[(D_T+D_R)K^2-N\right]^2+4D_T K^2\left[D_R\left(K_s{}^2-K^2+N\right)\right]}\Big\},
\end{aligned} \tag{19}$$

where $K_s{}^2$ is a source term representing feedback between C_E and C_I, and is defined by

$$K_s{}^2=\frac{C_E C_I}{D_T D_R}=\frac{c_B{}^2\Lambda^2}{2\alpha_\parallel(\kappa_\parallel+\phi_\parallel)}\frac{\gamma_\parallel}{L_T L_n}\left(\frac{\partial(\kappa_\wedge+\phi_\wedge)}{\partial\chi}+\frac{L_T}{L_n}\frac{\partial\phi_\wedge}{\partial\chi}\right). \tag{20}$$

Notice that if we set m=2 we recover the relation of A. Hirao and M. Ogasawara, which itself reduces to that of Tidman and Shanny for N=0.[viii,x] The $K_s{}^2$ source term thus describes the original thermo-magnetic field generation mechanism (illustrated in figure 3), while the advection term N can enhance instability by laterally compressing the magnetic field.

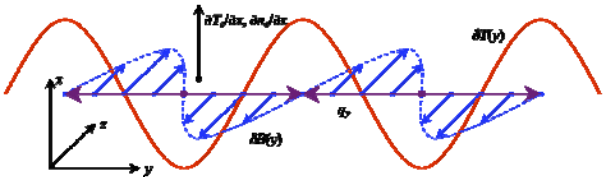

Fig. 3: The thermo-magnetic mechanism may be understood as follows: a temperature perturbation $\delta T(y)$ (red line) generates a magnetic field $\delta B(y)$ (blue arrows) by the $\nabla\delta T\times\nabla n_e$ mechanism. Since the Righi-Leduc heat-flow from the bulk temperature gradient (purple arrows) is given by $q_y=-\kappa_\wedge(\partial T_0/\partial x)(\delta B/|\delta B|)$, the alternating direction of $\delta B(y)$ periodically reverses q_y which then acts to magnify δT(y). In this physical picture δT and δB represent the real parts of their respective perturbations (see equation (15)).

Peak Growth Rates and Discussion

If the positive root is taken in equation (19), then instability prevails with growth-rate $\Gamma=\Im\{\Omega\}$ for those values of K obeying

$$K < K_c = \left(K_s^{\,2} + N/D_R\right)^{1/2}, \qquad (21)$$

where K_c is the cut-off wave-number. In addition, exact expressions may be found for the peak wave-number K_M and growth-rate $\Gamma_M(K_M)$ by solving $\partial\Gamma/\partial K=0$. However, for most laser plasmas of interest $\Lambda>>1$, in which case the peak-growth rates may be approximated by[xiii]

$$\Gamma_M \approx D_R K_c^{\,2}, \quad \text{for} \quad K_s^{\,2} > 0 \qquad \text{and} \qquad \Gamma_M = N \quad \text{otherwise.} \qquad (22)$$

These expressions provide a useful means of exploring the impact of super-Gaussian distributions on the instability; however, before doing so it is necessary to define coefficients

$$b = \frac{L_T}{L_n}, \quad a = L_T^{\,2}\frac{\lambda_T^{\,2}}{T_0}\frac{\partial^2 T_0}{\partial x^2} \quad \text{and} \quad \lambda_n = \frac{l_n}{n_0}\frac{\partial^2 n_0}{\partial x^2}, \qquad (23)$$

since these must be supplied to the source terms prior to evaluation. We shall consider conditions similar to those found close to the wall of an Inertial Confinement Fusion (I.C.F.) hohlraum - an appropriate context two reasons: first, the laser irradiation is of an intensity ~2×10^{15}Wcm^{-2}, for which I.B. is the main heating mechanism; and second, the high atomic number of gold ablating from the wall (Z=79) makes the Lorentz approximation used to calculate the transport coefficients a good assumption.[vii] Using data taken from the I.C.F. review paper by Lindl *et al.*,[i] we take approximate values of the length-scales such that $a\in[-1,1]$, $b\in[-1,2]$ and $l_n/\lambda_n\approx2$.

Assuming $n_e\sim10^{21}$cm^{-3}, T_e~4-5keV, Z~79, l_T~3mm and $\log\Lambda_{ei}$~6, and using $b=-1$ and $a=0$, the classical theory of the instability ($m=2$) predicts growth-rates $\gamma_M=\tau_T\Gamma_M\sim0.4(ns)^{-1}$, implying that the field generating thermal instability can undergo many e-foldings over the duration of a 13.5ns ignition pulse.[i] However, for the laser intensities and wavelengths appropriate to I.C.F. hohlraum conditions, namely $I_l\sim2\times10^{15}$Wcm^{-2} and λ_l~351nm respectively,[i] Matte's formula of equation (1) predicts $3.0<m<3.5$. Accordingly calculations based on these larger values of m must be compared with those from the classical transport case.

The ratio of peak growth-rates $\gamma_M(m=3.5)/\gamma_M(m=2)$ is plotted in figure 4, a comparison indicating reduction in the voracity of the field-generating thermal instability by more than ~70% when super-Gaussian transport theory is used as the basis description. Furthermore, using this data, and the calculation from the previous paragraph, we find that the growth-rate when $m=3.5$, for $b=1$ and $a=0$, is $\gamma_M\sim0.1$(ns)$^{-1}$. In this case, we expect the instability to under go a single e-folding over a 13.5ns time-scale, rendering questionable its significance for the hohlraum conditions described. In fact, by further increasing the super-Gaussian power, so that $m\to5$, even greater suppression of the instability may be achieved.[xiii]

6 Conclusions

In the first half of this report we considered the impact of inverse bremsstrahlung (I.B.) on collisional transport phenomena. We showed that super-Gaussian effects, which arise as a result of strong I.B. heating, both suppresses traditional phenomena and introduces a new advection effect in the direction ∇n_e. This suppression is most pronounced in the limit of low Hall-Parameter, in which case the Nernst effect is reduced by a factor of five, the $\nabla T_e\times\nabla n_e$ field generation mechanism by ~30%, and the diffusive and Righi-Leduc heat-flows by ~80% and ~90% respectively.

Having established the importance of super-Gaussian transport theory in un-magnetized conditions we speculated that it be most important for describing the seeding and evolution of magnetic field. Consequently, in the second half of this report we explored its consequences for the well-known field-generating thermal instability.[viii,ix,x] Indeed, making approximate calculations based on conditions in an I.C.F. hohlraum, we concluded that super-Gaussian effects strongly suppress the instability, by more than ~70%. This is presumably good news for I.C.F. fusion experiments, since it would appear possible to inhibit the spontaneous generation of large magnetic fields by increasing the strength of I.B. heating.[xiv] We hope to assess the consequences for other transport instabilities, such as the field compressing magnetothermal instability,[xv] as future work.

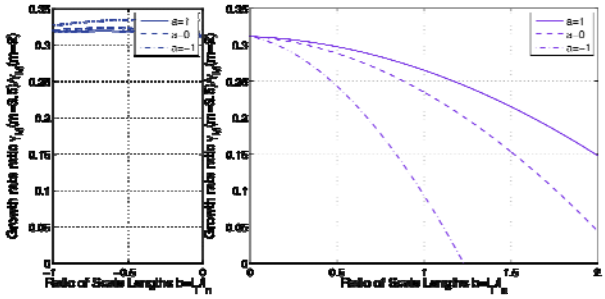

Fig. 4: The ratio $\gamma_M(m=3.5)/\gamma_M(m=2)$ plotted as a function of $b=l_T/l_n$ for different values of $a=(l_T^{\,2}/T_0)(\partial^2T_0/\partial x^2)$. The left-hand and right-hand plots correspond to the approximations for $\Gamma_M=\gamma_M\tau_T$ given in equation (22). Both indicate suppression of the field generating thermal instability by more than ~70%.

Acknowledgements

J. J. Bissell would like to acknowledge useful discussions with C. P. Ridgers regarding material in sections 2 and 3.

References

[i] Lindl *et al.*, *Phys Plas.* **11**, 339 (2004)
[ii] Braginskii, *Rev. Plas. Phys* **1,** (1965), p. 205
[iii] E. M. Epperlein, *J. Phys. D* **17**, 1823, (1984)
[iv] E. M. Epperlein and M. G. Haines, *Phys. Fluids* **29**, 1029 (1986)
[v] A. B. Langdon, *Phys Rev. Lett.* **44**, 575 (1980)
[vi] J. P. Matte *et al.*, *Plas. Phys Contrl Fus.* **30**, 1665 (1988)
[vii] C. P. Ridgers *et al.*, *Phys Plas.* **15**, 092311 (2008)
[viii] D. A. Tidman and R.A. Shanny, *Phys Fluids* **17**, p. 1207 (1974)
[ix] L. A. Bol'shov *et al.*, *JETP Lett.* **19**, p. 168 (1974)
[x] A. Hirao and M. Ogasawara, *J. Phys, Soc. Jap.* **50**, p. 668 (1981)
[xi] A. Nishiguchi, *et al.*, *Phys Fluids*, **28,** p. 3683 (1985)
[xii] M. G. Haines, *Can. J. Phys* **64**, p. 912 (1986)
[xiii] J.J. Bissell, *Draft Ph.D. Thesis*, Imperial College (2011)
[xiv] S. H. Glenzer *et al.*, *Phys. Plasmas* **6**, 2117 (1999)
[xv] J.J. Bissell *et al.*, *Phys Rev. Lett.* **105**, 175001 (2010)

High-field electrodynamics in plasmas

Contact *d.burton@lancaster.ac.uk*

DA Burton
Department of Physics, Lancaster University
& The Cockcroft Institute, Daresbury, UK

H Wen
Department of Physics, Lancaster University
& The Cockcroft Institute, Daresbury, UK

Classical vacuum Maxwellian electrodynamics is a linear theory, and non-linearities arise only via the coupling of electromagnetic fields and matter. Although non-linear theories of electrodynamics may be induced from vacuum persistence amplitudes in QED [1], the origin of the non-linearity may be understood as the coupling of the electromagnetic field to virtual electron-positron pairs. Unlike gauge fields associated with a non-Abelian gauge group, the electromagnetic field described by Maxwellian electrodynamics does not fundamentally couple to itself.

Born-Infeld electrodynamics has attracted considerable attention over recent years. It was originally introduced in the 1930s [2] in an attempt to describe the classical electron entirely in terms of its electromagnetic field. Born was driven by the desire to develop a quantum theory of electrodynamics that avoided the divergences that plagued QED at that time; by introducing a fundamentally non-linear classical theory of electromagnetism, he began by eliminating the Coulomb singularity in the electric field of a classical point charge at rest. Born's long-term goal was to quantize his non-linear classical field theory; however, this proved to be an extremely difficult task and he never fulfilled his ambition. Moreover, a workable scheme was developed for handling the divergences in QED order-by-order within perturbation theory, and the development of perturbative renormalization techniques led to some of the most spectacular triumphs of modern physics (for example, the recent determination of the inverse α^{-1} of the fine structure constant to less than one part per billion [3]). Thus, interest in Born's work waned; however, during the first superstring revolution in the mid-1980s it was shown that Born-Infeld-type theories are a feature of low energy string field theory [4], and this discovery led to the recent resurgence of interest in Born-Infeld electrodynamics [5–10].

Furthermore, among the family of non-linear generalizations of Maxwellian electrodynamics, it has long been known that Born-Infeld theory possesses a number of highly attractive features; in particular, like the vacuum Maxwell equations, the Born-Infeld equations exhibit zero birefringence and its solutions have exceptional causal behaviour [11, 12]. The vacuum Maxwell and Born-Infeld field equations are the only physical theories with a single light cone obtainable from a local Lagrangian constructed solely from the two Lorentz invariants associated with the electromagnetic field strength tensor and the metric tensor. Hence, the phase speed of a Born-Infeld electromagnetic plane wave in the vacuum is independent of its polarization.

Any self-consistent theory describing a large collection of charged particles must include all electromagnetic forces between the particles. However, the notorious problem of determining the classical force on a single accelerating point charge due to its own electromagnetic field has stimulated research for over a century and remains unresolved. The structure of an isolated single electron is currently beyond observation and one often proceeds classically by associating the electron with a singularity in the electromagnetic field described by Maxwell's equations in vacuo. Following Dirac [13], an equation of motion for the electron may be obtained by appealing to conservation of the total energy-momentum of the electron and its electromagnetic field (see Ref. 14 for a recent discussion). In order to remove singularities in the equation of motion, Dirac made "natural assumptions" about the origin of the electron mass. The resulting Lorentz-Dirac equation of motion contains *third* order proper time derivatives of the electron's world line, and possesses solutions that violate intuition. In particular, unless special conditions are adopted for the final state of the electron, it predicts that a free electron in vacuo can self-accelerate; furthermore the equations possess solutions in which the electron experiences a sudden acceleration before it enters a region of space containing a non-vanishing external electrostatic field (see Ref. 15 for a recent discussion).

The search for a complete dynamical theory of a point charge within Born-Infeld electrodynamics is ongoing [16], and this theory is expected to provide a resolution to the radiation-reaction problem. In particular, the difficulties associated with the Lorentz-Dirac equation are thought to have their origin in the electron's singular total mass-energy in classical Maxwell electrodynamics; however, the electric field of a Born-Infeld electron at rest is non-singular and its total mass-energy is finite. Even so, this electric field is not differentiable at the electron, and it may be that a complete dynamical theory can only be found in the context of many-body theory [17].

Some of the most extreme conditions ever encountered in a terrestrial laboratory are created when high-power laser pulses interact with matter. The laser pulse immediately vaporizes the matter to form an intense laser-plasma providing novel avenues for generating in-

tense bursts of coherent electromagnetic radiation for a wide range of applications in biological and material science [18]. Furthermore, laser-plasmas permit controllable investigation of matter in extreme conditions that only occur naturally away from the Earth. It is expected that the next generation of ultra-intense lasers will, for the first time, allow controllable access to regimes where a host of different quantum electrodynamic phenomena will be evident. In particular, the challenge of extending Schwinger's classic analysis [1] of vacuum breakdown in a static external electric field to breakdown in an intense laser-plasma is ongoing [19]. However, the radiation-reaction problem is sufficiently strong motivation for exploring whether a Born-Infeld-type theory can yield experimental signatures *before* quantum effects become significant [8]. A sufficiently short and intense laser pulse propagating through a plasma may create a travelling longitudinal plasma wave whose phase velocity is approximately the same as the laser pulse's group velocity. However, it is not possible to sustain arbitrarily large electric fields; substantial numbers of plasma electrons become trapped in the wave and are accelerated, which dampens the wave (the wave 'breaks'). Early theoretical investigation of non-linear plasma waves was undertaken in the mid 1950s by Akhiezer and Polovin [20], and later expounded by Dawson [21] in the context of wave-breaking. Furthermore, this acceleration mechanism was recently employed [22] to explain the emission of energetic electrons from within the interiors of pulsars; such electrons are necessary for the formation of the electron-positron plasma populating a pulsar's magnetosphere.

Wave-breaking is a fundamentally non-linear phenomenon, and it is natural to explore the properties of Born-Infeld electrodynamics from this perspective [10]. Moreover, the magnetic fields found in neutron stars are typically $\sim 10^8$T, whilst those in magnetars may be two orders of magnitude higher and such fields have energy densities commensurate with the Schwinger limit (i.e. commensurate with a static electric field of strength $\sim 10^{18}$ V/m).

Our first steps in an investigation of collective phenomena in Born-Infeld electrodynamics have focussed on the behaviour of cold Born-Infeld plasmas [10].

1 Born-Infeld plasma

Unlike classical Maxwell theory, the electromagnetic field in classical Born-Infeld theory possesses a fundamental self-coupling which leads to a non-trivial vacuum polarization. The situation is analogous to Euler-Heisenberg electrodynamics [1], where the electromagnetic constitutive relations are non-linear; however, the origin of the non-linearity in the latter is the coupling of the electromagnetic field operator to the electron-positron field operator. In Born-Infeld theory the electric displacement $\mathbf{D}$ and magnetic field $\mathbf{H}$ are non-linear functions of the electric field $\mathbf{E}$ and magnetic induction $\mathbf{B}$ and have the form

$$\mathbf{D} = \varepsilon_0 \frac{\mathbf{E} + \kappa^2 c^2 (\mathbf{E}\cdot\mathbf{B})\mathbf{B}}{\sqrt{1 - \kappa^2(\mathbf{E}^2 - c^2\mathbf{B}^2) - \kappa^4 c^2 (\mathbf{E}\cdot\mathbf{B})^2}}, \quad (1)$$

$$\mathbf{H} = \frac{1}{\mu_0} \frac{\mathbf{B} - \kappa^2 (\mathbf{E}\cdot\mathbf{B})\mathbf{E}}{\sqrt{1 - \kappa^2(\mathbf{E}^2 - c^2\mathbf{B}^2) - \kappa^4 c^2 (\mathbf{E}\cdot\mathbf{B})^2}} \quad (2)$$

in the classical vacuum, where the self-coupling constant κ has dimensions [electric field]$^{-1}$. As usual, the fields $\mathbf{E}, \mathbf{B}, \mathbf{D}, \mathbf{H}$ satisfy

$$\nabla\cdot\mathbf{D} = \rho, \qquad \nabla\times\mathbf{H} = \mathbf{J} + \partial_t \mathbf{D}, \quad (3)$$

$$\nabla\cdot\mathbf{B} = 0, \qquad \nabla\times\mathbf{E} = -\partial_t \mathbf{B}. \quad (4)$$

Equations (1), (2), (3), (4), with $\rho = 0$ and $\mathbf{J} = 0$, may be induced from an action principle for which the Lagrangian is a Lorentz invariant expressed entirely in terms of the spacetime metric tensor and the electromagnetic 2-form constructed from $\mathbf{E}, \mathbf{B}$ (see, for example, Ref. 8).

In the following, the plasma electrons are modelled as a cold charged fluid satisfying the momentum balance law

$$\partial_t \mathbf{p} + (\mathbf{u}\cdot\nabla)\mathbf{p} = -e(\mathbf{E} + \mathbf{u}\times\mathbf{B}) \quad (5)$$

where $\mathbf{u}$ is the plasma electrons' bulk 3-velocity and $\mathbf{p} = m_e\mathbf{u}/\sqrt{1 - \mathbf{u}^2/c^2}$ is their bulk relativistic 3-momentum. The ion background is assumed to be uniform and static over the timescales of interest, and the electric charge density ρ and electric current density $\mathbf{J}$ are

$$\rho = \rho_0 + \rho_e, \qquad \mathbf{J} = \rho_e\,\mathbf{u} \quad (6)$$

where ρ_e is the bulk electron charge density and ρ_0 is the background ion charge density (a positive constant). As usual, $-e$ is the charge on the electron and m_e is the rest mass of the electron.

One way to motivate the field equations (1)-(6) is to use an action principle that exploits the notion of a "material" (or "body") manifold, each of whose points correspond to the worldline in spacetime of an idealized particle in the electron fluid [10].

1.1 Properties of linear waves

Before exploring the behaviour of non-linear waves, we comment on some of the properties of small amplitude waves in a cold magnetized Born-Infeld plasma.

Inspection of (1) reveals

$$\mathbf{D} = \varepsilon_0 \frac{\mathbf{E} + \kappa^2 c^2 (\mathbf{E}\cdot\mathbf{B})\mathbf{B}}{\sqrt{1 + \kappa^2 c^2 \mathbf{B}^2}} + \mathcal{O}(|\mathbf{E}|^2) \quad (7)$$

and hence small amplitude plane waves that oscillate parallel to a static and uniform background magnetic field (with magnitude B_0) satisfy

$$D = \varepsilon_0 \sqrt{1 + \kappa^2 c^2 B_0^2}\, E, \tag{8}$$

and the permittivity $\varepsilon_0 \sqrt{1 + \kappa^2 c^2 B_0^2}$ is seen to depend on B_0. It follows that the plasma frequency $\omega_p^{\rm BI}$ of a cold Born-Infeld plasma may be obtained from the usual plasma frequency ω_p of a cold Maxwell plasma by the replacement $\varepsilon_0 \to \varepsilon_0 \sqrt{1 + \kappa^2 c^2 B_0^2}$:

$$\omega_p^{\rm BI} = \omega_p (1 + \kappa^2 c^2 B_0^2)^{-\frac{1}{4}}. \tag{9}$$

Now consider a small amplitude electromagnetic plane wave propagating parallel to the background magnetic field. We linearize (1)-(6) about the fields $(\mathbf{E} = 0, \mathbf{B} = \mathbf{B}_0, \mathbf{u} = 0, \rho_e = -\rho_0)$ describing a quiescent plasma:

$$\mathbf{E} = \epsilon \mathbf{E}_1 + \mathcal{O}(\epsilon^2), \tag{10}$$

$$\mathbf{B} = \mathbf{B}_0 + \epsilon \mathbf{B}_1 + \mathcal{O}(\epsilon^2), \tag{11}$$

$$\mathbf{u} = \epsilon \mathbf{u}_1 + \mathcal{O}(\epsilon^2), \tag{12}$$

$$\rho_e = \mathcal{O}(\epsilon^2) \tag{13}$$

where $\mathbf{B}_0$ is constant and $\mathbf{E}_1$, $\mathbf{B}_1$, $\mathbf{u}_1$ are perturbations about the equilibrium configuration $(\mathbf{E} = 0, \mathbf{B} = \mathbf{B}_0, \mathbf{u} = 0)$ satisfying $\mathbf{E}_1 \cdot \mathbf{B}_0 = \mathbf{B}_1 \cdot \mathbf{B}_0 = \mathbf{u}_1 \cdot \mathbf{B}_0 = 0$. The parameter ϵ is merely a device to tag the relative magnitudes of each term and has no physical significance. It can be set to unity at the end of any calculation.

For a cold Maxwell plasma, the dispersion relation for a right-handed circularly polarized plane electromagnetic wave propagating along the background magnetic field is [23]

$$(\omega - \omega_c)(\omega - c^2 k^2/\omega) = \omega_p^2 \tag{14}$$

where ω_c is the electron's cyclotron frequency. For the case of a Born-Infeld plasma, equating the coefficients of ϵ in (1) and (2) yields the perturbations $(\mathbf{D}_1, \mathbf{H}_1)$ about $(\mathbf{D} = 0, \mathbf{H} = \mathbf{B}_0/\mu_0)$ corresponding to (10), (11):

$$\mathbf{D}_1 = \varepsilon_0 \frac{\mathbf{E}_1}{\sqrt{1 + \kappa^2 c^2 B_0^2}}, \tag{15}$$

$$\mathbf{H}_1 = \frac{1}{\mu_0} \frac{\mathbf{B}_1}{\sqrt{1 + \kappa^2 c^2 B_0^2}}. \tag{16}$$

One can show that right-handed circularly polarized plane electromagnetic waves propagating along the background magnetic field satisfy the following dispersion relation:

$$\begin{aligned}(\omega - \omega_c)(\omega - c^2 k^2/\omega) &= \omega_p^2 \sqrt{1 + \kappa^2 c^2 B_0^2} \\ &= \omega_p^{\rm BI\,2} (1 + \kappa^2 c^2 B_0^2)\end{aligned} \tag{17}$$

where (9) has been used.

1.2 Properties of non-linear waves

Particle acceleration in non-linear electrostatic waves close to breaking has recently been proposed as a possible mechanism for explaining how energetic electrons are ejected from within the interiors of pulsars [22].

If an atom is immersed in a uniform background magnetic field whose strength is much greater than $\sim 10^5$T then the corresponding magnetic force on the electrons is much greater than the atom's Coulombic forces [24]. The atom settles into the ground Landau level, limiting the electrons' spatial displacement transverse to the magnetic field lines. Thus, electrons are conducted preferentially along the direction of the magnetic field lines, and one may approximate the bulk electron motion as 1-dimensional [22]. Moreover, the magnetic field lines in the iron crust of a neutron star are expected to run parallel to its surface and to be strongly curved near the poles, where they emerge normal to the star's surface. The magnetic curvature near the poles is expected to lead to variations in electron number density and excite electrostatic waves in the electron 'gas' within the iron crust [22].

We now examine the behaviour of a Born-Infeld plasma in this context, by exploring properties of solutions to (1)-(6) that describe large-amplitude longitudinal plane waves. It is useful to envisage the electrons in the plasma as belonging to one or other of two families. The first family and the ion background constitute the bulk plasma; those electrons and the background ions form the wave. The members of the second family are the rest of the electron population, some of which are trapped in the wave's potential; we do not attempt to include the second family in the simple model explored here.

We seek properties of solutions to (1)-(6) that describe longitudinal plane waves. The fields have the form

$$\mathbf{u} = u(\zeta)\, \hat{\mathbf{z}}, \qquad \mathbf{E} = E(\zeta)\, \hat{\mathbf{z}}, \qquad \mathbf{B} = B_0\, \hat{\mathbf{z}} \tag{18}$$

where $\zeta = z - vt$ with the constant v being the phase speed of the wave and $0 < v < c$. It is useful to encode the 3-momentum $\mathbf{p}$ in terms of a dimensionless function $\xi = \xi(\zeta)$ as follows:

$$\mathbf{p} = m_e c\, \gamma \left(\frac{v}{c} \xi - \sqrt{\xi^2 - 1} \right) \hat{\mathbf{z}} \tag{19}$$

where $\xi > 1$ is assumed and the Lorentz factor $\gamma = 1/\sqrt{1 - v^2/c^2}$ corresponds to the phase speed v of the wave. The speed of the electrons described by (19) is less than v when the electrons are moving in the same direction as the wave, i.e. the electrons lag behind the wave.

Equations (1)-(6), (18), (19) lead to the following ordinary differential system:

$$\frac{d}{d\zeta}\left(\frac{E\sqrt{1+\kappa^2c^2B_0^2}}{\sqrt{1-\kappa^2E^2}}\right)=\frac{\rho_0\,\gamma^2}{\varepsilon_0}\left(1-\frac{v}{c}\frac{\xi}{\sqrt{\xi^2-1}}\right), \tag{20}$$

$$E=-\frac{1}{\gamma}\frac{m_e\,c^2}{e}\frac{d\xi}{d\zeta} \tag{21}$$

for ξ and E.

Inspection of (20), (21) reveals that, for oscillatory solutions, the electric field E has a turning point where $\xi=\gamma$. Further investigation reveals that this turning point is a minimum of E and an upper bound $E_{\max}$ ('wave-breaking limit') on E may be obtained by evaluating the first integral of (20) between the points ($\xi=1$, $E=0$) and ($\xi=\gamma$, $E=-E_{\max}^{\rm BI}$) where

$$E_{\max}^{\rm BI}=\frac{1}{\kappa}\sqrt{1-\left[\frac{\kappa^2\,E_{\max}^{\rm AP\;2}}{2\sqrt{1+\kappa^2\,c^2\,B_0^2}}+1\right]^{-2}}. \tag{22}$$

The maximum electric field $E_{\max}^{\rm AP}$ for a relativistic cold Maxwell plasma is

$$E_{\max}^{\rm AP}=\frac{m\omega_p c}{e}\sqrt{2(\gamma-1)} \tag{23}$$

and was first obtained by Akhiezer and Polovin [20]. The maximum electric field occurs during motion in which the plasma electrons approach the phase velocity of the wave (i.e. ξ approaches unity).

Further analysis of (20), (21) reveals the angular frequency $\omega_{\rm BI}$ of solutions to (20), (21) to be

$$\omega_{\rm BI}\approx\frac{\omega_{\rm AP}}{(1+\kappa^2c^2B_0^2)^{1/4}}\left[1-\left(\frac{\kappa m\omega_p c}{2e}\right)^2\frac{\gamma}{\sqrt{1+\kappa^2c^2B_0^2}}\right] \tag{24}$$

in the parameter regime $\gamma\gg1$ and $\kappa m\omega_p(1+\kappa^2c^2B_0^2)^{-1/4}/e\ll1/\sqrt{\gamma}$ with $\kappa cB_0\approx1$. Also, $\omega_{\rm AP}$ is the (angular) frequency of electrostatic waves of a cold Maxwell plasma for $\gamma\gg1$ [20],

$$\omega_{\rm AP}=\frac{\pi}{2\sqrt{2\gamma}}\omega_p. \tag{25}$$

If $\kappa=10^{-18}$m/V then $\kappa cB_0=1$ corresponds to $B_0=10^9$T, which is within the range of the surface magnetic fields of rotation-powered radio pulsars [24].

Acknowledgements

We thank the Cockcroft Institute and the ALPHA-X project for support.

References

[1] J. Schwinger, *Phys. Rev.* **82** (5) 664 (1951)

[2] M. Born, L. Infeld, *Proc. R. Soc. Lond. A* **144** 425 (1934)

[3] D. Hanneke, S. Fogwell, G. Gabrielse, *Phys. Rev. Lett.* **100** 120801 (2008)

[4] E.S. Fradkin, A.A. Tseytlin, *Phys. Lett. B* **163** 123 (1985)

[5] G.W. Gibbons, C.A.R. Herdeiro, *Phys. Rev. D* **63** 064006 (2001)

[6] R. Ferraro, *Phys. Rev. Lett.* **99** 230401 (2007)

[7] R. Ferraro, *J. Phys. A: Math. Theor.* **43** 195202 (2010)

[8] T. Dereli, R.W.Tucker, *EPL* **89** 20009 (2010)

[9] S.I. Kruglov *J. Phys. A: Math. Theor.* **43** 375402 (2010)

[10] D.A. Burton, R.M.G.M. Trines, T.J. Walton, H. Wen, *J. Phys. A: Math. Theor.* **44** 095501 (2011)

[11] G. Boillat, *J. Math. Phys.* **11** 941 (1970)

[12] J. Plebanski, *Lectures on Non-Linear Electrodynamics*, Nordita, Copenhagen (1970)

[13] P.A.M. Dirac, *Proc. R. Soc. Lond. A* **167** 148 (1938)

[14] D.A. Burton, J. Gratus, R.W. Tucker, *Ann. Phys.* **322** 599 (2007)

[15] D.J. Griffiths, T. C. Proctor, D.F. Schroeter, *Am. J. Phys.* **78** (4) 391 (2010)

[16] D. Chruściński, *Phys. Lett. A* **240** 8 (1998)

[17] M.K.H. Kiessling, *J. Stat. Phys.* **116** (1/4) 1057 (2004)

[18] H.P. Schlenvoigt, et al., *Nat. Phys.* **4** 133 (2008)

[19] M. Marklund, J. Lundin, *Eur. Phys. J. D* **55** 319 (2009)

[20] A.I. Akhiezer, R.V. Polovin, *Sov. Phys.–JETP* **3** 696 (1956)

[21] J.M. Dawson, *Phys. Rev.* **113** 383 (1959)

[22] D.A. Diver, et. al., *Mon. Not. R. Astron. Soc.* **401** 613 (2010)

[23] T.H. Stix, *Waves in Plasmas*, Springer-Verlag, New York (1992)

[24] A.K. Harding, D. Lai, *Rep. Prog. Phys.* **69** 2631 (2006)

2D Hydrodynamic Code Development and Simulations Relevant to Fast Ignition Fusion Targets

Contact iab500@york.ac.uk

I. A. Bush and J. Pasley
York Plasma Institute, University of York
Heslington, York, YO10 5DD

A. P. L. Robinson
Central Laser Facility, STFC Rutherford Appleton Laboratory
HSIC, Didcot, Oxon., OX11 0QX

Introduction

In fast-ignition inertial confinement fusion the heating of a compressed core of deuterium-tritium fuel is provided by a second, high-power, laser pulse [1,2]. This creates a beam of hot electrons which heat the central region in the compressed fuel up to ignition temperatures.

One challenge to overcome with this scheme is the problem of the large divergence angles of the electrons created by the laser pulse [3]. These will not efficiently heat the core of the fuel, as much of their energy will be wasted. One way to overcome this problem would be to use a structured collimator to control the spread of the electrons. This is achieved by through resistivity gradients, for example in a solid cone shaped target [4]. It as been shown that such a resistivity gradient can successfully restrict the spread of the electrons [5].

One potential problem is what could happen to the structured collimator itself, over the duration of the high-powered laser pulse. Over the 10 – 20 ps duration of the laser pulse the collimator will undergo extremely rapid Ohmic heating, due to the resistive return current induced by the forward going relativistic electrons. The relativistic electrons experience virtually no resistivity, and approximately balance the return current, such that $j_f \approx -j_r$. This leads to a heating term given by

$$\frac{\partial T}{\partial t} = \frac{\gamma - 1}{n_i k_B} \eta j_f^2 \quad (1)$$

where T is the temperature, γ the specific heat ratio, n_i the ion number density, k_B Boltzmann's constant, η the resistivity and j_f the fast electron current density.

Hydrodynamic simulations of such structured collimators are necessary to explore this effect. Thermal conduction and ion-electron equilibration can be of great importance in laser produced plasmas, and also need to be included.

Two-Fluid Hydrodynamics

Electrons and ions are initially taken to be separate species, with coupling between the two given arising through the electromagnetic field, the frictional collision force and the electron-ion collision term. The resulting set of equations are;

Conservation of mass

$$\frac{\partial n_i}{\partial t} + \nabla \cdot \left(n_i \boldsymbol{u_i} \right) = 0 \qquad \frac{\partial n_e}{\partial t} + \nabla \cdot \left(n_e \boldsymbol{u_e} \right) = 0 \quad (2,3)$$

Conservation of momentum

$$n_i m_i \left(\frac{\partial}{\partial t} + \boldsymbol{u_i} \cdot \nabla \right) = \quad (4)$$
$$e n_i \left(\boldsymbol{E} + \boldsymbol{u_i} \times \boldsymbol{B} \right) - \nabla p_i - n_i m_i \bar{\nu}_{ie} \left(\boldsymbol{u_e} - \boldsymbol{u_i} \right)$$

$$n_e m_e \left(\frac{\partial}{\partial t} + \boldsymbol{u_e} \cdot \nabla \right) = \quad (5)$$
$$-e n_e \left(\boldsymbol{E} + \boldsymbol{u_e} \times \boldsymbol{B} \right) - \nabla p_e - n_e m_e \bar{\nu}_{ei} \left(\boldsymbol{u_e} - \boldsymbol{u_i} \right)$$

Conservation of energy

$$\frac{n_i k_B}{\gamma - 1} \left(\frac{\partial}{\partial t} + \boldsymbol{u_i} \cdot \nabla \right) T_i + p_i \nabla \cdot \boldsymbol{u_i} + \nabla \cdot \boldsymbol{q_i} = S_i \quad (6)$$

$$\frac{n_e k_B}{\gamma - 1} \left(\frac{\partial}{\partial t} + \boldsymbol{u_e} \cdot \nabla \right) T_e + p_e \nabla \cdot \boldsymbol{u_e} + \nabla \cdot \boldsymbol{q_e} = S_e \quad (7)$$

With the energy source terms given by;

$$S_i = \frac{n_i k_B}{\gamma - 1} \bar{\nu}_{ie} \left(T_i - T_e \right) \quad (8)$$

$$S_e = \eta j_r^2 + \frac{n_e k_B}{\gamma - 1} \bar{\nu}_{ei} \left(T_e - T_i \right) \quad (9)$$

Here n is the number density, m the mass, $\boldsymbol{u}$ the velocity and p the pressure with the subscript denoting ions or electrons. e is the charge on an electron. $\bar{\nu}_{ie}$ represents the collision operator between ions and electrons. $\boldsymbol{E}$ and $\boldsymbol{B}$ are the electric and magnetic fields respectively. The terms involving $\boldsymbol{q}_i$ and $\boldsymbol{q}_e$ represent the thermal conduction, which is defined later.

Hydrocode Implementation

Some assumptions are made in the code, which means we can can track four fluid parameters, instead of the six given in the previous section. Quasi-neutrality is assumed to be maintained, such that $n_i = Z\, n_e$, with Z being the ionic charge. The electrons and ions are taken to move together with the same velocity, that is, $u_i = u_e$. The mass density of the ions is much greater than the mass density of the electrons, such that $\rho \approx \rho_i$.

The equations for the momentum of the ions and electrons are linked through the Lorentz force term. There are no external fields applied that will be considered.

Hence the only fluid parameter that need to be tracked for both the electrons and the ions is the temperature. The resulting equations that are used, when simplifying with these assumptions are given by;

$$\frac{\partial \rho}{\partial t}+\nabla\cdot(\rho \boldsymbol{u})=0 \tag{10}$$

$$\rho\left(\frac{\partial}{\partial t}+\boldsymbol{u}\cdot\nabla\right)=-\nabla\left(p_i+p_e\right) \tag{11}$$

$$\frac{\partial e_i}{\partial t}+\nabla\cdot\left(\left(e_i+p_i\right)\boldsymbol{u}\right)=-\boldsymbol{u}\,\nabla\cdot p_e \tag{12}$$

$$\frac{\partial e_e}{\partial t}+\nabla\cdot\left(e_e\boldsymbol{u}\right)=\boldsymbol{u}\nabla\cdot p_e \tag{13}$$

where e is the total energy density, which is given by;

$$e_i=\frac{p_i}{\gamma-1}+\frac{1}{2}\rho_i\left|\boldsymbol{u}^2\right| \tag{14}$$

for the ions, and similarly for the electrons. The thermal conduction and equilibration implementation are not included here, but will be added in the next section.

This equation set is solved using a similar method to that discussed in Ziegler [6]. This is a Godunov-type scheme which is effective at naturally treating shocks without requiring artificial viscosity.

Equilibration

The equilibration between ions and electrons is given by;

$$\frac{\partial T_i}{\partial t}=\bar{\nu}_{ie}\left(T_e-T_i\right) \tag{15}$$

with the collision frequency is given by;

$$\bar{\nu}_{ie}=\frac{8\sqrt{2\pi}\,n_e Z^2 e^4 \ln\Lambda}{3\,m_i m_e k_B^{3/2}\left(\frac{T_i}{m_i}+\frac{T_e}{m_e}\right)^{3/2}\epsilon_0^2} \tag{16}$$

where the symbols have their previously defined meanings, and ln Λ is the Coulomb logarithm. Note also that;

$$\bar{\nu}_{ie}=\frac{n_e}{n_i}\bar{\nu}_{ei}=Z\,\bar{\nu}_{ei} \tag{17}$$

This is implemented in the code using an implicit scheme, which ensures numerical stability. The resulting equations for the equilibration are given by;

$$T_i^{n+1}=\frac{\left(1+n_i\beta\Delta T_i^n\right)+n_e\beta\Delta t\,T_e^n}{1+\left(n_e+n_i\right)\beta\Delta t} \tag{18}$$

$$T_e^{n+1}=\frac{\left(1+n_e\beta\Delta T_e^n\right)+n_i\beta\Delta t\,T_i^n}{1+\left(n_i+n_e\right)\beta\Delta t} \tag{19}$$

where the value β is given by;

$$\beta=\frac{\bar{\nu}_{ie}}{n_e}=\frac{\bar{\nu}_{ei}}{n_i} \tag{20}$$

and Δt is the time-step in the code. The superscript n refers to the current time-step in the code, and $n+1$ the next time-step.

As an implicit method is being used no special time-step restriction is imposed for the equilibration. This means that, depending on the problem, equilibration could occur quickly over a few time steps, although in many of the simulations of interest the equilibration will only occur over the length of the simulation.

Thermal Conduction

The thermal conduction in a plasma is given by the Spitzer-Härm formula [7];

$$\frac{\partial u}{\partial t}=\nabla\cdot\left(\kappa_{SH}\nabla T\right) \tag{21}$$

where u is the internal energy, that is $u = p / (\gamma - 1)$.

Here κ_{sh} is given by;

$$\kappa_{SH}=20\left(\frac{2}{\pi}\right)^{3/2}\frac{\epsilon_0\left(k_B T\right)^{5/2}k_B}{\sqrt{m_e}e^4 Z\ln\Lambda} \tag{22}$$

The effective thermal conductivity is actually less than this. An electric field is produced such that current created by the temperature gradient is canceled, which reduces in turn the heat flow. The reduction factor is given by [7,8];

$$\epsilon=0.4\frac{Z}{Z+0.2\log_{10}\left(Z+3.44\right)} \tag{23}$$

and the effective thermal conductivity given by;

$$\kappa=\epsilon\,\kappa_{SH} \tag{24}$$

This is similarly solved implicitly, to ensure stability in the code. The initial equations are given by;

$$\frac{T_j^{n+1}-T_j^n}{\Delta t}=\frac{\gamma-1}{n k_B}\frac{F_{j+1/2}^{n+1}-F_{j-1/2}^{n+1}}{\Delta x} \tag{24}$$

where the flux, F, is given by

$$F_{j+1/2}=\frac{\kappa_{j+1}+\kappa_j}{2}\frac{T_{j+1}-T_j}{\Delta x} \tag{25}$$

and similarly for $F_{j-1/2}$. Here Δx is the cell width and j refers to the cell number.

Overall this gives the relation;

$$T_j^n=T_j^{n+1}-\frac{\Delta t}{2\Delta x^2}\frac{\gamma-1}{n k_B}\left[\left(\kappa_{j+1}+\kappa_j\right)T_{j+1}-\left(\kappa_{j+1}+2\kappa_j+\kappa_{j-1}\right)T_j+\left(\kappa_j+\kappa_{j-1}\right)T_{j-1}\right] \tag{26}$$

This can be rewritten as a tridiagonal matrix equation. To solve for the new temperature this matrix needs to be inverted, which is done using an implementation of the Thomas algorithm [9]. In the code the thermal conduction for the x-direction and y-direction are done separately in consecutive steps.

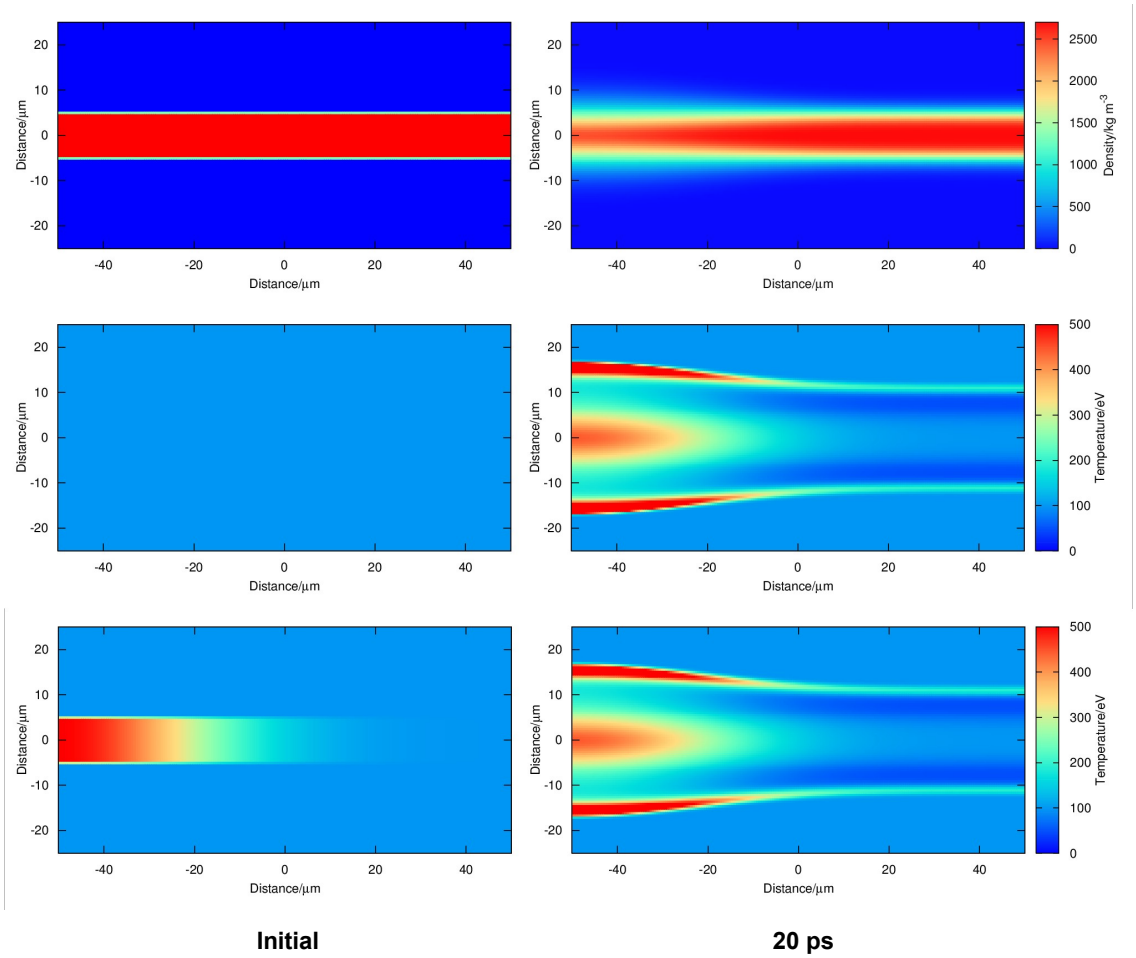

Figure 1: *Spatial profiles for density (top), ion temperature (middle) and electron temperature (bottom) at 0 ps and 20 ps. It can be seen the electrons and ions have reached equilibrium after 20 ps. This is for an aluminium plasma initially at rest.*

Results

Extensive tests of problems relevant to fast-ignition have not yet been performed, however some tests of the code have been done. In figure 1 the initial density, ion temperature and electron temperature are shown respectively, alongside the values at 20 ps. In this problem a 10 μm region of an aluminium plasma has an electron temperature profile given by;

$$T_{eV} = 400\, e^{-\frac{x^2}{2\sigma^2}} + 100$$

where σ = 25 μm. The rest of the plasma has an initial temperature of 100 eV. In the central 10 μm region the density is 2700 kg m^{-3}, solid density for aluminium. The remainder is at one thousandth of aluminium solid density.

It can be seen that after 20 ps the temperature of the ions and electrons are identical. The initial higher density plasma has remained largely intact.

Conclusions

A discussion has been given of the creation of a 2D hydrodynamics code, which includes treatment of an ion and electron species with different temperatures. Ion-electron equilibration has been implemented along with thermal conductivity and the results of a simulation has been shown.

Future work needs to be done in using this code to look at problems relevant to fast-ignition. This will be done by taking temperature profiles from other simulations and looking at the hydrodynamic response of the plasma to the return current heating the target is subjected to.

References

1. Nuckolls J *et al*. 1972 Nature **239** 139
2. Lindl J 1995 Phys. Plasmas **2** 3933
3. Stephnes R *et al.* 2004 Phys. Rev E. **69** 066414
4. Robinson A P L *et al.* 2007 Phys. Plasmas **14** 083105
5. Kar S et al. 2009 Phys. Rev. Lett. **102** 055001
6. Ziegler U 2004 J. Comp. Phys. **196** 393
7. Spitzer L 1962 *Physics of Fully Ionized Gases*
8. Schurtz G *et al.* 2000 Phys. Plasmas **7** 10
9. Press W H *et al.* 1986 *Numerical Recipes in Fortran 90, Second Edition*

Evolution of a short pulse via ray tracing

Contact: rac@st-andrews.ac.uk

R.A. Cairns
University of St Andrews
School of Mathematics and Statistics
St Andrews, Fife, KY16 9SS

1 Introduction

In a recent paper [1] we have suggested a way in which the radiation pattern produced by an antenna can be reproduced in detail by following rays. The method relies on the use of the asymptotic method of stationary phase to find the wave amplitude and phase in the far field region away from the antenna, the innovative feature being the development of a method that does not depend on having explicit knowledge of the phase or a solution in terms of a phase integral. The required information is obtainable by looking at differences between adjacent rays. Examples for which an explicit solution can be found and compared with the approximation show that it works well except in the vicinity of a region where rays are reflected. Our object here is to adapt this method to study the evolution of short pulses launched into a time and space dependent medium, a problem with possible relevance to some laser plasma systems.

2 Theory

We consider a one-dimensional problem with a short pulse launched from $x = 0$ into the region $x > 0$. The time dependence of the pulse will be assumed centered around $t = 0$ and we shall assume that the pulse is propagating into a cold plasma so that the local dispersion relation is

$$D = \omega^2 - \omega_p^2 - k^2c^2 = 0 \tag{1}$$

with ω_p, the plasma frequency, a function of x and t. With a time-dependent plasma frequency the wave frequency changes as it propagates, as can be seen from the standard ray-tracing equations [2] and applications of this photon acceleration to laser plasma have been explored by Mendonça [3]. The initial pulse launched from $x = 0$ can still be Fourier transformed in time, even though the frequencies change as the wave propagates and, since we are dealing with a linear problem, the wave field is a superposition of these initial Fourier components. The rate of change of the background plasma is assumed such that there is no appreciable change during the time taken to launch the pulse. We shall use Ω as the Fourier transform variable of the initial pulse and ω for the frequency following a ray.

In principle the wave amplitude at any point will be a summation over the different Fourier components. We shall assume that the solution at any point for a given Fourier component can be expressed as a slowly varying amplitude and a phase, taking the form $A(\Omega, x, t) \exp\left[i\Phi\left(\Omega, x, t\right)\right]$. The full solution will then take the form

$$a(x,t) = \int_{-\infty}^{\infty} A(\Omega, x, t) \exp\left[i\Phi\left(\Omega, x, t\right)\right] d\Omega. \tag{2}$$

The essence of the method of stationary phase [4] is to assume that rapid variations in the phase factor cancel out over most of the range of integration and that the dominant contribution comes from the neighbourhood of points where

$$\frac{\partial}{\partial\Omega}\left[\Phi\left(\Omega, x, t\right)\right] = 0. \tag{3}$$

Taking this to be the case and letting Ω_0 be the frequency at which (3) is satisfied, we then approximate the integral by

$$\int_{-\infty}^{\infty} A(\Omega_0, x, t) \exp\left[i\Phi\left(\Omega_0, x, t\right) + i\frac{1}{2}\left(\Omega - \Omega_0\right)^2 \Phi''(\Omega_0, x, t)\right] d\Omega$$
$$= A(\Omega_0, x, t)\sqrt{\frac{2\pi}{|\Phi''|}} e^{i\Phi \pm i\frac{\pi}{4}} \tag{4}$$

where the sign in the exponential correponds to that of Φ'' and the primes denote derivatives with repect to Ω. The problem we now address is how to obtain the second derivative of the phase in the absence of any explicit expression for Φ.

We begin by relating the problem to ray tracing. The standard ray racing equations [2] are

$$\begin{aligned} \dot{x} &= -\frac{\frac{\partial D}{\partial k}}{\frac{\partial D}{\partial \omega}} \\ \dot{k} &= \frac{\frac{\partial D}{\partial x}}{\frac{\partial D}{\partial \omega}} \\ \dot{\omega} &= -\frac{\frac{\partial D}{\partial t}}{\frac{\partial D}{\partial \omega}} \end{aligned} \tag{5}$$

where D is defined by (1) and its dependence on x and t is through that of the plasma frequency. Since the wavenumber and frequency are related to the phase by

$$\begin{aligned} k &= \frac{\partial \Phi}{\partial x} \\ \omega &= -\frac{\partial \Phi}{\partial t} \end{aligned} \tag{6}$$

the phase along a ray path is

$$\Phi = \int (k dx - \omega dt),$$

with the integral starting at the origin, and

$$\frac{\partial \Phi}{\partial \Omega} = \int \left(\frac{\partial k}{\partial \Omega} dx - \frac{\partial \omega}{\partial \Omega} dt \right) = - \int \frac{\left(\frac{\partial k}{\partial \Omega} \frac{\partial D}{\partial k} + \frac{\partial \omega}{\partial \Omega} \frac{\partial D}{\partial \omega} \right)}{\frac{\partial D}{\partial \omega}} dt$$

using (5). The numerator in this integral is the total derivative of D with respect to Ω and is zero since D is identically zero. We conclude then that $\frac{d\Phi}{d\Omega}$ is zero along a ray path and so the point of stationary phase at any value of x and t is determined by the initial frequency such that a ray launched from the origin at $t = 0$ arrives at that point. That being so we now need to calculate the second derivative of the phase in order to find the wave amplitude from (4).

Following the method of [1] we note that following the ray path

$$\frac{\partial^2 \Phi}{\partial \Omega^2} = \int \left(\frac{\partial^2 k}{\partial \Omega^2} dx - \frac{\partial^2 \omega}{\partial \Omega^2} dt \right) = - \int \frac{\left(\frac{\partial^2 k}{\partial \Omega^2} \frac{\partial D}{\partial k} + \frac{\partial^2 \omega}{\partial \Omega^2} \frac{\partial D}{\partial \omega} \right)}{\frac{\partial D}{\partial \omega}} dt$$

and that by using the fact that the total derivative of D is zero we can obtain an expression involving first derivatives of the wavenumber and frequency with respect to the launch frequency. Since these derivatives need to be evaluated numerically, this should allow better accuracy than using the original expression with second derivatves. The integral is taken from $t = 0$, $x = 0$ along the ray trajectory. Note that all rays are launched at the same time, the time dependence of the pulse being implicit in its Fourier spectrum rather than in the launch conditions. This is analogous to the spatial problem where the rays are all launched from the centre of the antenna. In the latter case the solution is only valid sufficiently far from the antenna (a few antenna widths in practice) and in the present case the solution is only valid sufficiently far from the origin that the solution is dominated by the dispersion of the different frequency components.

At this point it will be useful to illustrate the method with a simple example, namely a short pulse launched into a homogeneous plasma. The solution of this problem can be found exactly and is

$$a(x,t) = \int_{-\infty}^{\infty} \tilde{a}(\Omega) \exp\left[i \left(\Omega^2 - \omega_p^2 \right) x - i \Omega t \right] d\Omega \qquad (7)$$

with $\tilde{a}$ the Fourier transform of the time-dependence of the pulse launched from $x = 0$. This illustrates the way in which the solution is a superposition of the different frequency components. Of course, the standard method of stationary phase could readily be applied to this integral to yield the asymptotic behaviour and it is readily verified that the condition for stationary phase is equivalent to $x = v_g t$. However, we test the numerical method by using our method with the derivatives of wavenumber and frequency obtained by finite differencing on adjacent rays. Figure 1 illustrates how the approximation so obtained compares with the exact solution with an initial Gaussian pulse $a(x,0) = e^{i\omega_0 t} \exp\left[-\frac{t^2}{2T^2} \right]$. Time and distance are measured in units of $\frac{1}{\omega_0}$ and $\frac{c}{\omega_0}$ respectively and in these units $\omega_p = 0.2$, $T = 10$. The number of rays used is 40.

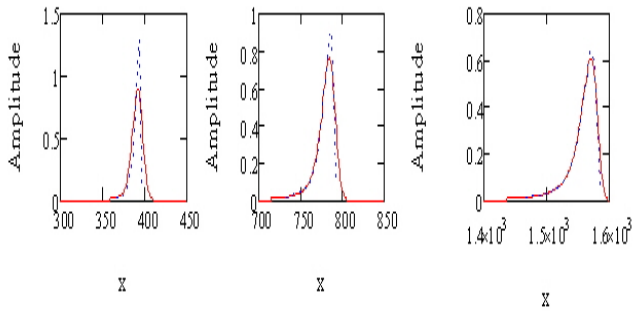

Figure 1. Exact (full red) and approximate (dotted blue) amplitudes for $t = 400, 800, 1600$. Beyond 1600 the graphs are essentially indistinguishable. Note changing scale on x-axis - pulse becomes broader with time.

Near the source the approximation is too peaked, a consequence of the fact that all rays are launched at the same time. However, once the spreading of the rays becomes the dominant factor in determining the width the agreement is excellent. The ray tracing here is obviously trivial, the main point being to see how well our method works. We now go on to look at a more general problem where the plasma frequency varies in time and space and an explicit solution is not readily obtainable.

3 Further discussion of the theory and an example.

The calculation of the derivatives needed to obtain the wave amplitude needs some care. In the phase integral, as can be seen from the example above, the derivative with respect to frequency needs to be carried out at constant x and t. However, the rays are followed as a function of t and at any fixed t adjacent rays are at different values of x. This needs to be allowed for in the calculation of the derivatives from differencing on adjacent rays, but we do not have space here to discuss the details of the mathematics. One further factor which needs taken into account is the change in amplitude due to the change in the energy density of the wave as it propagates in a

changing medium. This is separate from the effect of dispersion of the waves which we have considered so far. If we express the amplitude in terms of the vector potential a of the wave, then as shown by [5] the quantity ωa^2 is conserved for each frequency component, assuming the gradients in space or time to be small. This means that, in our one-dimensional problem,

$$\frac{\partial}{\partial t}\left(\omega a^2\right) + \frac{\partial}{\partial x}\left(v_g \omega a^2\right) = 0. \tag{8}$$

Following a ray path this implies that

$$\frac{d}{dt}\left(\omega a^2\right) = \frac{\partial}{\partial t}\left(\omega a^2\right) + v_g \frac{\partial}{\partial x}\left(\omega a^2\right) = -\left(\omega a^2\right)\frac{\partial v_g}{\partial x}. \tag{9}$$

Now

$$\frac{\partial v_g}{\partial x} = -\frac{1}{\sqrt{\omega^2 - \omega_p^2}}\frac{\omega_p}{\omega}\frac{\partial \omega_p}{\partial x}$$

while from the ray tracing equations

$$\dot{k} = -\frac{\omega_p}{\omega}\frac{\partial \omega_p}{\partial x}$$

so that (9) becomes

$$\left(\omega a^2\right)^{-1}\frac{d}{dt}\left(\omega a^2\right) + k^{-1}\frac{dk}{dt} = 0 \tag{10}$$

implying that $k\omega a^2$ is constant along the ray. The amplitude variation implied by this is included as an effect additional to that due to the spreading of the rays.

To illustrate the method we look at a pulse (as before) being overtaken by a moving density ramp as illustrated in Figure 2. The peak of the pulse has been reduced to 0.25 in the figure for convenience. We use 100 rays, initially spread across the spectrum of the pulse. Since its time profile is Gaussian, so too is the spectrum, and the rays initially are spaced evenly over ± 2.5 standard deviations from the centre, at 1 in our normalised units.

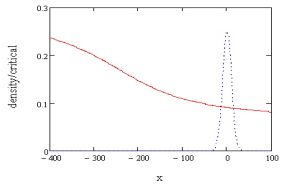

Figure 2. Initial pulse shape (blue) and density profile (red) in terms of critical density for frequency ω_0.The profile moves to the right with velocity $0.98c$.

Figure 3 shows the amplitudes and frequencies of the rays as a function of position, in the frame moving with the density ramp, at $t = 5 \times 10^3$. The ramp has overtaken the pulse which has been blue shifted by photon acceleration in the increasing density.

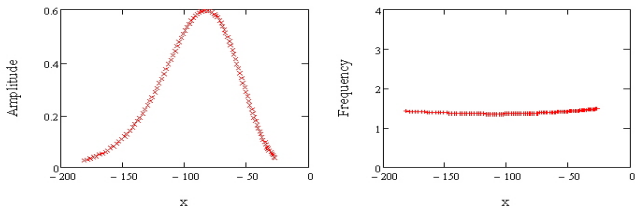

Figure 3. The amplitudes (electric field as a ratio to the peak electric field of the initial pulse) and frequencies of the rays at $t = 5 \times 10^3$.

At a later time Figure 4 shows the pulse very substantially blue shifted and now moving forward with respect to the density ramp with highest frequencies at the back of the pulse.

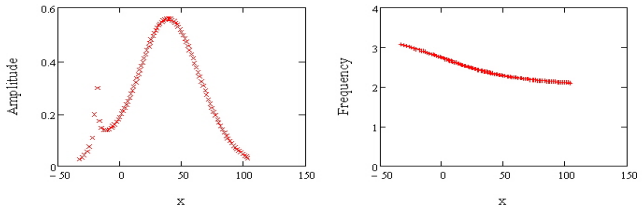

Figure 4. As for Figure 3 with $t = 2.5 \times 10^4$.

The peak on the trailing edge occurs in the neighbourhood of a point where the second derivative passes through zero. The method obviously breaks down there and the exact behaviour needs further investigation.

At $t = 5 \times 10^4$ the pulse is as shown in Figure 5.

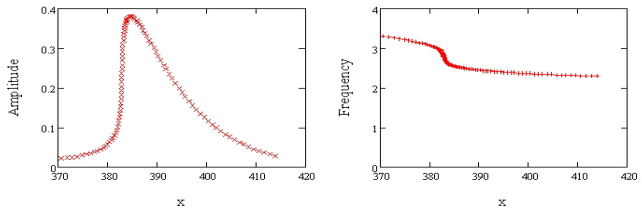

Figure 5. As before with $t = 5 \times 10^4$.

The higher frequency components at the back of the pulse have caught up with the lower frequencies, leading to a steepening and shortening of the pulse. Finally we show the pulse at $t = 10^5$.Now all the higher frequency rays have overtaken the lower frequencies and the sign of the chirp is reversed.

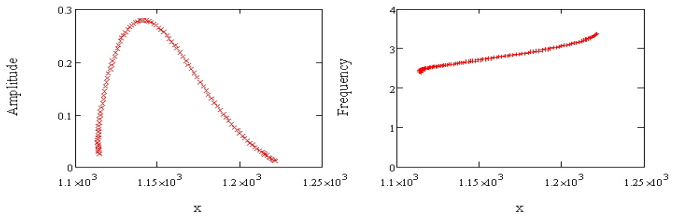

Figure 6. As before at $t = 10^5$.

4 Conclusions

We have outlined a method for obtaining the exact evolution of a short pulse launched into a space and time dependent system based on tracing of rays. In the far field region the method of stationary phase is used to give an exact description of the evolution of the amplitude of each ray, building on a theory already developed for a time-independent problem. The most closely related method which has been used in the past is probably that of photon kinetics [6], [7] which also follows an ensemble of ray paths. There, however, the wave intensity is taken to be given by the density of photons. In our theory the importance of the classical ray path depends on the fact that along it neighbouring Fourier components of the pulse have almost the same phase and so reinforce each other to give the dominant wave contribution. The amplitude depends on the rate of variation of the phase around this stationary value. The essential way in which this goes beyond the standard method of stationary phase is, of course, the way in which the idea of this method is employed in a situation where the complexity of the problem does not allow us to obtain a solution in the form of a phase integral. Instead, the required rate of variation of phase about the stationary point is obtained from numerical derivatives obtained by finite differencing on rays with adjacent initial frequencies.

A major limitation of the discussion here is its restriction to one spatial dimension. However, the inclusion of transverse spatial dimensions should be possible in the same way as an extra dimension in the launching antenna can be included in the spatial problem [1]. This would involve Fourier transforming the initial transverse profile of the pulse as well as its time dependence, so more rays would be needed to give good resolution. However, the advantage of this method is its computational simplicity. Following the hundred rays used in the calculations of the previous section out to a time of 10^5 dimensionless units then doing the differencing necessary to obtain the amplitudes took less than a minute on a laptop computer. Using a larger machine it should be possible to follow many rays quite easily and, since the ray paths are all independent, the method should be ideally suited to parallel machines. We have not considered here the details of the interference between different rays arriving at the same point, something which occurs as high frequency rays overtake lower frequency rays as we go from Figure 5 to figure 6. However, our earlier work on the time independent problem shows that it is, in principle, possible to obtain fine details of this by following the wave phase. This would need to be done numerically, but since the phase is slowly varying for the type of problem for which this method is appropriate, these details should be accessible without the need to follow the time variation with the resolution which would be required in a direct solution of the wave equation.

Another limitation of the discussion here is that it does not take account of the self-consistent evolution of the plasma. So long as the interaction of the wave with the plasma is via the ponderomotive force so that the discussion of energy conservation of equations (8) to (10) is valid then it should be possible to couple the plasma evolution to evolution of the wave field using this method. Problems involving photon acceleration in any kind of time dependent plasma should be readily treated by this method, more accurately than by just looking at ray paths and much more easily than by doing full wave calculations.

5 Acknowledgement

This work was carried out as part of the Alpha-X project supported by the UK Engineering and Physical Sciences Research Council.

References

[1] R.A. Cairns and V.Fuchs, Nucl. Fusion **50**, 095001 (2010).

[2] S. Weinberg, Phys. Rev. **126**, 1899 (1962).

[3] J.T. Mendonça, *Theory of Photon Acceleration*, Institute of Physics Publishing, Bristol and Philadelphia (2000).

[4] J.D. Murray, *Asymptotic Analysis,* Springer, New York, 1984.

[5] R.A. Cairns, A. Reitsma and R. Bingham, Phys. Plasmas **11**, 766 (2004).

[6] I.M. Besieris and F.D. Tappert, J. Math. Phys. **14**, 704 (1973)

[7] R.M.G.M. Trines, R. Bingham, L.O. Silva, J.T. Mendonça, P.K Shukla., C.D. Murphy, M.W. Dunlop, J.A. Davies, R. Bamford, A. Vaivads, P.A. Norreys, Phys. Plasmas **16**, 055904 (2009).

Calculation of Siegert states of molecules in electric field : an H_2^+ study

contact : linda@power1.pc.uec.ac.jp, lhamonou01@qub.ac.uk

Linda Hamonou
University of Electro-communications,
1-5-1, Chofu-ga-oka, Chofu-shi, Tokyo, Japan

Oleg I. Tolstikhin
Russian Research Center "Kurchatov Institute"
Kurchatov Square 1, Moscow 123182, Russia

Toru Morishita
University of Electro-communications,
1-5-1, Chofu-ga-oka, Chofu-shi, Tokyo, Japan

Shinichi Watanabe
University of Electro-communications,
1-5-1, Chofu-ga-oka, Chofu-shi, Tokyo, Japan

1. Introduction

Siegert states of atoms and molecules placed in an electric field, defined as the solutions to the stationary Schrödinger equation satisfying the regularity and outgoing-wave boundary conditions [2], have been obtained by Batishchev *et al* [1] within th restriction of the single active electron (SAE) approximation. In [1] was presented an efficient method to calculate not only the complex energy eigenvalues, but also the eigenfunctions for a general class of one-electron atomic potentials. They also derived an exact expression for the transverse momentum distribution of the ionized electrons in terms of Siegert eigenfunction in the asymptotic region.

In the previous CLF report we presented an extension of the Siegert states to molecules. The formulation of computational method requires some modifications from the atomic procedure.

In this report we present the preliminary results obtained using the molecular formulation to study the simplest molecular ion, H_2^+. We first give the basic equation required for understanding the Siegert states of molecules. Then we explain the numerical procedure including a DRV basis set and R-matrix propagation. Results have been obtained for different potential models of H_2^+ for an internuclear distance of R=2 and an angle between the electric field direction and the molecular axis $\theta = 0$. We use atomic units through the report in not specified otherwise.

2. Basic equations

The Siegert states of molecules are obtained within the SAE approximation by solving the following Schrödinger equation

$$H\varphi = E\varphi \tag{1}$$

The Hamiltonian for an electron interacting with a molecular potential $V(\mathbf{r})$ in presence of a static uniform electric field $\mathbf{F}$ directed along the z axis is given by :

$$H = -\frac{1}{2}\Delta + V(\mathbf{r}) + Fz. \tag{2}$$

We use the parabolic coordinates η, φ

and ξ defined as follow.

$$\xi = r + z, 0 \leq \xi \leq \infty \quad (3)$$

$$\eta = r - z, 0 \leq \eta \leq \infty \quad (4)$$

$$\varphi = arctan\frac{y}{x}, 0 \leq \varphi \leq 2\pi \quad (5)$$

In the general cases, for an arbitrary molecular potential $V(\mathbf{r})$, the variables (ξ, η) and ϕ cannot be separated as they are for the atomic case. In order to solve the molecular problem we have to take into account a coupling in φ. The Schrödinger equation (1) in paraboliccoordinates is rewritten in the form

$$\left[\frac{\partial}{\partial\eta}\eta\frac{\partial}{\partial\eta} - \frac{1}{4\eta}\frac{\partial^2}{\partial\varphi^2} + \mathbf{B}(\eta) + \frac{E\eta}{2} + \frac{F\eta^2}{4}\right]\psi(\xi,\eta,\varphi) = 0, \quad (6)$$

where

$$\mathbf{B}(\eta) = \frac{\partial}{\partial\xi}\xi\frac{\partial}{\partial\xi} - \frac{1}{4\xi}\frac{\partial^2}{\partial\varphi^2} - \frac{\xi+\eta}{2}V(\xi,\eta) + \frac{E\xi}{2} - \frac{F\xi^2}{4}. \quad (7)$$

These equations must be supplemented by the regularity and out-going-wave boundary conditions [2]. For non-zero electric fields, all the eigenstates are unbound, so the eigenvalue E is a complex number

$$E = \mathcal{E} - \frac{i}{2}\Gamma \quad (8)$$

with the real part $\mathcal{E}$ giving the energy of the state, and the imaginary part Γ defining the ionisation rates. Equation () and (7) are solved using the slow-variable discretization (SVD) method [3] in combination with the R-matrix propagation technique [4].

3. Numerical procedure

The numerical procedure is based on the discrete variable representation (DVR) basis sets [5] constructed from Laguerre, Jacobi and Legender polynomials compatible with the boundary conditions [6]. We refer the reader to [1] for more mathematical and numerical details.

In the atomic case [1], the eigenfunctions of the adiabatic Hamiltonian were obtained using the DVR constructed using the generalized Laguerre polynomials $L_n^{|m|}(s\xi)$ [6], where the scaling s defines the extent of the DVR basis in ξ.

This representation enables the exact incorporation of the regularity boundary condition $\psi(\xi,\eta)|_{\xi\to 0} \propto \xi^{|m|/2}$ into the formulation. In the molecular case, the solution $\psi(\xi,\eta,\varphi)$ contains integer and half-integer powers of ξ for $\xi \to 0$ which cannot be represented by a single Laguerre-DVR basis with a fixed magnetic quantum number m. We thus introduce a new variable.

$$\xi = \zeta^2 \quad (9)$$

So we have

$$B(\eta) = \frac{\tilde{B}(\eta)}{4\zeta} \quad (10)$$

with

$$\tilde{B}(\eta) = \frac{\partial}{\partial\zeta}\zeta\frac{\partial}{\partial\zeta} + \left(\frac{1}{\zeta} + \frac{\zeta}{\eta}\right)\frac{\partial^2}{\partial\varphi^2} - 2\zeta(\zeta^2+\eta)V(\xi,\eta,\varphi) + 2E\zeta^3 - F\zeta^5. \quad (11)$$

This transformation allows us to use a single-Laguerre-DVR basis with $m = 0$ for the expansion in ζ. The eigenfunctions of $\tilde{B}(\eta)$ are constructed using the direct product of the Laguerre-DVR basis with periodic boundary conditions in φ.

In the R-matrix theory [7], the space is divided into two regions, an inner region which is here divided into N_{sec} sectors so that $0 \leq \eta \leq \eta_c$ can be define by

$$0 = \eta_0 < \eta_1 < \cdots < \eta_{N_{sec}} = \eta_c. \quad (12)$$

In each sector, we construct the R-matrix basis $\bar{\psi}_n(\xi, \eta, \varphi)$ defined by

$$\left[\frac{\partial}{\partial\eta}\eta\frac{\partial}{\partial\eta} - \mathcal{L} - \frac{1}{4\eta}\frac{\partial^2}{\partial\varphi^2} + \mathbf{B}(\eta) + \frac{\bar{E}\eta}{2} + \frac{F\eta^2}{4}\right]\bar{\psi}(\xi, \eta, \varphi) = 0, \quad (13)$$

with $\mathcal{L}$ is the Bloch operator given by:

$$\mathcal{L} = \eta[\delta(\eta - \eta_+) - \delta(\eta - \eta_-)]\frac{\partial}{\partial\eta}. \quad (14)$$

Similarly to the η variable, in the molecular problem in order to incorporate the regularity boundary condition $\psi(\xi, \eta)|_{\eta\to 0} \propto \eta^{|m|/2}$, the solution contains integer and half-integer powers of η. We thus introduce another change of variables in the first sector,

$$\eta = \chi^2 \quad (15)$$

to allow the representation of the solution by a single Legendre-DVR basis. In the outer region, $\eta > \eta_c$, the molecular potential is substituted by a purely Coulomb potential $-Z_{as}/r$ so that the problem becomes exactly separable in parabolic coordinates and reduced to solving uncoupled equations in η [1]. We apply out-going wave boundary condition. The R-matrix is propagated from $\eta = 0$ outward and from $\eta = \eta_c$ inward. Matching the solutions at the right boundary in the first sector gives the Siegert eigenvalue E and eigenfunctions.

4. Results

The calculation are performed for H_2^+ molecular ion. The internuclear distance is fixed to R=2, and the angle between the electric field direction and the molecular axis is set to $\theta = 0$. The molecular ion is modeled by a soft Coulomb potential.

$$V = \frac{1}{2}(\xi + \eta)\left(-\frac{1}{\sqrt{\xi\eta + (\frac{(\xi-\eta)}{2} - \frac{R}{2})^2 + b^2}} - \frac{1}{\sqrt{\xi\eta + (\frac{(\xi-\eta)}{2} + \frac{R}{2})^2 + b^2}}\right) \quad (16)$$

The softening parameters is initially set to $b = 0.09$ which gives a very rounded potential, the energies obtained are represented by the black curved and compared with energies obtained by perturbation theory in blue on the left hand side whereas the right hand side presents the corresponding ionisation rates in black and the comparison with MOADK in blue. We also performed calculation with a sharper potential $b = 0.0009$ allowing a better representation of real H_2^+ molecular ion, the energies and ionisation rates are presented by the red curves and compared

as well with perturbation theory's energies and MOADK [10] ionisation rates in green. We obtain a good agreement with perturbation theory for electric field $F < 0.25$ which is to be expected as perturbation theory is limited to low electric field. We can also notice that for the rounded potential with $b = 0.09$ our ionisation rates are lower than the one given by MOADK which is also to be expected as MOADK tend to overestimate the ionisation rates. However the ionisation rate obtained for the sharper potential with $b = 0.0009$ is much higher than the value obtained with MOADK. For sharper potential, as bounding energy increases, the ioinsation rates decreases leading to an underestimation of the ionisation rates by MOADK.

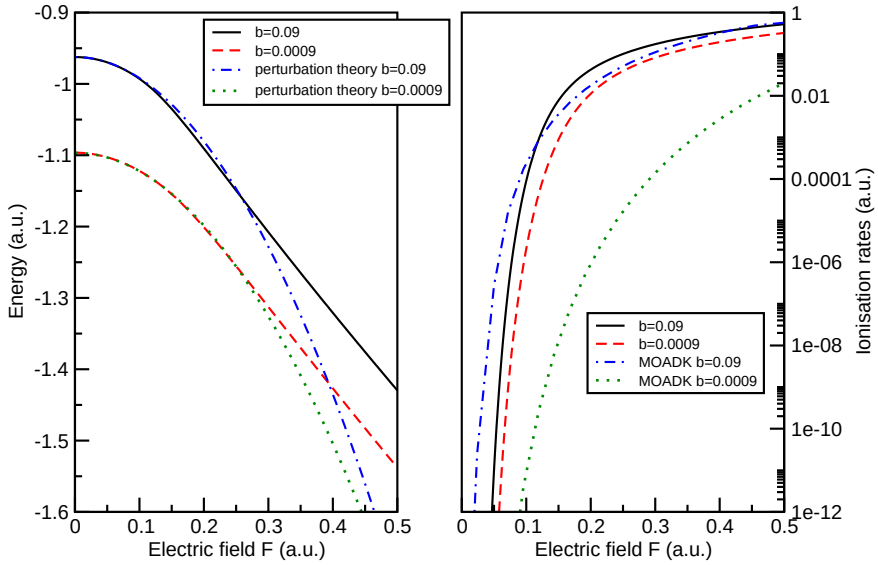

Figure 1. Electric field dependent energies and ionisation rates obtained with two different potential and compared with other theory.

5. Conclusion

In this report, we have presented the development necessary to calculate the molecular Siegert states in a static electric field. Starting from an atomic problem enabling the calculation of Siegert states in the single active electron approximation, we extended the problem reducing the use of the symmetries and including the coupling in φ coordinate to solve molecular problems. This new method enable us to obtain eigenvalues and eigenfunctions for a particular Siegert state as a function of a variating electric field for molecules modeled by one-electron potential. The complex eigenvalue obtained from the match of the R-matrix with the out-going wave Siegert boundary condition gives the energy and the ionization rate of a particular state.

6. Reference

1. P. A. Batishchev, O. I. Tolstikhin and T. Morishita, Phys. Rev. A **82**, 023416 (2010)
2. A. J. F. Siegert, Phys. Rev. **56**, 750 (1939)
3. O. I. Tolstikhin, S. Watanabe and M. Matsuzawa, J. Phys. B **29**, L389 (1996)
4. K. L. Baluja, P. G. Burke and L. A. Morgan, Comput. Phys. Commun. **27**, 299 (1982)
5. D. O. Harris, G. G. Engerholm and W. D. Gwinn, J. Chem. Phys. **43**, 1515 (1965)
6. A. S. Dickinson and P. R. Certain, J. Chem. Phys. **49**, 4209 (1968)
7. J. C. Light, I. P. Hamilton and J. V. Lill, J. Chem. Phys. **82**, 1400 (1985)
8. O. I. Tolstikhin and C. Namba, *CTBC - A Program to Solve the Collinear three-Body Problem: Bound States and Scattering Below the Three-body Disintegration Threshold*, Research Report NIFS-779 (National Institute for Fusion Science, Toki, Japan, 2003). Available at http://www.nifs.ac.jp/report/nifs779.html
9. P.G. Burke and K. A. Berrington, *Atomic and Molecular Processes: An R-matrix Approach* (IOP, Bristol, 1993)
10. X. M. Tong, Z. X. Zhao and C. D. Lin, Phys. Rev. A **66**, 033402 (2002)

Radiation Reaction in Ultra-Intense Laser Fields

Contact *theinzl@plymouth.ac.uk*

Tom Heinzl
School of Computing and Mathematics, University of Plymouth, Plymouth PL4 8AA, UK

Chris Harvey
Department of Physics, Umeå University, SE-901 87 Umeå, Sweden

Introduction

The problem of classical radiation reaction (RR) has vexed generations of physicists since its first formulation in 1892 by Lorentz [1, 2]. Following important contributions by Abraham [3] and others the equation describing the back reaction of the radiation field on the motion of the radiating charge has been cast in its final covariant form by Dirac in 1938 [4]. It is now aptly called the Lorentz-Abraham-Dirac (LAD) equation. The relevant body of literature has become enormous and we refer to the recent monographs [5, 6] and, in particular, to the preprint [7] for an overview of the historical development and extensive lists of references. A particularly compact way of writing the LAD equation, say for an electron (mass m, charge e) is

$$m\dot{u} = F + \tau_0 \mathbb{P}\, m\ddot{u} \ , \tag{1}$$

where u denotes the electron 4-velocity, $F = e\mathbb{F}u/c$ the Lorentz 4-force in terms of the field strength tensor, $\mathbb{F}$, of the *externally prescribed* field and dots derivatives with respect to proper time, τ. The second term on the right is the RR force, F_{RR}, which is characterised by the appearance of the time parameter

$$\tau_0 = \tfrac{2}{3} r_e/c \simeq 2 \text{ fm}/c \simeq 10^{-23} \text{ s} \ . \tag{2}$$

This is the time it takes light to traverse the classical electron radius[1], $r_e = e^2/4\pi mc^2 = \alpha\lambda_C \approx 3$ fm. Obviously, the scales involved are typical for strong interactions (or quantum chromodynamics) – a first hint that the classical LAD equation (1) does not capture the physics at these (essentially quantum) scales. Finally, the projection $\mathbb{P}_{\mu\nu} = 1 - u_\mu u_\nu /c^2$ in (1) guarantees that 4-acceleration and velocity are Minkowski orthogonal. This follows upon differentiating the on-shell condition, $u^2 = c^2$, which, of course, is Einstein's first postulate on the universality of the speed of light, c. As u is time-like, its τ-derivative is space-like.

Estimating RR

The LAD equation (1) is of third order in time derivatives and hence suffers from a number of pathologies such as runaway solutions and pre-acceleration. One way to overcome this is by iteration, assuming that $F_{RR} << F$ which amounts to working to first order in τ_0. This in turn implies a 'reduction of order' in derivatives and results in the Landau-Lifshitz (LL) equation [8],

$$m\dot{u} = F + \tau_0 \mathbb{P}\, \dot{F} \ . \tag{3}$$

Hence, one replaces the problematic 'jerk' [9] term, $m\ddot{u}$, in (1) by the proper time derivative of the Lorentz force [6] where the acceleration term is evaluated to *lowest* order in τ_0, hence

$$\dot{F} = \frac{e}{c}\dot{\mathbb{F}}u + \frac{e^2}{mc^2}\mathbb{F}^2 u + O(\tau_0) \ . \tag{4}$$

[1] We employ Heaviside-Lorentz units with fine structure constant $\alpha = e^2/4\pi\hbar c = 1/137$.

For alternative derivations of the LL equation emphasising mathematical intricacies related to regularisations of the point particle concept we refer to [10, 11].

The LL equation (3) was derived under the assumption of a small reaction force, $F_{RR} << F$. Let us elucidate the physics involved somewhat further by assuming that the external field is produced by a laser modelled as a plane wave with light-like wave vector k, $k^2 = 0$. An electron 'approaching' the laser field with initial 4-velocity u_0 will, in its rest frame, 'see' a wave frequency given by the invariant scalar product,

$$\Omega_0 \equiv k \cdot u_0 \ . \tag{5}$$

Temporal gradients will then be of the order of the laser period, $dF/d\tau \sim \Omega_0 F$, so that the relative magnitude of the reaction force becomes

$$r \equiv \frac{F_{\rm RR}}{F} = \Omega_0 \tau_0 \ll 1 \ , \tag{6}$$

with the inequality required for the validity of the LL equation. Consider now a head-on collision in the lab where the laser frequency is measured to be ω,

$$k = \omega/c(1, \hat{\mathbf{z}}) \ , \quad u_0 = \gamma_0 c(1, -\beta\hat{\mathbf{z}}) \ , \tag{7}$$

with the usual relativistic gamma factor, $\gamma_0 = E_e/mc^2$ measuring the electron energy E_e in units of mc^2. Such an electron then 'sees' a laser frequency that is Doppler upshifted according to

$$\Omega_0 = \gamma_0(1+\beta)\omega \equiv e^\zeta \omega \simeq 2\gamma_0\omega \ , \tag{8}$$

the last identity holding for $\gamma_0 >> 1$.This boost in laser frequency is just the usual energy gain of a colliding versus fixed target mode (which, of course, are related by a longitudinal Lorentz boost with rapidity ζ). If we define dimensionless photon energies in the co-moving and lab frames,

$$\nu_0 \equiv \frac{\hbar\Omega_0}{mc^2} \ , \quad \nu \equiv \frac{\hbar\omega}{mc^2} \ , \tag{9}$$

the RR parameter r from (6) becomes

$$r = \tfrac{2}{3}\alpha\nu_0 \simeq \tfrac{4}{3}\alpha\gamma_0\nu \simeq 10^{-2}\gamma\nu \ . \tag{10}$$

For an optical laser $\nu \approx 10^{-6}$ so that $r \approx 10^{-8}\ \gamma_0$.Thus, to boost this to order unity (such that reaction equals Lorentz force) requires $\gamma_0 \approx 10^8$ i.e. electron energies of order $\approx 10^2$ TeV. These can only be produced in gamma-ray bursts, but not (currently) in labs. The ground breaking laser pair production ("matter from light") experiment SLAC E-144, for instance, was utilising the 50 GeV SLAC linear collider implying $\gamma_0 \approx 10^5$ and $r \approx 10^{-8}$ [12].

The standard way of quantifying radiation by accelerated charges is via Larmor's formula for the radiated power, the relativistic incarnation of which may be written as

$$P = -m\tau_0\dot{u}^2 > 0 \ , \tag{11}$$

and hence is of order τ_0. If we follow our philosophy of neglecting terms of order τ_0^2 it suffices to express the acceleration via just the Lorentz force,

$$m\dot{u} = F = e\mathbb{F}u/c \equiv eE \ , \tag{12}$$

where we have introduced the 4-vector E corresponding to the electric field 'seen' by the electron. Let us reemphasise here that we do not require the LL equation with its RR force, F_{RR}. Thus, if we assume transversality of our laser fields, $k\mathbb{F} = 0$, we

immediately derive a very useful conservation law by dotting k into (12),

$$\dot{\Omega} \equiv k \cdot \dot{u} = 0 \,. \tag{13}$$

Hence, without RR, the electron always 'sees' the same laser frequency on its passage through the laser beam,

$$\Omega = k \cdot u = k \cdot u_0 = \Omega_0 \,. \tag{14}$$

If we now plug the Lorentz equation (12) into (11) the average energy loss per (reduced) laser period $1/\Omega_0$ in units of mc^2 becomes

$$R \equiv \frac{\langle P \rangle}{\Omega_0 m c^2} = -r \frac{e^2 \langle E^2 \rangle}{m^2 c^2 \Omega_0^2} \equiv r a_0^2 \,. \tag{15}$$

Interestingly, we recover our RR parameter r from (6) and (10) *plus* a new quantity, the dimensionless laser amplitude a_0 which measures the energy gain of an electron traversing a laser wavelength, c/Ω_0, in an rms field E in units of mc^2. Obviously, when this (purely classical) parameter becomes of order unity, the electron motion is relativistic. Note that a_0 is both Lorentz and gauge invariant [13]. This is particularly obvious upon reexpressing a_0 in terms of a dimensionless field strength,

$$\hat{\mathbb{F}} \equiv e\mathbb{F}/mc\Omega_0$$

whereupon

$$a_0^2 = \frac{(u_0, \langle \hat{\mathbb{F}}^2 \rangle u_0)}{c^2} \,. \tag{16}$$

The energy loss parameter (15) was previously employed in [14–17]. It suggests that for substantial radiation the small RR parameter r needs to be compensated by large values of a_0^2. Denoting the current record intensity by $I_{22} = 10^{22}$ W/cm^2 we may write

$$a_0 = 60 \sqrt{I/I_{22}}\, \lambda_L/\mu\mathrm{m} \,, \tag{17}$$

so that one can envisage a_0 values of about 10^3 for the not too distant future [18,19]. We have seen already in (10) that large gamma factors (colliding mode) yield a further increase of radiative losses. In addition, the losses accumulate over successive laser periods. After, say, N cycles one expects a total relative change of the electron gamma factor given by

$$\frac{\Delta\gamma}{\gamma_0} = 2\pi N R = \frac{8\pi}{3} N \alpha \gamma_0 \nu a_0^2 \,, \tag{18}$$

where the smallness of $\alpha\nu \approx 10^{-8}$ may be compensated by pulse duration, N, initial electron energy, γ_0, and intensity, a_0^2.

Modelling the laser

The simplest model of a laser (beam) is provided by a plane wave with a field tensor depending solely on the invariant phase, $\mathbb{F} = \mathbb{F}(\varphi)$, $\varphi = k \cdot x$, and obeying transversality, $k\mathbb{F} = 0$. If we choose k as in (7) we have

$$\Omega = k \cdot u = \omega(u^0 - u^3)/c \equiv \omega u^-/c \,, \tag{19}$$

$$\phi = k \cdot x = \omega(x^0 - x^3)/c \equiv \omega x^-/c \,. \tag{20}$$

In other words, the laser field $\mathbb{F}$ only depends on the light-front or null coordinate, $x^- = ct - z$.

Plane waves are invariantly characterised as *null* fields [21, 22] as scalar and pseudoscalar invariants vanish,

$$\mathscr{S} \equiv \tfrac{1}{4}\mathrm{tr}\,\mathbb{F}^2 = 0 \,, \tag{21}$$

$$\mathscr{P} \equiv \tfrac{1}{4}\mathrm{tr}\,\mathbb{F}\tilde{\mathbb{F}} = 0 \,. \tag{22}$$

Hence, the energy momentum tensor of a plane wave is just $\mathbb{F}^2$.

$$c\mathbb{T} = \mathbb{F}^2 - \mathscr{S}\mathbb{1} = \mathbb{F}^2 \,. \tag{23}$$

This is the *only* nontrivial power of field strength as $\mathbb{F}$ is nilpotent with index 3, i.e. $\mathbb{F}^3 = 0$ which will be important when we solve the equations of motion in such a field. As a result it is important to note that there is no *intrinsic* invariant scale associated with a null field. In order to characterise them in an invariant fashion one needs a probe such as an electron or a (non-laser) photon. This naturally leads to the invariant amplitude a_0 as defined in (16) which explicitly depends on the probe electron 4-velocity. Defining the energy density of the laser 'seen' by the electron as

$$w_0 \equiv (u_0, c\mathbb{T}u_0)/c^2 = (u_0, \mathbb{F}^2 u_0)/c^2 = E^2 \,, \tag{24}$$

we see that (16) expresses just the dimensionless version of this energy density,

$$a_0^2 = \langle \hat{w}_0 \rangle \,. \tag{25}$$

Typically, the plane wave modelling the laser will be pulsed, i.e. of finite duration in invariant phase, φ. We accommodate this situation by parameterising $\mathbb{F}$ as follows. We assume the plane wave field to be linearly polarised along the space-like transverse 4-vector ε ($\varepsilon^2 = -1$) and hence decompose $\mathbb{F}$ into magnitude a_0, envelope $f = f(\varphi)$ and a constant tensor,

$$\mathbb{f} = n \wedge \epsilon - \epsilon \wedge n,$$

so that we have altogether

$$\hat{\mathbb{F}}(\phi) = a_0\, f(\phi)\, \mathbb{f} \,, \tag{26}$$

with the dimensionless constant 4-vector $n = kc/\Omega_0$ obeying $n^2 = 0 = n \cdot \varepsilon$ and $n \cdot u = n \cdot u_0 = c$. As a result,

$$\mathbb{f}^2 = n \wedge n \,,$$

with all higher powers vanishing due to $n^2 = 0$. In order for (26) to be consistent with (16) and (25) the average must be defined in such a way that f is normalized to unity. Defining a dimensionless gauge potential, $\hat{A} = eA/mc^2$, the field strength becomes

$$\hat{\mathbb{F}} = n \wedge \hat{A}' - \hat{A}' \wedge n \,, \tag{27}$$

the prime henceforth denoting the derivative with respect to invariant phase φ. Comparison with (26) finally yields $\hat{A}' = a_0 f \varepsilon$ and

$$a_0^2 = -\langle \hat{A}'^2 \rangle.$$

Solving the LL equation

Unlike the LAD the LL equation is a fairly standard equation of motion being second order in time derivatives. Hence, it requires two integrations and initial conditions for velocity and position. For the purposes of this contribution it will be sufficient to perform only the first integration for which we need to provide the initial 4-velocity, $u(0) = u_0$.

Neglecting RR

To set the stage for a later comparison we first briefly recall the solution without RR, i.e. of the Lorentz force equation of motion (12). We first note that for any function $f = f(\tau)$ of proper time we may trade derivatives according to

$$\dot{f} = f' \dot{\phi} = f' \Omega = f' \Omega_0 \,, \tag{28}$$

where, in the last step, we have used the conservation law (14). In terms of the dimensionless field strength (27) the Lorentz equation takes on the particularly compact form

$$u' = \hat{\mathbb{F}} u \,. \tag{29}$$

This is, of course, integrated by a matrix exponential which truncates at second order due to nilpotency, $\mathbb{F}^3 = 0$. Employing the parameterisation (26) the solution becomes

$$u = u_0 - c a_0 I_1 \epsilon + \left(a_0 I_1 \epsilon \cdot u_0 + \tfrac{1}{2} a_0^2 I_1^2 c \right) n \,, \tag{30}$$

where we have used the pulse shape integral

$$I_k \equiv \int_0^\phi d\varphi\, f^k(\varphi) \,, \tag{31}$$

for $k = 1$. Upon inspection of the solution (30) we note the following features. The velocity decomposes into transverse and longitudinal contributions given by the second and third terms on the right, respectively. If the initial velocity is longitudinal (like for a head-on collision) we have $\varepsilon \cdot u_0 = 0$. In this case, the longitudinal velocity is quadratic in a_0 while the transverse component is always linear.

At the cost of manifest gauge invariance one may rewrite the solution (30) in terms of the gauge potential $\hat{A}=a_0 I_1\,\varepsilon$ defined in (27) which results in the neat expression

$$u = u_0 - c\hat{A} + (\hat{A}\cdot u_0 - \tfrac{1}{2}\hat{A}^2 c)n \qquad (32)$$

From this expression one easily identifies the additional conserved quantity $\varepsilon\cdot(u + c\hat{A})$ corresponding to the transverse kinetic momentum. Both for fixed target and head-on collision modes there are no transverse components for the initial velocity, hence $\hat{A}\cdot u_0 = 0$. As $\hat{A}$ is space-like, $\hat{A}^2 < 0$, the quadratic contributions in (32) are actually positive.

Including RR

Upon including RR we have to solve the full LL equation (3) which we write in dimensionless notation as

$$\hat{\Omega}u' = \hat{\mathbb{F}}u + r(\hat{\Omega}\hat{\mathbb{F}}' + \hat{\mathbb{F}}^2 - \hat{w})u\ , \qquad (33)$$

with the abbreviations

$$\hat{\Omega} \equiv \Omega/\Omega_0 \text{ and } \hat{w} \equiv (u, \hat{\mathbb{F}}^2 u)/c^2,$$

cf. (24) and (25). As (33) seems highly nonlinear it may come as a surprise that, for plane wave background, there is still an analytic solution [15, 23]. Let us briefly review its main steps using our compact notation. In contradistinction to the previous subsection a non-vanishing RR force, $F_{RR} \neq 0$, entails that $\Omega = k\cdot u$ is no longer conserved, but rather

$$\hat{\Omega}' = -r\hat{w}^2 = -Rf^2\hat{\Omega}^2\ . \qquad (34)$$

This is possibly the most significant new feature: In the presence of RR the electron will see a *continuously changing* laser frequency during its passage through the pulse. Crucially, however, the equation (34) for the longitudinal velocity component completely decouples and, though nonlinear, can be solved by straightforward quadrature,

$$\hat{\Omega} = \frac{1}{1+RI_2} \simeq 1 - RI_2\ , \qquad (35)$$

with the $k = 2$ shape integral from (31) and the initial condition $\Omega(0) = \Omega_0$. It is worth noting that the RR parameter R from (15) appears at this stage. As $R \sim \tau_0$ we should actually use the ultimate expression in (35) in keeping with our philosophy of neglecting terms of order τ_0^2. In any case we would like to point out that (35) is a particularly nice signature for RR as the right-hand side differs from unity only when a substantial amount of RR is present. In more physical terms, $\Omega \neq \Omega_0$ signals *symmetry breaking* in the following sense. Together with the longitudinal velocity $u^0 - u^3 \sim \Omega$, cf. (19), the longitudinal momentum, $p^- = p^0 - p^3$, ceases to be conserved. As a result RR induces a breaking of translational invariance in the conjugate null direction[2] $x^+ = x^0 + x^3$.

Let us continue with the LL equation and the remaining velocity components. The crucial technical trick is to introduce a new 4-velocity v via

$$v \equiv \hat{\Omega}^{-1}u = (1 + RI_2)u\ , \qquad (36)$$

the longitudinal component of which is again conserved, $k\cdot v = \Omega_0$. Using (34) it is straightforward to see that the LL equation for v simplifies to

$$v' = (\hat{\Omega}^{-1}\hat{\mathbb{F}} + r\hat{\mathbb{F}}' + r\hat{\Omega}^{-1}\hat{\mathbb{F}}^2)v\ , \qquad (37)$$

As we know the solution (35), which is independent of v, this equation is indeed *linear* in v and easily solved via exponentiation. Using the parameterisation (26) once more and noting that $u_0 = v_0$, the solution for v may be written as

$$v = u_0 - ca_0 J_1\epsilon + \big(a_0 J_1\epsilon\cdot u_0 + \tfrac{1}{2}a_0^2 J_1^2 c + RJ_2 c\big)\ n\ , \qquad (38)$$

with the new shape integrals (suppressing the measure $d\varphi$),

$$J_k \equiv \int_0^\phi \hat{\Omega}^{-1} f^k = I_k + R\int_0^\phi I_2 f^k\ , \qquad (39)$$

$$K_1 \equiv J_1 + rf\ . \qquad (40)$$

Comparing (38) and (30) one can identify precisely the same vector structure, the analogous longitudinal and transverse terms guaranteeing $k\cdot v = k\cdot v_0 = \Omega_0 = const$. In the limit of no RR ($\tau_0 \to 0$) one has $K_1 \to I_1$ and $J_2 \to 0$ such that (30) is readily recovered. In the non-relativistic limit one neglects terms of order a_0^2 (hence R) so that (38) becomes

$$u_{\rm NR} = u_0 - c(\hat{A} + r\hat{A}') + (\hat{A} + r\hat{A}')\cdot u_0\, n\ . \qquad (41)$$

which differs from (32) by the (small) $r\hat{A}'$ terms. The analogue of this equation for a Coulomb background has recently been used to discuss the classical Coulomb problem with RR [24].

As a final comment we note that the dependence on proper time τ is recovered by integrating (35) which gives

$$\Omega_0\tau = J_0 = \phi + R\int_0^\phi d\varphi\, I_2(\varphi)\ . \qquad (42)$$

Hence, in proper time τ, RR leads to a phase shift compared to the Lorentz solution [23] as τ is no longer proportional to the invariant phase, φ.

An analytic example

With the analytic solution (38) of the LL equation at hand we can readily analyse an example. The only remaining technical difficulty is the evaluation of the pulse shape integrals (31), (39) and (40). It turns out that they may be performed analytically for the pulse shape function

$$f(\phi) \equiv \begin{cases} \sin^4(\phi/2\pi N)\sin(\phi)\ , & 0 \le \phi \le 2\pi N\ , \\ 0 & \text{else} \end{cases} \qquad (43)$$

originally suggested in [25] (see also [26]). The pulse (43) has a duration of $\varphi_0 = 2\pi N$ (hence contains N cycles) and vanishes identically outside this interval. Thus, unlike a sine modulated Gaussian [23], it has compact support (see **Fig. 1**).

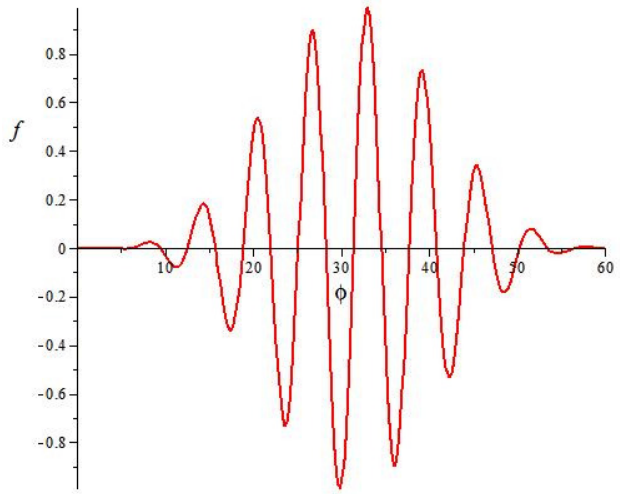

Fig. 1: *Laser pulse* (43) *for N = 10 as a function of invariant phase, φ.*

We are only interested in the behaviour of the symmetry breaking parameter (35). For this we need the integral I_2, which is

[2] Recall the scalar product:
$p\cdot x = p^+x^-/2 + p^-x^+/2 - \boldsymbol{p}_\perp\cdot\boldsymbol{x}_\perp$.

$$I_2 = \begin{cases} \frac{35}{256}\phi + \delta I_2 & 0 \le \phi \le \phi_0 \\ \frac{35}{256}\phi_0 & \text{else} \end{cases} . \qquad (44)$$

The term δI_2 in (44) denotes a series of small amplitude sine functions which we do not display. All we need to know is that they vanish at the 'end' of the pulse, $\delta I_2(\varphi_0) = 0$. Hence, inside the pulse $\Omega/\Omega_0 = 1 - RI_2$ drops linearly with small oscillations superimposed until it reaches a final plateau. For parameter values $\gamma_0 = 100$, $a_0 = 150$, $\nu = 10^{-6}$ (implying $R = 0.022$) and $N = 10$ the resulting behaviour is shown in **Fig. 2**.

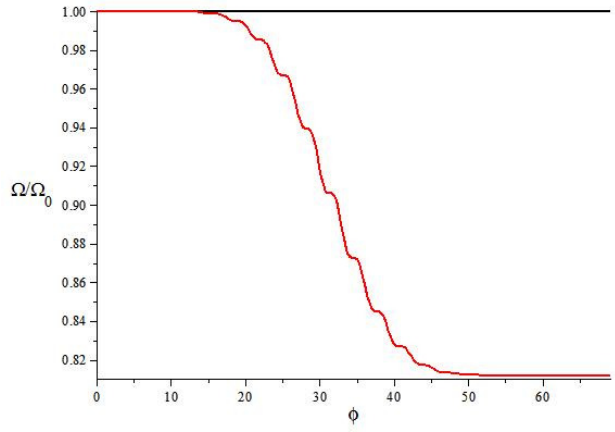

Fig. 2: *Laser frequency* $\Omega/\Omega_0 = 1 - RI_2$ *as 'seen' by the electron during the passing of an N =10 pulse as a function of invariant phase, φ. Black line: Constant result* (14) *without RR. Red line: RR Solution* (35).

From (44) the final plateau value, once the pulse has passed, is given by the simple expression

$$\hat{\Omega}_f = 1 - RI_2(\phi_0) = 1 - 2\pi N \frac{35}{256} R . \qquad (45)$$

For the parameter values of **Fig. 2** the plateau value is 0.81. In general, assuming a head-on collision with $\gamma_0 >> 1$ one has $\Omega_0 \approx 2\gamma_0$, $\Omega_f \approx 2\gamma_f$ and the total relative energy loss becomes

$$\frac{\Delta\gamma}{\gamma_0} \simeq 1 - \hat{\Omega}_f = \frac{35}{256} \times 2\pi NR . \qquad (46)$$

Apart from the numerical coefficient this is precisely our prediction (18) based on Larmor's formula.

Conclusions

We have re-analysed the problem of radiation reaction by solving the Landau-Lifshitz equation analytically for an electron in an intense plane wave laser field. Such a field depends solely on the invariant phase, $\varphi = k \cdot x$ or, with the laser wave vector **k** pointing in z direction, on the light-front coordinate $x^- = ct - z$. A particularly useful signature for radiation reaction is the laser frequency as 'seen' by the electron, $\Omega = k \cdot u$. This ceases to be conserved when radiation reaction is present, thus signalling symmetry breaking: Translational invariance in the light-front coordinate $x^+ = ct + z$ is violated. For a pulsed plane wave of finite duration in x^- the total change in Ω (hence in longitudinal momentum, p^-) obtained from the Landau-Lifshitz equation is well described by Larmor's formula for the radiated power.

We end our discussion with a caveat. While the discussion above is consistent one expects, in view of the small length and time scales and the huge field gradients involved, that all classical effects will be accompanied (if not overwhelmed) by quantum ones. Whether these can be disentangled, say by looking at special observables or kinematics, remains to be seen. A thorough analysis of this question will have to be given elsewhere.

Acknowledgements

The authors thank Kurt Langfeld and Nicloa Iji for a fruitful (and ongoing) collaboration on radiation reaction. C. H. was supported by the Swedish Research Council Contract #2007-4422 and the European Research Council Contract #204059-QPQV.

References

1. H.A. Lorentz, *La Théorié Electromagnétique de Maxwell et son Application aux Corps Mouvants*, Arch. Neérl. **25**, 363-552 (1892), reprinted in Collected Papers (Martinus Nijhoff, The Hague, 1936), Vol. II, pp. 64-343.
2. H.A. Lorentz, *The Theory of Electrons*, B.G. Teubner, Leipzig, 1906; reprinted by Dover Publications, New York, 1952 and Cosimo, New York, 2007.
3. M. Abraham, *Theorie der Elektrizität*, Teubner, Leipzig, 1905.
4. P.A.M. Dirac, Proc. Roy. Soc. A **167**, 148-169 (1938).
5. H. Spohn, *Dynamics of Charged Particles and their Radiation Field*, Cambridge University Press, Cambridge, 2004.
6. F. Rohrlich, *Classical Charged Particles*, 3rd ed., World Scientific, Singapore, 2007.
7. K.T. McDonald, *Limits on the Applicability of Classical Electromagnetic Fields as Inferred from the Radiation Reaction*, unpublished preprint, available from: http://www.hep.princeton.edu/~mcdonald/examples/
8. L.D. Landau and E.M. Lifshitz, *The Classical Theory of Fields* (Course of Theoretical Physics, Vol. 2), Butterworth-Heinemann, Oxford, 1987.
9. J.G. Russo and P.K. Townsend, J. Phys. A **42**, 445402 (2009).
10. H. Spohn, Europhys. Lett. **49**, 287 (2000).
11. S.E. Gralla, A.I. Harte and R.M. Wald, Phys. Rev. D **80**, 024031 (2009).
12. C. Bamber *et al.*, Phys. Rev. D **60**, 092004 (1999).
13. T. Heinzl and A. Ilderton, Opt. Commun. **282**, 1879 (2009).
14. J. Koga, T.Zh. Esirkepov and S.V. Bulanov, Phys. Plasmas **12**, 093106 (2005).
15. A. Di Piazza, Lett. Math. Phys. **83**, 305 (2008).
16. A. Di Piazza, K.Z. Hatsagortsyan and C.H. Keitel, Phys. Rev. Lett. **102**, 254802 (2009).
17. Y. Hadad *et al.*, Phys. Rev. D **82**, 096012 (2010).
18. The Vulcan 10 Petawatt Project: http://www.clf.rl.ac.uk/New+Initiatives/14764.aspx
19. The Extreme Light Infrastructure (ELI) project: http://www.extreme-light-infrastructure.eu
20. T. Heinzl, Lect. Notes Phys. **572**, 55-142 (2001).
21. J.L. Synge, University of Toronto Applied Mathematics Series, No. 1 (Univ. of Toronto Press, 1935).
22. H. Stephani, *Relativity: An Introduction to Special and General Relativity*, Cambridge University Press, Cambridge, 2004.
23. C. Harvey, T. Heinzl, N. Iji, K. Langfeld, Phys. Rev. D **83**, 076013 (2011).
24. S.G. Rajeev, Annals Phys. **323**, 2654-2661 (2008).
25. F. Mackenroth, A. Di Piazza, C.H. Keitel, Phys. Rev. Lett. **105**, 063903 (2010).
26. T. Heinzl, A. Ilderton, M. Marklund, Phys. Lett. B **692**, 250-256 (2010).

Time-dependent R-matrix theory for ultra-fast processes

Contact *h.vanderhart@qub.ac.uk*

S. Hutchinson

Centre for Theoretical Atomic, Molecular and Optical Physics, Queen's University Belfast, Belfast BT7 1NN, United Kingdom

A. C. Brown

Centre for Theoretical Atomic, Molecular and Optical Physics, Queen's University Belfast, Belfast BT7 1NN, United Kingdom

H.W. van der Hart

Centre for Theoretical Atomic, Molecular and Optical Physics, Queen's University Belfast, Belfast BT7 1NN, United Kingdom

Introduction

Over the last ten years, substantial experimental effort has been devoted to the study of atomic and molecular processes on ultra-short timescales. At the heart of these developments lies harmonic generation, since ultra-short pulses are created through the superposition of several harmonics created by the same pulse [1]. Harmonic generation can also be used as a measurement tool, for example, to study molecular changes on the sub-femtosecond timescale [2], and to obtain information about molecular structure [3]. Harmonic generation has been used to explore the importance of ultra-fast multi-electron dynamics in molecules [4] and in atomic systems [5].

The most widely used approximation in theoretical work devoted to atoms in strong fields is the single-active-electron approximation. Within this approximation, only a single electron can respond to the laser field. This approximation is clearly invalid if we aim to investigate the influence of electron correlation on the dynamics. However, it can be shown that even sophisticated two-electron approaches are insufficient to describe the full influence of electron-electron interactions on multi-electron dynamics. It is therefore important to develop approaches, which can describe these interactions and their effects on multi-electron dynamics in full detail. Over the last five years, we have developed such an approach: the time-dependent R-matrix (TDRM) approach.

Time-dependent R-matrix theory

The TDRM approach solves the time-dependent Schrödinger equation by partitioning the configuration space into an inner and outer region with a shared boundary at $r = a_0$ [6,7]. Within the inner region, exchange and correlation effects are included for all of the electrons in the system under investigation. Within the outer region, the ejected electron is well separated from the residual ion. Thus the outer electron interacts with the remaining ion only through long-range direct interactions.

Within the inner region, the wavefunction is expressed through an R-Matrix basis expansion [8]. The wavefunction is propagated using a Crank-Nicolson scheme, which requires the solution of a system of linear equations at each time step. Solving this system of equations at time $t = t_q$, we calculate the R-matrix **R** and a T-Vector **T** on the boundary $r = a_0$ [6]. Both the R-matrix and the T-vector represent wavefunction flow through the boundary: the T-vector represents flow for the known wavefunction at time t_q, and the R-matrix flow for the (yet unknown) wavefunction at time t_{q+1}.

In the outer region $a_0 \leq r \leq a_p$, we solve a set of coupled differential equations describing the motion of the ejected electron in the presence of the light field by subdividing into *p* equally sized sub regions. Following solution of this set of equations, we propagate the R-matrix and T-vector across the boundaries of each sub region. Using **R** and **T**, along with the boundary condition stating that the wave function is zero at $r = a_p$, we propagate the wave function at $t = t_{q+1}$ inwards across all of the sub regions. We then use this wave function as the start for the next iteration.

Electron dynamics in C^+

The TDRM method has been applied successfully to describe correlated electron dynamics in a C^+ ion with magnetic quantum number M=0 [9,10]. A pump-probe scheme was employed to observe the ultrafast dynamics of a $2s2p^2$ wavepacket both in the ionization probability [9] and in momentum distributions coupled to the residual $^3P^o$ target state of the C^{2+} ion [10]. As the dynamics is primarily confined to the $2s2p^2$ configuration, it is predominantly driven by repulsion between the two electrons.

While the restriction of the total magnetic quantum number to M=0 is appropriate for targets with filled valence shells, such as noble gas atoms, general targets with open valence shells, such as C^+, can be in an initial state with a non-zero value for M. As a consequence, multi-electron dynamics for systems with M≠0 has so far not been investigated thoroughly, even though there may be fundamental changes to the dynamics.

We have therefore extended time-dependent R-matrix theory to the case that M≠0 [11]. This requires some modifications to the codes since ΔL=0 transitions are allowed for non-zero M, whereas they are not allowed for M=0. We demonstrate this code by extending our earlier work in the description of $2s2p^2$ dynamics in C^+ to the case that M=1. This changes the $2s2p^2$ dynamics fundamentally: from spatial dynamics for M=0 to spin dynamics for M=1. The pump-probe scheme is the same as in our previous study for M=0, with a pump laser photon energy of 10.9 eV and a probe laser photon energy of 16.3 eV. Both pump and probe laser pulse have a six-cycle $\sin^2$ profile.

Results

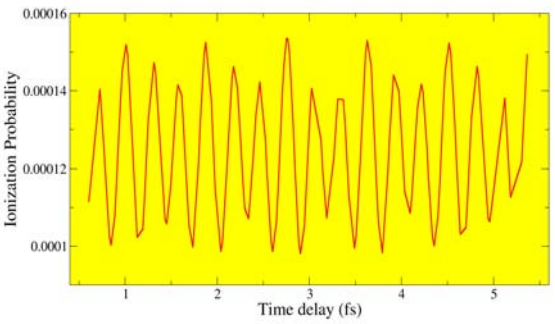

Figure 1. Ionization probability of C^+ in a 10.9-16.3 eV pump-probe scheme as a function of time delay between the two six-cycle pulses.

For the pump-probe scheme described above, figure 1 shows the obtained ionization probabilities over a range of time delays between the laser pulses. At the photon energies used, we observe an ultrafast oscillation with a period of approximately 0.3fs, along with a weak longer period behaviour with a period

of approximately 0.9 fs. The oscillation with a period of 0.3 fs is due to interference between ionization through absorption of one pump-pulse photon and one probe-pulse photon and ionization through absorption of two probe-pulse photons. The oscillation with a period of 0.9 fs is due to dynamics within the $2s2p^2$ configuration.

To analyse the dynamics within the $2s2p^2$ configuration, it is easiest to transform from the LS-coupled basis to the uncoupled basis in which the wavefunction is expressed as a product of one-electron functions. The basis functions in the uncoupled basis can be written as $|2s_0^+2p_1^+2p_0^-\rangle$, $|2s_0^+2p_1^-2p_0^+\rangle$, and $|2s_0^-2p_1^+2p_0^+\rangle$, where the subscript indicates magnetic quantum number m and the superscript $m_s=\pm½$. The population in the basis state $|2s_0^-2p_1^+2p_0^+\rangle$ remains constant in time, but the population in the other two states oscillates with a period of 0.9 fs. The minimum in the peak ionization yields corresponds closely to a maximum in the population in the uncoupled basis state $|2s_0^+2p_1^+2p_0^-\rangle$. The main reason for this is that excitation to the $2s2p(^1P^o)3s$ state is not allowed for this state. This autoionizing state plays a key role in the ionization process, so that ionization is reduced when excitation of this state from the $2s2p^2$ configuration is reduced.

Harmonic generation in TDRM

As mentioned earlier, one of the fundamental processes arising from light-matter interaction is harmonic generation. The theoretical description of harmonic generation in real atoms poses a serious challenge to current theory, since it becomes increasingly difficult for complex atoms to describe multi-electron effects adequately. The TDRM approach is, however, uniquely suited to provide an accurate description of multi-electron dynamics. We have therefore developed an extension to the TDRM code to obtain the harmonic response of a system.

Harmonic generation arises from the oscillating dipole moment induced during laser-atom interactions. The harmonic spectrum is thus obtained from the Fourier transform of the time-dependent expectation value of the electric dipole operator, $d(t) = -e\langle\Psi(t)|R|\Psi(t)\rangle$, where R is the total position operator. We note that the expectation value of the dipole acceleration operator is more commonly used to obtain the harmonic spectrum, but we find that this operator is less suitable for multi-electron systems.

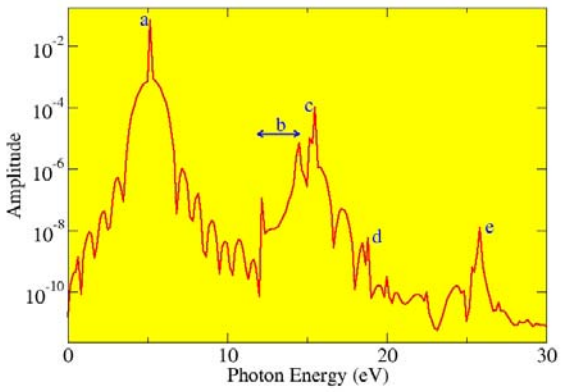

Figure 2. The harmonic spectrum produced by Ar irradiated by a 25 cycle, 2×10^{13} Wcm^{-2} laser pulse of frequency 5.17eV. The labelled features include (a) the first harmonic peak, (b) the $3s^23p^5n\ell$ Rydberg series, (c) the third harmonic peak, (d) a peak arising from the $3s^23p^54p$ state after absorption of a photon, and (e) the fifth harmonic peak.

Results

In order to investigate the suitability of the TDRM approach for the determination of harmonic generation, we investigate the harmonic spectrum obtained after an Ar atom interacts with 2×10^{13} Wcm^{-2} laser light with a photon energy around 5.17 eV. The basis used for the description of Ar is given in [12].

Figure 2 shows the harmonic spectrum obtained at an incident laser pulse with a photon energy of 5.17 eV. The lowest three odd-harmonic peaks can be identified easily. However, the spectrum shows several additional features which are due to the atomic structure of Ar. In the photon energy region between 12 and 15 eV, the $3s^23p^5n\ell$ Rydberg series influences the harmonic spectrum. With a pulse length of 25 cycles, we can separate out 3d/4s, and 4d/5s from higher-lying states, but we cannot separate the contributions from 3d and 4s. The peak at 18.8 eV can not be associated directly with any state of Ar directly, but it corresponds to the energy obtained after absorption of a single photon from $3s^23p^54p$. The fifth harmonic lies close to the $3s3p^6n\ell$ Rydberg series and we find that it is strongly influenced by this Rydberg series. In particular, by varying the frequency of the incident laser pulse we can investigate how this series affects the fifth harmonic [13].

Conclusions

Time-dependent R-matrix theory is a promising approach for the study of multi-electron dynamics on ultra-short timescales. In this report, we have shown how it can be used to explore whether spin dynamics involving three electrons can be observed in ultra-fast excitation of the $2s2p^2$ configuration, and how the approach can be exploited to investigate harmonic generation in multi-electron atoms

Acknowledgements

SH and ACB acknowledge financial support from the Department of Employment and Learning (NI) through the Programme for Government. HvdH acknowledges support from EPSRC through grant EP/G055416/1.

References

1. P M Paul *et al*, *Science* **292** 5522 (2001)
2. S Baker *et al*, *Science* **312** 5772 (2006)
3. J. Itatani *et al*, *Nature* **432** 867 (2004)
4. O. Smirnova *et al*, *Nature* **460**, 972 (2009)
5. A D Shiner *et al*, *Nat. Phys.* **7** 464 (2011)
6. M. A. Lysaght, H. W. van der Hart and P. G. Burke, *Phys. Rev. A* **79** 053411 (2009)
7. M.A. Lysaght, P.G. Burke and H.W. van der Hart, *Phys. Rev. Lett.* **101** 253001 (2008)
8. P.G. Burke and K.A. Berrington, *Atomic and Molecular Processes: an R-matrix approach* (Bristol: Institute of Physics Publishing, 2003)
9. M. A. Lysaght, P.G. Burke and H. W. van der Hart, *Phys. Rev. Lett.* **102** 193001 (2009)
10. M. A. Lysaght, S. Hutchinson and H. W. van der Hart, *New J. Phys.* **11** 093014 (2009)
11. S. Hutchinson *et al*, to be published (2011)
12. P G Burke and K T Taylor, *J. Phys. B: At. Mol. Opt. Phys.* **8** 2620 (1975)
13. A. C. Brown *et al*, to be published (2011)

Molecular Dynamics simulations for the viscosity of non-ideal plasmas

Contact *james.mithen@physics.ox.ac.uk*

Author 1 J. P. Mithen

University of Oxford, Clarendon Laboratory, Parks Road, Oxford, OX1 3PU

Author 2 J. Daligault

Theoretical Division, Los Alamos National Laboratory, Los Alamos, NM, 87545, USA

Author 3 G. Gregori

University of Oxford, Clarendon Laboratory, Parks Road, Oxford, OX1 3PU

Introduction

Viscosity is a fundamental characteristic property of all liquids. Recently, it was shown by the present authors that the viscosity of non-ideal plasmas - which have liquidlike properties - could in principle be measured in x-ray scattering experiments on laser produced plasmas [1]. With this in mind, it is desirable to have theoretical estimates of the viscosity of non-ideal plasmas. In this contribution, we will describe two methods for computing the viscosity and present numerical results.

Both of the methods we describe - the "Green-Kubo method" and the "Hydrodynamic method" - rely on large scale, accurate Molecular dynamics (MD) simulations. In the present instance, these simulations have been performed for the Yukawa system, which is a fluid of particles, mass m, with interaction potential $v(r)=(Ze)^2\exp(-r/\lambda_s)/4\pi\epsilon_0 r$. The particles in this system represent interacting ions of charge Ze; the bare Coulomb interactions between the ions are screened by the electrons. The electronic screening length λ_s reduces to either the Debye length or the Thomas-Fermi distance in the limiting cases of classical and degenerate electron fluid respectively [2]. This system, often called the Yukawa one-component plasma (YOCP), is known to be fully characterised by two dimensionless parameters only [3]: the coupling strength

$$\Gamma=\frac{(Ze)^2}{(4\pi\epsilon_0 k_b T)} \quad ,$$

where T is the temperature, and the screening parameter

$$\alpha=\frac{a}{\lambda_s} \quad ,$$

where $a=(4\pi n/3)^{-1/3}$ with n the density. For $\Gamma\geq 1$, the system represents a 'non-ideal' or 'strongly coupled' plasma; at these coupling parameters the standard results of high temperature plasma physics are no longer applicable. The YOCP represents a highly simplified description of such a non-ideal plasma consisting of ions and electrons. Nevertheless, it is certainly a useful model with which to investigate the properties of these states of matter.

As will be elucidated in the following sections, the viscosity of the YOCP can be calculated by computing its *equilibrium* dynamics. In order to compute these dynamics we use MD simulations [4]. First, we choose values for Γ and α. For the calculations presented in this contribution, we have chosen a fixed value of $\alpha=2$ - which is often a reasonable estimate of the screening parameter for a typical non-ideal laser produced plasma - and performed simulations for a range of Γ values (1, 5, 10, 50, 120 and 175) in order to compute the viscosity for a range of thermodynamic conditions. In our simulations, we perform a long equilibration of duration $1000\omega_p^{-1}$, where $\omega_p=\sqrt{n(Ze)^2/\epsilon_0 m}$ is the plasma frequency of the system (our timestep is $\delta t=0.01\omega_p^{-1}$). After this equilibration, we record the positions and velocities of the $N=5000$ particles for a further time of $30\times 819.1\,\omega_p^{-1}$. From the particle positions and velocities we can calculate the time-dependent correlation functions introduced in the following sections (we split the simulation into 30 parts, compute correlation functions for each part, and average in order to improve statistics). Each of the two methods for computing the viscosity, as outlined in the following sections, involves computation of a different time-dependent correlation function.

Green-Kubo method

A standard way to compute the viscosity of a fluid is to use the following "Green-Kubo relation" in which the shear viscosity η is expressed in terms of the time integral of the shear stress autocorrelation function $\eta(t)$ [5],

$$\eta=\int_0^\infty \eta(t)dt=\frac{1}{k_B T V}\int_0^\infty <\sigma^{zx}(0)\sigma^{zx}(t)>dt \quad . \qquad (1)$$

In Eq. (1), V is the volume of the system (in our case the volume of the simulation box). The brackets $<...>$ denote the usual statistical (thermal) average. The shear stress autocorrelation function is given in terms of the zx component of the microscopic stress tensor,

$$\sigma^{zx}(t)=\sum_{i=1}^{N}[mv_{i,z}(t)v_{i,x}(t)-\frac{1}{2}\sum_{j=1\neq i}^{N}(z_{ij}x_{ij}/r_{ij})v'(r_{ij})] \qquad (2)$$

where $v_{i,z}(t)$ is the z component of velocity of particle i at time t, and $x_{ij}=|x_i(t)-x_j(t)|$. Eq. (1) is a particular example of a "Green-Kubo relation" in which a transport coefficient of a fluid is expressed in terms of a time integral of a microscopic correlation function.

We compute σ^{zx} at each timestep using the positions and velocities from our MD simulations. We can then compute $<\sigma^{zx}(0)\sigma^{zx}(t)>$ by replacing the statistical average by a time average [4], i.e.

$$<\sigma^{zx}(0)\sigma^{zx}(t)>=\lim_{T\to\infty}\frac{1}{T}\int_0^T \sigma^{zx}(\tau)\sigma^{zx}(t+\tau)d\tau \quad . \qquad (3)$$

In this way the shear stress autocorrelation function $\eta(t)$ appearing in Eq. (1) can be computed. The time integral of $\eta(t)$ then gives the shear viscosity η (see Eq. (1)).

In Fig. 1, we show typical MD results for the normalised shear stress autocorrelation function and the normalised shear viscosity, which are both dimensionless and defined by

$\hat{\eta}(t)=\eta(t)/nma^2\omega_p^2$ and $\hat{\eta}=\eta/nma^2\omega_p$ respectively.

As shown in Fig. 1, because of noise in the computed shear stress autocorrelation function, the upper limit in the integral in Eq. (1) must be replaced by some cutoff time t_{cutoff}, which is less than the total simulation time of $819.1\omega_p^{-1}$. We find that this cutoff time must be chosen differently for each Γ; the arbitrary choice of t_{cutoff} is a somewhat undesirable necessity of the Green-Kubo method. Despite this, we find that our simulations are long enough that the final result for the viscosity is not particularly sensitive to the choice of t_{cutoff}, providing t_{cutoff} is selected to be close to the time at which

the MD result shear stress autocorrelation function appears to decay to zero (see Fig. 1) .

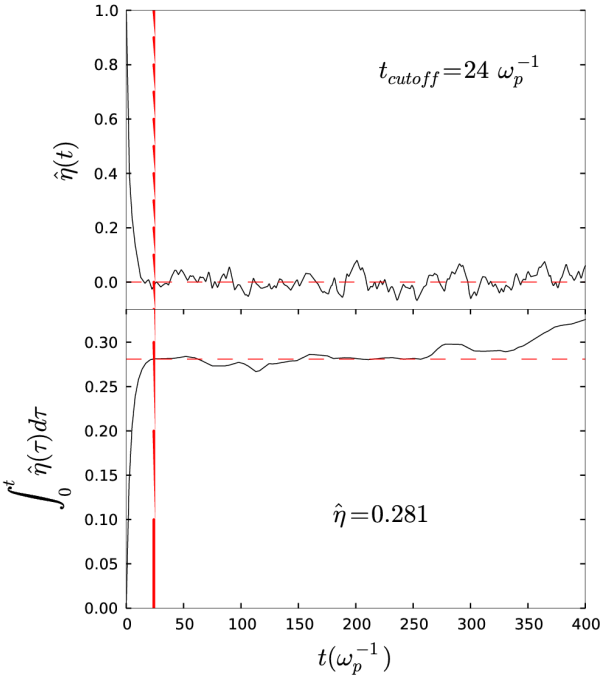

Figure 1: Illustration of the Green-Kubo method for determining the viscosity for $\Gamma=5,\alpha=2$. The top panel shows the decay of the shear stress autocorrelation function, and the time after which it is effectively set to zero for the purpose of computing the viscosity (vertical line). The bottom panel shows the cumulative integral of this quantity, which gives a value for the viscosity as indicated by the dashed horizontal line.

Hydrodynamic method

The "hydrodynamic method" for computing the shear viscosity, as we shall refer to it here, is based on the transverse part of the linearized Navier-Stokes equation. This can be written in terms of the wavevector and time dependent transverse current correlation function, $C_t(k,t)$ [6],

$$\frac{\partial}{\partial t}C_t(k,t)=-\frac{\eta}{nm}k^2 C_t(k,t) \qquad (4)$$

where the transverse current correlation function is defined as [7]

$$C_t(k,t)=\frac{1}{N}<\sum_{i=1}^{N}\sum_{j=1}^{N} v_{i,x}(t)v_{j,x}(0)e^{ik(z_i(t)-z_j(0))}> \quad . \qquad (5)$$

From Eq. (4), one obtains an exponential decay for the transverse current correlation function,

$$\frac{C_t(k,t)}{C_t(k,0)}=e^{-\frac{\eta}{nm}k^2 t} \quad . \qquad (6)$$

The hydrodynamic method consists of computing $C_t(k,t)$ with MD and then using Eq. (6) to estimate the shear viscosity. To achieve this, as in the case of the Green-Kubo method (cf Eq. (3)), the statistical average in Eq. (5) is taken as a time average. Then, since the only unknown parameter in Eq. (6) is the shear viscosity η , the MD result for $C_t(k,t)$ can be fitted to an exponential decay to yield our best estimate of the shear viscosity.

In Fig. 2, we show typical MD results for the transverse current correlation function along with the exponential fit that allows the shear viscosity to be estimated. As shown in Fig. 2, we apply the exponential fit to only a particular time interval, denoted by t_{fit} . The upper limit of this region, which we have chosen as $200\omega_p^{-1}$, is required because of the deteriorating quality of the MD data: as time increases in Fig. 2, fewer averages contribute to the transverse current correlation function, and therefore the MD data becomes more noisy. The reason that a lower limit on the time interval is required is instead a physical one. Since the hydrodynamic description, on which Eqs. (4) and (6) are based, is only applicable for dynamics occurring on long time and length scales, only at sufficiently long times should $C_t(k,t)$ be expected to decay exponentially as in the hydrodynamic description. Indeed, we find that the short time behaviour of $C_t(k,t)$ as computed from our MD simulations can be seen to be Gaussian (as expected) rather than exponential. Our chosen lower limit of $50\omega_p^{-1}$ ensures that this non-hydrodynamic behaviour of $C_t(k,t)$ at short times does not influence our fit for the shear viscosity. As for long length scales, this implies that the wavevector k is small. In a previous work [1], the present authors quantified exactly how small the wavevector k must be for the hydrodynamic description to apply for the Yukawa system: the maximum wavevector k_{max} at which the Navier-Stokes equation is valid was found to be given approximately by $k_{max}\lambda_s\approx 0.43$. For $\alpha=2$, this criterion gives $k_{max}a\approx 0.86$. For our viscosity calculations, we have computed $C_t(k,t)$ at $ka=0.23$. Thus we are computing the transverse current correlation function at wavevectors much smaller than k_{max} , and we expect the hydrodynamic description to be very accurate. This expectation is confirmed by our MD data – as shown in Fig. 2, the exponential decay given by Eq. (6) fits the MD data very well.

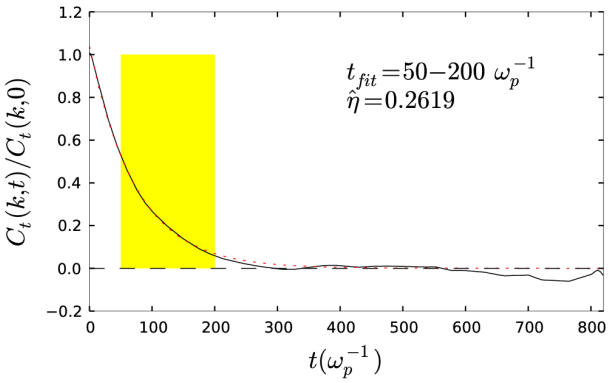

Figure 2: Normalised transverse current correlation function (solid line) for $\Gamma=5,\alpha=2$ and $ka=0.23$ along with the exponential fit (dotted line). The fitted region is shaded.

Comparison between methods

As shown in Fig. 3, for $\alpha=2$ both the "Green-Kubo method" and the "hydrodynamic method" give similar results for the shear viscosity. We see no reason that this should not be the case for all values of α ; we are currently undertaking further simulations at other α values to confirm this.

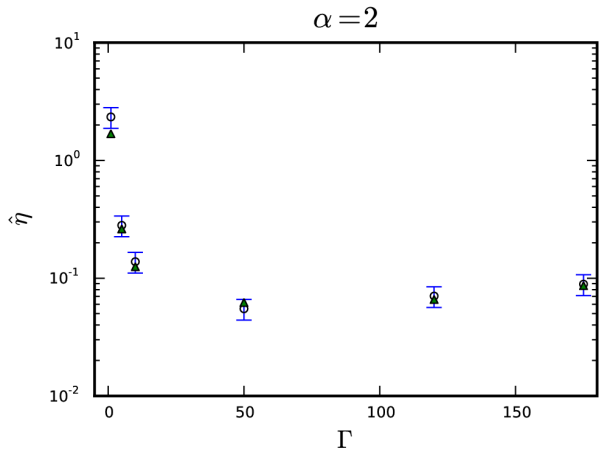

Figure 3: Comparison of viscosity as computed by the Green-Kubo method (open circles, with 20% error bars) and the hydrodynamic method (filled triangles).

Concluding Remarks

In this contribution we investigated two methods for computing the viscosity of non-ideal plasmas using Molecular Dynamics simulations. As our model of a non-ideal plasma we took the Yukawa one-component plasma. Our work demonstrated that the hydrodynamic method for computing the viscosity is feasible and therefore complements the more widely used method based on the Green-Kubo relation. That is to say, this alternative method provides a way to validate the Green-Kubo result. Furthermore, we expect that in the future our viscosity calculations will be used to assist with the interpretation and analysis of x-ray scattering experiments, which could in principle measure this fundamental physical quantity.

Acknowledgements

This work was supported by the John Fell Fund and by EPSRC grant no. EP/G007187/1.

References

1. J. P. Mithen, J. Daligault and G. Gregori, *Phys. Rev. E* **83**, 015401(R); see also the article “Hydrodynamics of the Yukawa One Component Plasma” (CLF Annual Report 2009-2010).
2. D. Kremp, M. Schlanges and W. D. Kraeft, *Quantum Statistics of Nonideal Plasmas* (Springer-Verlag, Berlin, 2005).
3. Z. Donkó, G. J. Kalman and P. Hartmann, *J. Phys.: Consens. Matter* **20**, 413101 (2008).
4. See e.g. M. P. Allen and D. J. Tildesley, *Computer simulation of liquids* (Oxford, New York, 1987).
5. U. Balucani and M. Zoppi, *Dynamics of the Liquid State*, (Oxford, 1994).
6. J. P. Boon and S. Yip, *Molecular Hydrodynamics*, (Dover, 1991).
7. J. P. Hansen, I. R. McDonald and E. L. Pollock, *Phys. Rev. A* **11**, 1025 (1975).

Kinetic theory of radiation reaction

Contact *adam.noble@strath.ac.uk*

Adam Noble & Dino Jaroszynski
SUPA & University of Strathclyde, Glasgow, G4 0NG, UK

Jonathan Gratus & David Burton
Physics Department, Lancaster University, LA1 4YB, UK & The Cockcroft Institute, Daresbury, UK

Introduction

With the development of ultrahigh intensity laser facilities, such as the Extreme Light Infrastructure (ELI), it is increasingly important to understand how charged particles behave in strong electric and magnetic fields. While it is well known that such fields cause charges to accelerate, and hence to radiate energy and momentum, consistently accounting for accelerations caused by both the applied fields and the radiation field has troubled physicists for more than a century.

The Abraham-Lorentz-Dirac (ALD) equation, derived to describe the motion of a radiating point charge, is beset with difficulties. The worst of these is the existence of solutions which describe exponentially increasing proper acceleration − so-called runaway solutions − something at odds with both intuition and observation.

Because of these problems, many alternative descriptions of radiation reaction have been proposed. However, the many independent derivations of the ALD equation suggest it should remain the starting point of any serious study of radiation reaction.

Any realistic prospect of studying the effects of radiation reaction experimentally come from observing not individual particles, but rather electron bunches containing on the order of 10^8 particles or more. It follows that an appropriate description of radiation reaction is not the single particle ALD equation, but a kinetic theory based on it. We have recently presented such a theory, and, after a brief overview of the single-particle theory, summarize it here.

Single particle theory

The ALD equation for a particle of charge q and mass m in an external electromagnetic field F^a_b is

$$\dot{u}^a = -\frac{q}{m}F^a_b\, u^b + \tau\Delta^a{}_b\ddot{u}^b,$$

where $\tau \coloneqq q^2/6\pi m$ is the characteristic time of the particle, $\Delta^a{}_b \coloneqq \delta^a_b + u^a u_b$ is the projection orthogonal to the 4-velocity u^a, and an overdot denotes differentiation with respect to proper time s.

The difficulties in using this equation stem from the fact it involves the derivative of the particle's acceleration, so specifying initial position and velocity does not uniquely fix the solution. On the other hand, a generic specification of the initial acceleration leads to pathological behaviour, with the proper-acceleration growing exponentially, $\sqrt{\ddot{u}_a\ddot{u}^a}\sim e^{s/\tau}$.

To avoid these problems, Landau and Lifshitz have proposed an alternative equation of radiation reaction, obtained by expanding the ALD equation about the Lorentz force:

$$\dot{u}^a = -\frac{q}{m}F^a_b\, u^b - \frac{q}{m}\tau\left(\partial_d F^a_b u^b - \frac{q}{m}\Delta^a{}_b F^b{}_c F^c{}_d\right)u^d.$$

This equation has the advantage that when the applied force vanishes, so too does the acceleration, so runaway solutions are absent. However, while it may be a good approximation for a single radiating particle, it is far from clear how the errors scale with the number of particles, so it is not a suitable starting point for a kinetic theory.

Kinetic theory

For a sufficiently large collection of particles, we can use a particle distribution function to analyze the average properties, if we are not concerned with tracking the detailed motion of each particle.

The Maxwell-Vlasov theory is a self-consistent kinetic theory of charged particles, which conserves energy and momentum and so includes some of the bulk features of radiation reaction. However, it treats the charge as a continuum whose elements have infinitesimal charge and mass, and so must be altered to describe particles whose trajectories satisfy the ALD equation.

Since the ALD equation is 3rd order, the appropriate phase space must have acceleration variables as well as spacetime and velocity variables. Hence the Liouville vector governing the dynamics of the system is

$$L \coloneqq \frac{d}{ds} = u^a\frac{\partial}{\partial x^a} + a^a\frac{\partial}{\partial u^a} + \dot{a}^a\frac{\partial}{\partial a^a},$$

where a^a is the 4-acceleration, and $\dot{a}^a$ is given from the ALD equation as

$$\dot{a}^a = a_b a^b u^a + \frac{1}{\tau}\left(a^a + \frac{q}{m}F^a_b u^b\right).$$

Since particles with the same initial conditions evolve together, the number of particles in a region of phase space remains constant. It follows that the generalized Vlasov equation takes the form

$$Lf + \frac{3}{\tau}f = 0,$$

where the second term follows from the expansion of the phase space volume element under the flow of L.

This equation governs the motion of the particles. To close the system, we must couple it to Maxwell's equations, using the current

$$J^a = q\int u^a f\,\frac{d^3u\wedge d^3a}{(u^0)^2}.$$

Fluid model

The generalized Vlasov equation does not in general reduce to the usual Vlasov equation in the limit $\tau \to 0$. This is because any regular solution contains runaway trajectories as well as physical ones. Hence physical solutions must be singular, with support only on a submanifold of phase space.

Rather than work with singular quantities, we can take moments of the generalized Vlasov equation, yielding a fluid theory on spacetime. Because this procedure involves integrating out the velocity and acceleration dependence, the moments themselves are regular, unlike the distribution function.

Define the (l,n)-moments of the distribution,

$$S^{a_1\ldots a_l:b_1\ldots b_n} = \int u^{a_1}\ldots u^{a_l} a^{b_1}\ldots a^{b_n} f\,\Omega,$$

where $\Omega = (u^0)^{-2} d^3u \wedge d^3a$ is the invariant measure. Then integrating the generalized Vlasov equation yields

$$\begin{aligned}\partial_c S^{ca_1\ldots a_l:b_1\ldots b_n} &= lS^{(a_1\ldots a_{l-1}:a_l)b_1\ldots b_n} + nS^{a_1\ldots a_l(b_1:b_2\ldots b_n)c}{}_c \\ &+ \frac{n}{\tau}\Big[S^{a_1\ldots a_l:b_1\ldots b_n} \\ &+ \frac{q}{m} S^{a_1\ldots a_l c:(b_1\ldots b_{n-1}} F_c^{b_n)}\Big],\end{aligned}$$

where parentheses about indices denote symmetrization.

The first few equations read explicitly

$$\partial_a S^{a:\emptyset} = 0,$$

$$\partial_a S^{ab:\emptyset} = S^{\emptyset:b},$$

$$\partial_a S^{a:b} = S^{b:c}{}_c + \frac{1}{\tau}\Big[S^{\emptyset:b} + \frac{q}{m} S^{c:\emptyset} F^b{}_c\Big],$$

where the index $\emptyset$ denotes the absence of velocity and/or acceleration terms in the given moments.

It is convenient, and helps to illustrate the relation between the field system and the original ALD equation, to rewrite the moment equations in terms of the average velocity and acceleration,

$$U^a = \frac{S^{a:\emptyset}}{S^\emptyset}, \qquad A^a = \frac{S^{\emptyset:a}}{S^\emptyset},$$

and the centred moments

$$R^{a_1\ldots a_l:c_1\ldots c_n} = \int \bar{u}^{a_1}\ldots\bar{u}^{a_l}\bar{a}^{b_1}\ldots\bar{a}^{b_n} f\,\Omega,$$

where $\bar{u}^a = u^a - U^a$ and $\bar{a}^a = a^a - A^a$. Then the above become

$$U^a\partial_a S^\emptyset = -S^\emptyset \partial_a U^a,$$

$$U^a\partial_a U^b = A^b - \frac{1}{S^\emptyset}\partial_a R^{ab:\emptyset},$$

$$\begin{aligned}U^a\partial_a A^b = A_c A^c U^b &+ \frac{1}{\tau}\Big(A^b + \frac{q}{m} F^b_c U^c\Big) \\ &+ \frac{1}{S^\emptyset}\big[R^{b:c}{}_c + 2R^{b:}{}_c A^c + R^{\emptyset:c}{}_c U^b - \partial_a R^{a:b}\big].\end{aligned}$$

If the centred moments all vanish, these represent the ALD equation as a field system, with proper time derivatives replaced by $U^a\partial_a$. In general, the centred moments represent collective effects which drive the average motion away from the motion of an individual particle.

As with the single particle ALD equation, this field system contains both physical and unphysical solutions, with the latter manifesting as instabilities. By analogy with the Landau-Lifshitz approximation, we can eliminate the unphysical solutions by expanding the equations about $\tau = 0$. Because of the acceleration moments, this will not in general lead to the same fluid system as we would get from a kinetic theory based on the Landau-Lifshitz equation.

Reducing a kinetic theory to a fluid system based on a finite number of modes introduces a loss of information, which manifests itself in the failure of the moment equations to form a closed system. It is therefore necessary to introduce equations of state to supplement the system. Because of the greater variety of moments available, the appropriate choice of equation of state is more subtle than for the fluid system based on the usual Vlasov theory, and further exploration of this issue is required. One convenient and physically relevant choice corresponds to a cold fluid model, and involves setting all centred moments to zero.

Langmuir waves

One of the most fundamental phenomena in the physics of plasmas is the existence of Langmuir waves, and these provide an important testing ground for any theory. Although the effects of radiative damping on such waves will be extremely small, it provides a useful demonstration of how the theory can be applied. For simplicity, we consider only the case of a cold plasma.

The equilibrium state for a cold quiescent plasma is

$$S^\emptyset = n_0, \quad U^a = \delta^a_0, \quad A^a = 0, \quad F_{ab} = 0,$$

with external current due to the ions, $J^a_{ext} = -qn_0\delta^a_0$.

Linearizing the field system and Maxwell's equations about this equilibrium, and seeking harmonic longitudinal solutions of frequency ω leads to the dispersion relation

$$\omega^2(1 + i\omega\tau) = \omega_p^2,$$

where $\omega_p = \sqrt{q^2 n_0/m}$ is the plasma frequency. This has three roots: two (physically equivalent) physical solutions,

$$\omega \approx \pm\omega_p\left(1 - \frac{5}{8}\left(\omega_p\tau\right)^2\right) - \frac{i}{2}\omega_p^2\tau,$$

and the unphysical solution,

$$\omega \approx \frac{i}{\tau}.$$

The physical roots behave as one would expect: oscillations close to the plasma frequency, with a small radiative damping term. The third root describes an extremely rapid growth without oscillation. Its origin in the runaway solutions of the ALD equation is seen in the impossibility of taking the limit $\tau \to 0$, so it must be rejected as unphysical.

Conclusions

We have discussed a kinetic theory suitable for describing large numbers of radiating electrons, based on the exact Abraham-Lorentz-Dirac equation. Like the ALD equation, it admits both physical solutions and unphysical ones for which the limit $\tau \to 0$ does not exist.

While the presence of the nonphysical solutions prevents the kinetic theory from reducing to the usual Maxwell-Vlasov description in the appropriate limit, a fluid model can be derived from the moments of the particle distribution function which does have the correct correspondence limit.

As a simple demonstration of the theory, we have applied it to the radiative damping of Langmuir waves, and found that, as expected, it exhibits both physically reasonable behaviour and unphysical solutions which must be rejected.

Acknowledgements

We acknowledge the support of the U. K. EPSRC, the Laserlab-Europe consortium and the FP7 - Extreme Light Infrastructure (ELI) project.

References

1. P.A.M. Dirac, Proc. R. Soc. A **167** 148 (1938)
2. L.D. Landau and E.M. Lifshitz, *The Classical Theory of Fields* (Pergamon, London, 1962)
3. A. Noble *et al*., Proc. SPIE 8079, 80790L (2011)
4. A. Noble *et al*., *A kinetic model of radiating electrons*, in preparation.

Simulating Prolific Pair-Production in 10PW Laser-Plasma Interactions

Contact ***c.ridgers1@physics.ox.ac.uk***

C. P. Ridgers
University of Oxford
Clarendon Laboratory, Parks Road, Oxford, OX1 3PU

A. R. Bell
University of Oxford & Rutherford Appleton Laboratory
Clarendon Laboratory, Parks Road, Oxford, OX1 3PU

J. G. Kirk
Max Planck-Institute fur Kernphysik
Postfach 10 39 80, 69029 Heidelberg, Germany

R. Duclous
Commissariat a l'Energie Atomique, Bruyeres-le-Chatel, DAM-Ile de France, France

Introduction

With the next generation of high intensity lasers it will be possible to access the regime in which Quantum Electrodynamics (QED) plays an important role. Specifically, the laser-fields may be sufficiently strong to generate electron-positron pairs [1,2]. In order to correctly simulate laser-plasma interactions with 10PW lasers one must include pair production in the modeling tools, first and foremost in Particle-in-Cell (PIC) codes. Here we will discuss the model required to do this efficiently.

At laser intensities between 10^{23}Wcm^{-2} and 10^{24}Wcm^{-2} two effects become increasingly important. Firstly the acceleration of the electrons in the laser fields is sufficiently violent that they may generate high-energy gamma-ray photons, the generation of which causes the electron to recoil significantly. This radiation drag is important in determining the motion of the electrons. The high energy photons may then go on to generate pairs in the fields of the laser, a process known as the (multiphoton) Breit-Wheeler process. Alternatively the electrons may generate pairs directly in the laser-fields, via a virtual photon. This is known as the Trident process. Of particular interest is the fact that the two-step Breit-Wheeler process can lead to all of the laser energy being converted to pairs, and so very efficient antimatter production [1,3]. At 10PW laser intensities the emission of gamma rays by the electrons is discontinuous, i.e. few high-energy photons are emitted instead of continuous radiation. This enhances the rate of pair production as the electron can reach high energy between emission events and so emit a high energy photon which is in turn more likely to create a pair, this process is known as straggling [4].

The theoretical model

A semi-classical model describing the QED effects described above was developed by Bell, Kirk, Arka & Duclous [1,2,4], a summary of this model is presented here.

The controlling parameter determining the rate of emission of photons by electrons accelerated in the laser fields is

$$\eta = \gamma \left| \frac{\mathbf{E}_\perp}{\mathbf{E}_s} + \mathbf{v} \times \frac{\mathbf{B}}{\mathbf{B}_s} \right| \qquad (1)$$

Here $\mathbf{E}_\perp$ is the electric field perpendicular to the direction of motion of the electron $\mathbf{E}_s$ (= c$\mathbf{B}_s$ =1.3x10^{18}Vm^{-1}) is the Schwinger field (the field at which the vacuum breaks down into a cascade of pairs). Pair production becomes important when η becomes of the order of 0.1 [1]. For an intensity of 10^{23}Wcm^{-2} the electric field of the laser is of the order of 10^{15}Vm^{-1}. From equation (1) one can see that when the Lorentz factor of the electrons (γ) is of the order of 100 then pairs should be produced in significant quantities. Electrons are accelerated to this energy by a 10PW laser.

The second controlling parameter is

$$\chi = \frac{h\nu}{2m_e c^2} \left| \frac{\mathbf{E}_\perp}{\mathbf{E}_s} + \frac{\mathbf{k}}{k} \times \frac{\mathbf{B}}{\mathbf{B}_s} \right| \qquad (2)$$

Here $h\nu$ is the relevant photon energy and $\mathbf{k}$ is its wavevector.

The rate of generation of gamma-ray photons by an electron and their energy are controlled by these parameters. The rate of generation of photons of all energies by a single electron of Lorentz factor γ is

$$\frac{dN_\gamma}{dt} = \sqrt{3} \frac{m_e c^2 \alpha_f}{h} \frac{\eta}{\gamma} \int_0^{\eta/2} \frac{F(\eta,\chi)}{\chi} d\chi \qquad (3)$$

Where η and γ are those for the emitting electron. $F(\eta,\chi)$ is the (quantum-corrected) synchrotron function [2]. As the energy of the electron increases, the energy spectrum (i.e. the synchrotron function) shifts to higher energies, and so higher energy photons are emitted; these are much more likely to generate pairs.

The rate of pair production from photons with energy $h\nu$ and controlling parameter χ by the Breit-Wheeler process is given by

$$\frac{dN_\pm}{dt} = \frac{\alpha_f m_e c^2}{h} \frac{m_e c^2}{h\nu} \chi T(\chi) \qquad (4)$$

The corresponding rate of pair production directly by an electron (the Trident process) with Lorentz factor γ and controlling parameter η is

$$\frac{dN_\pm}{dt} = 0.64 \frac{\alpha_f^2 m_e c^2}{h} \frac{\eta}{\gamma} \Omega(\eta) \qquad (5)$$

$\Omega(\eta)$ and $T(\chi)$ are well known functions [2,5].

The inclusion of pair production in PIC codes

The emission of gamma-ray photons and pairs described above is a statistical process. A quantum particle may or may not emit in a given time interval subject to emission probabilities. This statistical nature of the emission process gives rise to the straggling effect already mentioned [4]. In order to capture this effect a Monte-Carlo approach is taken when including pair-production in a PIC code [4]. If a beam of particles of initial intensity I_0 travels through a medium of optical depth τ then the emerging intensity is

$$I = I_0 e^{-\tau} \Rightarrow P = (1 - e^{-\tau}) \qquad (6)$$

P is probability of a given beam particle emitting. From equation (6) we see that most particles penetrate to some small optical depth, with relatively fewer getting further. Such a description of the emission process is naturally suited to inclusion in a PIC code. Each particle is assigned with a *P*-value at random, this is used to compute the optical depth it reaches before emission. As the particle moves along its worldline by distance Δs, $\Delta\tau$ is added to its optical depth until it reaches its optical depth for emission, at which point it emits a particle. The increments to the optical depth are

$$\Delta\tau = \Delta t \frac{dN}{dt} \qquad (7)$$

dN/dt is the relevant rate of particle production, for the generation of photons by an electron or positron this is given by equation (3) and for the generation of a pair from a photon by equation (4). Note that it has been shown that the generation of pairs by the Trident process is not important for high intensity ($>3\text{x}10^{23}\text{Wcm}^{-2}$) interactions and it will no longer be considered [4].

We will now consider each step in the two-step Breit-Wheeler process. Firstly a photon is generated. This occurs when the optical depth of an electron or positron equals that for emission as calculated using the Monte-Carlo approach described above. The photon is emitted moving in the same direction as the electron or positron, its energy is determined by a quantum, and therefore, Monte-Carlo process. The probability that the emitted photon has a given energy is set by the synchrotron function. The energy of the photon is related to the χ-value with which it is emitted. The probability of the photon having a χ-value between 0 and χ_f is

$$P = \frac{\int_0^{\chi_f} \frac{d^2N_\gamma}{d\chi dt} d\chi}{\int_0^{\eta/2} \frac{d^2N_\gamma}{d\chi dt} d\chi} = \frac{\int_0^{\chi_f} \frac{F(\eta,\chi)}{\chi} d\chi}{\int_0^{\eta/2} \frac{F(\eta,\chi)}{\chi} d\chi} \qquad (8)$$

Once again *P* is chosen at random and by inverting equation (8) χ_f is found. This then gives the energy of the emitted photon

$$h\nu = \frac{2m_e c^2 \chi_f \gamma}{\eta} \qquad (9)$$

η and γ are those for the emitting particle.

The electron (or positron) recoils, resulting in its momentum changing from $\mathbf{p}_f$ to $\mathbf{p}_i$

$$\mathbf{p}_f = \mathbf{p}_i - \frac{h}{2\pi}\mathbf{k} \qquad (10)$$

k is the wavevector of the emitted photon. This formulation does not conserve energy but the error has been shown to be of the order of $1/\gamma_i\gamma_f$ (the subscripts *i* and *f* denote the initial and final states of the electron respectively) [4]. The error is small as the electron is ultra-relativistic in 10PW laser-plasma interactions.

The photon generated is then assigned an optical depth for emission and propagates until this is reached, at which point it emits a pair and is annihilated. The electron and positron are emitted moving in the same direction as the photon. The electron is assigned a fraction of the photon's energy *f*. The probability of the electron gaining this fraction is given by

$$P = \frac{\int_0^f \frac{dR(f,\chi)}{df} df}{\int_0^1 \frac{dR(f,\chi)}{df} df} \qquad (11)$$

dR(f,χ)/df is given by [6]

$$\frac{dR(f,\chi)}{df} \propto \frac{2 + f(1-f)}{f(1-f)} K_{2/3}\left(\frac{1}{3\chi f(1-f)}\right) \qquad (12)$$

Where χ is that for the emitting photon and $K_{2/3}$ is a Bessel function of the second kind. The constant in equation (12) is not required as *P* is expressed as a ratio.

The electron is assigned a *P*-value at random and equation (11) is inverted to determine *f*. It should be noted that the value of *f* is relatively unimportant as the energy the electron and positron in the pair gain by acceleration in the laser field is typically much greater than that they start with.

Conclusions

A relatively straightforward prescription for including radiation and pair-production in a PIC code has been developed and presented here in summary. Including these QED effects is of crucial importance to modeling the interaction of 10PW laser-plasma interactions, where such processes are of importance.

References

[1] A.R.Bell & J.G.Kirk, Phys Rev Lett, **101**, 200403 (2008)

[2] J.G.Kirk, A.R.Bell & I.Arka, Plas Phys Cont Fus, **51**, 085008 (2009)

[3] N.Elkina *et al*, Phys.Rev.ST Accel.Beams, **14**, 054401 (2011)

[4] R.Duclous, Plas Phys Cont Fus, **53**, 015009 (2010)

[5] T.Erber, Rev Mod Phys, **38**, 629 (1966)

[6] J.K.Daugherty & A.K.Harding, Ap J, **273**, 761 (1983)

The Magnetic Switchyard : Guiding Fast Electrons for Fast Ignition ICF

Contact *alex.robinson@stfc.ac.uk*

A.P.L.Robinson

Central Laser Facility
STFC Rutherford-Appleton Laboratory
Didcot,
OX11 0QX,
United Kingdom

M.Tabak and M.H.Key

Lawrence Livermore National Laboratory
Livermore
USA

Introduction

Fast Ignition ICF [1] is an attractive alternative to central hot-spot ignition of inertially confined fusion fuel. The key attractions are the significant reductions in implosion requirements and the overall reduction in laser energy that should be required (a few hundred kJ as opposed to > 1MJ).

The reduction in overall laser energy will only be achieved if there is a sufficiently high coupling efficiency between the short "ignitor" laser pulse and the hot spot that is generated in the compressed DT fuel. Extensive hydrodynamic studies, based on analytic considerations, have indicated that the minimum energy that must be coupled into the hot spot for ignition are in the range 10-20kJ (assuming DT compressed to 350-400 gcm^{-3}) in 10-20ps. Achieving a laser to fast electron conversion efficiency of 30%, and perhaps higher, is not unlikely. This therefore leaves the question of how to ensure that a sufficiently large proportion of the fast electron energy is deposited in the hot spot. If the fast electron population has a large divergence angle (PIC simulations increasingly suggest this is the case) this will not be possible, but if one could devise a scheme for effectively guiding the fast electrons then this could become possible.

In this report we describe a new concept for guiding fast electrons using structured inserts in the cone tip. The concept has been assessed using 3D numerical simulations for multi-kJ conditions that are relevant to full Fast Ignition.

Magnetic Switchyard Concept

We propose a new concept for effectively guiding the fast electrons in the case where the fast electrons have a high divergence angle. This is termed the "Magnetic Switchyard", and this is based on the idea of engineering the growth of resistivity gradients that the authors proposed in [2], and which were explored experimentally in [3,4]. The idea is to use an insert in cone and to focus the laser onto the rear surface of the insert. The insert consists of an array of concentric quasi-cylindrical shells embedded in a lower-Z substrate. The shells are axisymmetric about the cone axis. This arrangement is illustrated in figure 1 below.

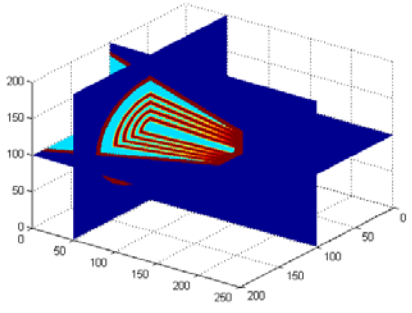

Figure 1 : Slice Plot of Z for a Magnetic Switchyard insert into a cone. Red regions are higher Z than blue regions. This shows the concentric, axisymmetric shells embedded in the lower-Z material.

The Magnetic Switchyard works as follows : As fast electrons flow through the structure, initially as a divergent spray, magnetic fields will grow at the interfaces between higher-Z and lower-Z materials. These fields will act to push fast electrons into the higher-Z guiding shells. Eventually the magnetic fields will have grown to such an extent that they will function as `rigid pipes' for the fast electrons. The shells will only accept a part of the fast electron source with a limited angular spread. As the bunches move through the shell they will have their mean direction altered (from diverging to converging), but the angular spread of the bunch cannot be reduced. At the far end of the switchyard we should thus emit electron bunches whose mean direction have all been altered so as to point at a distant target region. In a fast ignition scenario there is now no need to introduce any guiding elements outside the cone, which pose problems for hydrodynamic fuel assembly. In figure 2 below, we show the results of a 2D particle tracking simulation through a prescribed B-field arrangement similar to what one might obtain. This shows how such an arrangement might act to guide electrons.

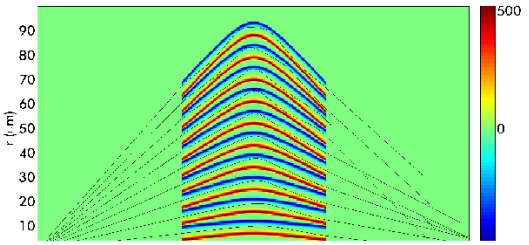

Figure 2. Results of 2D particle tracking calculation through a prescribed B-field. This illustrates how the Switchyad might work to guide fast electrons to a distant point, even when they are initially divergent.

3D Hybrid Simulation Model

In what follows we will now show the results of one of a number of numerical simulations that show that the magnetic switchyard concept may be highly beneficial to Fast Ignition ICF, even if the switchyard is not too complex.

The numerical simulations are 3D particle-based hybrid code calculations, that have been performed using the ZEPHYROS code [3,4]. ZEPHYROS is a particle hybrid code, and a description of this method can be found in the work of Davies and co-workers [5]. The simulations were performed on a 200x200x200 grid with a cell size of 1μm on each side. In these simulations an array of carbon shells (density $2gcm^{-3}$)

embedded in CH_2 (density of 1gcm^{-3}) was studied. The atomic Z-map and ion density are shown in figure 3 below as a slice through the x-y mid-plane. The background temperature is initially set to 100eV. Note that we also include compressed DT fuel in the simulation, however no hydrodynamics or burn is included in the simulation model.

The fast electron injection models irradiation by a laser intensity of 4 x 10^{20}Wcm^{-2} with a 50% conversion efficiency. The temporal profile of the beam is a top-hat function of 18ps duration, and the transverse injection profile that was employed is $\exp(-(r/r_s)^4)$ with r_s = 15μm . The fast electron distribution was given by a single-temperature relativistic Maxwellian in energy, with T_f = 2.6MeV (from the ponderomotive scaling with a 0.351μm wavelength) and in terms of angular distribution a uniform distribution over a cone subtended by a half-angle of 70^o was used. The total fast electron energy that is injected is 23kJ. These simulations are run up to 20ps.

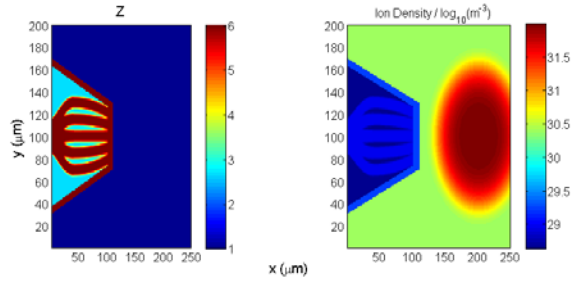

Figure 3 : Ion Charge (Z) in x-y midplane (left), and Ion Density in x-y midplane (right).

Results

In the simulation it was found that the Magnetic Switchyard structure had a strong guiding effect on the fast electrons as we anticipated. In figure 4 we show the fast electron density and the B_z component of the magnetic flux density in the x-y midplane at 6ps.

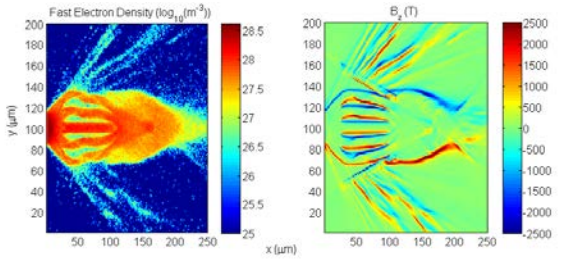

Figure 4 : Fast Electron Density in x-y midplane at 6ps (left), and B_z component of magnetic flux density in x-y midplane at 6ps (right).

The fast electron density in figure 4 shows that strong guiding of the fast electrons has occurred, both through the switchyard structure and through the DT fuel. The structure of the fast electron density is interesting. There exists a distinct cone that suggests convergence of fast electrons, surrounded by a 'penumbra' of lower fast electron density, which suggests that it consists of divergent fast electrons.

The plot of B_z in figure 4 shows that collimating/confining B-field builds up around all of the more resistive shells inside the Switchyard as expected, thus achieving the anticipated effect. In the DT fuel region we note that a strong collimating field is generated but only around the aforementioned 'penumbral' part of the fast electron beam. The denser, converging part of the beam only seems to have much weaker magnetic field associated with it.

The observations of the fast electron density pattern and magnetic field apply to most of the simulation time. At the end of the simulation, one is clearly more interested in examining the coupling of the fast electron energy into the dense DT fuel.

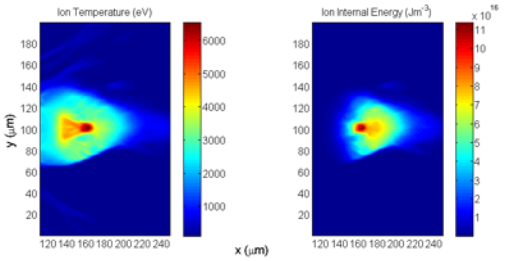

Figure 5 : Ion temperature in x-y midplane at 20ps (left), and Ion Internal Energy in x-y midplane at 20ps (right). Note that both plots only show the DT fuel region.

In figure 5 we show plots of the ion temperature and ion internal energy at 20ps in the DT fuel region only (i.e. > 110 μm). In terms of the energetic of this simulation, it is important to remember that 23kJ of fast electron energy is injected. The ion temperature shows that a very small spot is heated to 6keV (at this point the density is about 275gcm^{-3}) and this is surrounded by a wider region which is heated to about 3keV. In terms of the ion internal energy one can see that a roughly spherical hot spot has been generated with a roughly 20μm radius. If one integrates the internal energy over a 40x40x40μm cube centred on (172,100,100)μm then one finds that 6.22kJ has been deposited. This means that the effective coupling efficiency is 27%. The Atzeni minimum ignition criterion [6] for a spot of this size would be about 22kJ so this is insufficient to ignite the target. Nonetheless it does show that the Switchyard can lead to good coupling efficiencies even when the electron divergence is large (70^o half-angle in this case) under multi-kJ Fast Ignition relevant conditions.

Conclusions

In this article we have reported on the development of a new concept for guiding fast electrons which are initially highly divergent for Fast Ignition ICF. The concept is based on previous work which showed that resistivity gradients can be used to engineer the growth of collimating magnetic field as required. 3D hybrid simulations suggest that even when the electron divergence half-angle is 70^o, that the use of the switchyard results in 27% coupling into a 20μm radius hot-spot. Future work will concentrate on scaling the concept to full ignition conditions.

Acknowledgements

APLR is grateful for the use of computing resources provided by Science and Technology Facilities Council's e-Science facility.

APLR would like to thank A.R.Bell, W.Bokee-West, M.Tolley, and P.A.Norreys for their advice and useful discussions during the course of this work.

References

1. M.Tabak et al., *Phys.Plasmas*, **1** (1994)
2. A.P.L.Robinson and M.Sherlock, *Phys.Plasmas*, **14**, 083105 (2007)
3. S.Kar et al., *Phys.Rev.Lett.*, **102**, 055001 (2009)
4. B.Ramakrishna et al., *Phys.Rev.Lett.*, **105**, 135001(2010)
5. J.R.Davies et al, *Phys.Rev.E*, **56** (1997)
6. S.Atzeni, *Phys.Plasmas*, **6** , 3316 (1999)

Production of high energy protons with hole-boring radiation pressure acceleration

Contact *A.P.L.Robinson@stfc.ac.uk*

A.P.L.Robinson

Central Laser Facility,
STFC Rutherford-Appleton Laboratory
Didcot,
Oxfordshire,
United Kingdom
OX11 0QX

Introduction

Recently there has been considerable interest in Radiation Pressure Acceleration (RPA) of ions. RPA can occur in two distinct modes that have been termed 'Light Sail' (LS) [1] and 'Hole-Boring' (HB) [2] RPA respectively. In LS RPA a slab of plasma will be accelerated as a whole, and it has been shown that numerical simulations of this are well modeled by the classic simple model of a planar reflecting slab being accelerated by pure light pressure – hence the name. In HB RPA a laser pulse will drive into a thick slab of plasma pushing a beam of ions ahead of the receding plasma surface. Studies suggest that it should be much easier to reach high energies (> 100MeV per nucleon) with LS RPA than HB RPA.

In non-relativistic HB RPA the ion energy should be given by ,

$$\varepsilon = \frac{I}{n_i c}, \qquad (1)$$

and if we now assume that the minimum ion density is $a_0 n_c$, then we can express the intensity in terms of a_0 and substitute to obtain,

$$\varepsilon = a_0 m_e c^2 , \quad (2)$$

which is a very slow scaling compared to LS RPA. This scaling is not consistent with previous numerical simulations which show a much better scaling [2]. In this article we will examine why Eq. 2 is incorrect, and thus show that HB-RPA is much less restricted than the $a_0 n_c$ 'limit' suggests. This opens up the possibility that HB RPA will actually allow us to produce 100-200MeV protons at not excessively high intensities.

Theory

The $a_0 n_c$ 'limit' on HB-RPA comes from the minimum density at which a plasma will be transparent to an incident laser pulse. Linearized relativistic fluid theory gives this as $a_0 n_c$ for the case of a circularly polarized laser pulse. The problem with this is that linear theory does not fully treat such high intensity laser-plasma interactions. The effect of non-linearity on the penetration of laser pulses into plasma slabs was thoroughly analysed by Cattani et al. [3] using analytic theory. This yields the following expression for the penetration threshold at a given a_0,

$$a_p^2 = \frac{1}{4}\left[2n(1+a_d^2)(\sqrt{1+a_d^2}-1) - a_d^4\right], \quad (3)$$

where,

$$a_d^2 = n\left(\frac{9}{8}n - 1 + \frac{3}{2}\sqrt{\frac{9}{16}n^2 - n + 1}\right), \qquad (4)$$

Note that the electron density is normalized to the critical density in Eq.3 and 4. If this is shown graphically, as is done in figure 1, then we find that the penetration threshold rapidly exceeds that predicted by linear theory. In other words, Cattani's analysis indicates that we should be able to achieve HB-RPA with much lower density plasmas than that predicted by linear theory.

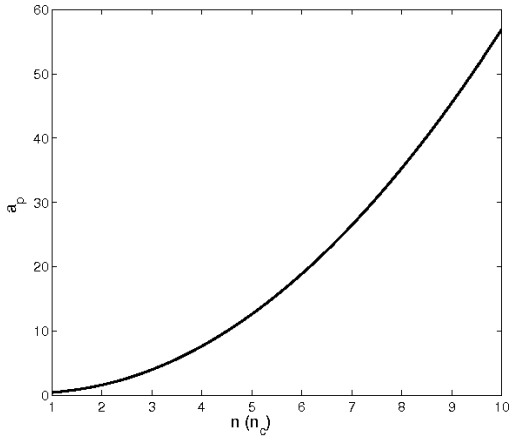

Figure 1 : Penetration threshold in terms of a_0 as predicted by Eq. 3 and 4.

Futhermore we can use the expressions developed in [2] to predict the proton energies that can be achieved given this limit. If one assumes that the laser wavelength is 1μm and that HB-RPA can be achieved right at the penetration threshold then one obtains the curves plotted in figure 2 below where both the maximum obtainable energy and the intensity requirement are plotted.

This shows that protons in the range of 100-200MeV can be generated using laser intensities in the range of $5\text{x}10^{21}$-$1\text{x}10^{22}$ Wcm^{-2}. In [2] the PIC simulations suggested that one would need 2-$4\text{x}10^{22}$ Wcm^{-2} to reach the 100-200MeV so this result represents a reduction by a factor of four in the required intensity. In what follows we will report on our numerical investigations that were carried out to validate this theoretical result.

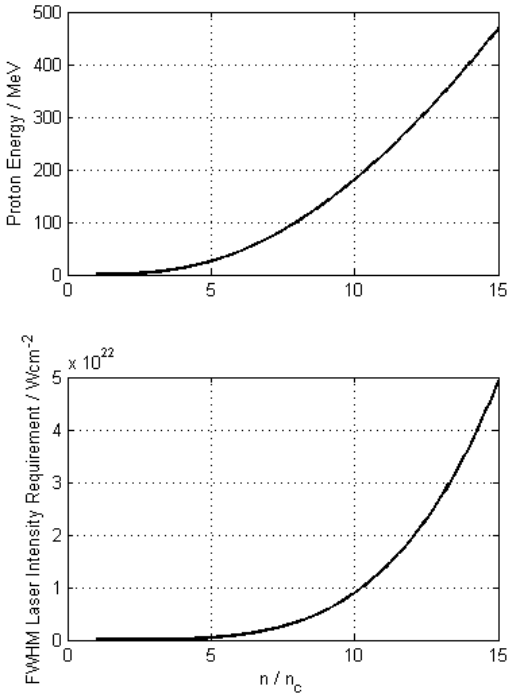

Figure 2 : Maximum achievable proton energy from HB-RPA as a function of plasma density normalized to critical density at 1µm wavelength.

Numerical Simulation Set-Up

One dimensional electromagnetic Particle-in-Cell simulations were carried out to address the questions raised in the preceding section. The code employed for this is the same used in previous investigations (e.g. [1]).The plasma consists of a purely hydrogenic plasma initially at a temperature of 20keV with a density in the range 3-10x$10^{27}$$m^{-3}$. The plasma has a `top-hat' density profile and is 10µm thick. Each species is represented by 100 macroparticles per cell. The spatial grid consisted of 10000 cells of 10nm width. A circularly polarized pulse with a FWHM intensity of I_{FWHM} = 1.25 x $10^{21}$$Wcm^{-2}$ and FWHM duration of 40fs is incident on the target from the left. The pulse has a $\sin^2$ temporal profile and a wavelength of 1µm.

Results

Initially a scan was conducted over the range of densities from 3-10x$10^{27}$$m^{-3}$ and the results are summarized in figure 3 in which we show the average energy of the protons accelerated by HB RPA at 75fs (if any), and the predicted energy according to the formulae of [2] for both the FWHM intensity and the peak intensity. As can be seen, we are obtaining HB RPA at plasma densities well below a_0n_c as predicted. To demonstrate that HB RPA is indeed observed we show the results of one particular simulation (the one where n = 7x$10^{27}$$m^{-3}$) in figure 4. This clearly shows the hole-boring process in the both the phase space, and the strong pistoning of the plasma in terms of the particle densities. Note that the actual target thickness is not important provided that it is more than a few microns thick. The target could be much thicker than the 10µm used here and the same results would be obtained.

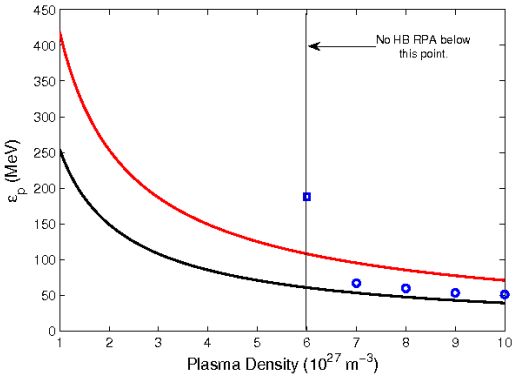

Figure 3 : Results of 1D PIC simulation as average proton versus plasma density (blue circles). Black line is predicted proton energy from HB formulae at FWHM intensity and red line is the same at the peak intensity.

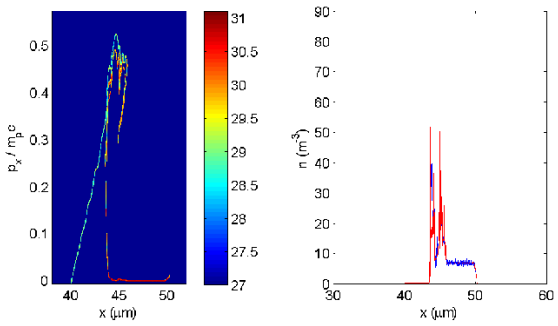

Figure 4 : (Left) p_x-x phase space for protons. (Right) Number densities of protons (red) and electrons (blue). Data is taken from the n = 7x$10^{27}$$m^{-3}$ simulation.

The loss of HB-RPA at 6x$10^{27}$$m^{-3}$ is consistent with Cattani's prediction for the penetration threshold. On extending this method of scanning across density at a given a_0 to a set of a_0s we have found a very good general agreement with Cattani's prediction.

Thus 1D PIC simulations validate the idea that one can reach much higher proton energies using HB-RPA than one would think from the a_0n_c limit.

This is the main text of the article. This will include many lines about what the article is about. There can be many sections depending what the subject matter is. These may contain graphs, figures, photos equations etc.

Conclusions

In this paper we addressed the question of the minimum plasma density that can be used to obtain HB-RPA. If this were limited to a_0n_c then reaching high proton energies is demanding. We showed, however, that the limit is considerably lower due to the effect of nonlinear processes on laser pulse penetration. In fact this reduces the intensities required to reach the 100-200MeV range by a factor of 4 – down to 0.5-1x$10^{22}$$Wcm^{-2}$, which means that high energy proton generation from HB-RPA should be possible. In future we will conduct multi-dimensional simulations to further investigate this route.

References

1. T.Esirkepov, *Phys.Rev.Lett.*, **92**, 175003-1 (2004)
2. A.P.L.Robinson, *Plasma Phys.Control. Fusion*, **51**, 024004 (2009)
3. F.Cattani et al., *Phys.Rev.E*, **62**, 1234 (2000)

The Effect of Density Scalelength on the Fast Electron Beam Generated by Ultra-Intense Laser-Solid Interactions

R.H.H. Scott,[1,2,a)] F. Perez,[3] J.J. Santos,[4] C.P. Ridgers,[5,2] J.R. Davies,[6] K.L. Lancaster,[1] S.D. Baton,[3] Ph. Nicolai,[4] R.M.G.M. Trines,[1] A.R. Bell,[5,1] S. Hulin,[4] M. Tzoufras,[5,1] S.J. Rose,[2] and P.A. Norreys[2,1]

[1)] *Central Laser Facility, STFC, Rutherford Appleton Laboratory, Harwell Oxford, Didcot, OX11 0QX, United Kingdom*

[2)] *Department of Physics, The Blackett Laboratory, Imperial College London, Prince Consort Road, London, SW7 2AZ, United Kingdom*

[3)] *LULI, École Polytechnique, UMR 7605, CNRS/CEA/UPMC, Route de Saclay, 91128 Palaiseau, France*

[4)] *Centre Lasers Intenses et Applications, UMR 5107, Université de Bordeaux 1 /CNRS/CEA, 351 Cours de la Liberation, 33405 Talence, France*

[5)] *Clarendon Laboratory, University of Oxford, Parks Road, Oxford OX1 3PU, United Kingdom*

[6)] *GoLP, Instituto de Plasmas e Fusão Nuclear - Laboratório Associado, Instituto Superior Técnico, 1049-001 Lisboa, Portugal*

(Dated: June 30, 2011)

A systematic experimental and computational investigation of the effects of density scalelength on ultra-intense laser-solid interactions has been performed. When the density scalelength is sufficiently large, the fast electron beam resulting from the laser-solid interaction is best described by two distinct populations: those accelerated within the sub-solid density plasma - the fast electron pre-beam, and those accelerated near or at the target front surface - the fast electron main-beam. The pre-beam has considerably lower divergence than that of the main-beam with a half-angle of $\sim 20°$, under the conditions investigated it contains up to 30% of the total fast electron energy absorbed into the target. The fast electrons comprising the pre-beam have a higher temperature than those of the main-beam. The number, kinetic energy, and total energy of the fast electrons in the pre-beam is increased by an increase in density scalelength.

A larger density scalelength reduces the total number of electrons absorbed into the target, but increases their mean kinetic energy, while the total absorbed energy is unchanged. With a larger density scalelength, the fast electrons heat a smaller cross sectional area of the target, causing the thinnest targets to reach significantly higher rear surface temperatures. This is ascribed to the enhanced fast electron pre-beam associated with the large density scalelength interaction, which generates a magnetic field within the target of sufficient magnitude to partially collimate the subsequent, more divergent, fast electron main-beam.

The study of MeV (fast) electron transport in high density plasmas is important for numerous applications including proton and ion beam production[1–3], isochoric heating of high density matter for opacity studies[4], and fast ignition inertial confinement fusion[5].

For successful fast ignition, laser energy must be efficiently coupled to fast electrons at the vacuum-solid boundary. Various mechanisms can cause ablation of the solid prior to the arrival of the ultra-high intensity laser pulse, thereby creating a density gradient at the vacuum-solid interface. Particle-In-Cell (PIC) modelling indicates[6] that a density gradient enhances laser absorption in comparison to a delta function type density profile. The aim of this experiment was to perform a systematic experimental investigation into the target rear surface heating using three well characterised front surface density ramps and three target designs.

[a)] Electronic mail: Robbie.Scott@stfc.ac.uk; The authors gratefully thank the staff of the LULI2000 laser facility, Ecole Polytechnique, Paris, France. This investigation was undertaken as part of the HiPER preparatory project and was funded by the UK Science and Technology Facilities Council.

This paper begins by outlining the experimental setup and results. It then describes PIC and Vlasov modelling of the experiment. Finally the experimental results are discussed and explained in light of the modelling.

A. Experimental Setup

The experiment was performed at the Ecole Polytechnique LULI pico2000 laser system which operates at 1053 nm, 40 J, 12 µm full-width-at-half-maximum (FWHM) and 800 fs pulse duration giving a peak intensity of 2×10^{19} W/cm^2. The laser was p-polarised with an incidence angle of 45° onto the CH surface of the CH(5 µm)-Al(10, 20 or 50 µm)-Cu(10 µm)-Al(1 µm) layered, planar, targets. The transverse target dimensions were 5 mm square.

The front surface density gradient was created using the laser's amplified spontaneous emission (ASE). The ASE arrives nanoseconds prior to the high intensity pulse ablating the target front surface, creating a front surface density gradient. The ASE was controlled by altering the timing of the Pockels cells, thereby changing the energy content and duration of the ASE and consequently the

front surface plasma density scalelength[7].

The plasma density gradient was inferred using a combination of gated transverse interferometry at 527 nm and 2D magneto-hydrodynamic modelling. Refraction of the $2\omega_0$ interferometry probe beam within the underdense plasma means interferometry can only provide a reference density profile below $\sim 10^{21}$ electrons/cm^3. The interferometry timing error was $\pm$ 200 ps. The density profile above 10^{21} electrons/cm^3 was inferred using the 2D magneto-hydrodynamic (MHD) code CHIC[8]. The modelling was fitted to the experimental data by setting the laser ASE duration and contrast parameters within CHIC to the measured experimental parameters, then iterating the input parameters until the MHD density profile fitted the interferometric data. This technique provides the complete target density profile.

DSL 'size'	ASE duration (ns)	Energy contrast	Density profile $(e-/cm^{-3})$
Small	1.1	3.0×10^{-3}	$1.530\times10^{25}(10-x(\mu m))^{-3.0}$
Medium	1.9	6.0×10^{-3}	$7.095\times10^{24}(14-x(\mu m))^{-2.7}$
Large	4.3	1.0×10^{-2}	$5.805\times10^{24}(20-x(\mu m))^{-2.4}$

Table I. The shot parameters for the three experimental density scalelengths and the functions fitted to the front surface density profiles. The functions fit the front surface density profiles along the propagation axis of the laser (45° off target normal), x is zero at the initial target front surface and decreases along the (outward) target normal axis. The functions were bounded at the target solid surface, switching to the solid density.

The target rear surface temperatures were evaluated using Cu K_α x-ray spectroscopy, and spatially and temporally resolved streaked pyrometry of the rear surface. A KAP conical crystal with a focal length of 310 mm and 2d spacing of 26.64 Å focussed the 6.85-8.5 keV (fifth order) Cu K_{α_1} and K_{α_2} x-rays onto an image plate[9]. Bulk electron temperatures within the Cu fluor layer were inferred by fitting Cu K_{α_1} and K_{α_2} line spectra generated by the non-LTE code FLYCHK[10] to the data. F/4 optics at 20° from target normal collected the visible optical emission from the target rear surface, which was split between a gated optical imager (GOI) and a high speed sampling camera (HISAC)[11]. The GOI provides a single frame image with high spatial resolution (∼10 µm) within the gate time of 80 ps, while HISAC combines a lower 2D spatial resolution (70 µm) with higher temporal resolution (∼ 50 ps) and multi-frame capability (2 ns window). HISAC was filtered using an ND 6, 950 nm lowpass filter and an ND 4, 20 nm FWHM bandpass filter centred at 532 nm, the temporal resolution is a function of the spectral bandwidth of the signal due to dispersion within the fibreoptics. Any optical transition radiation was removed from the spectral integral of the Plankian emission spectrum (the signal HISAC measures - subsequently referred to as the thermal signal) by extracting the thermal signal 100 ps after the interaction. Radiation-hydrodynamic modelling was used to infer the initial target temperature from the thermal emission at t=100 ps. During 100 ps, the target rear surface expands and cools, modifying the thermal emission spectrum. HYADES[12] was used to model the expansion and resultant evolution of this spectrum for many initial target temperatures. These spectra were folded with the spectral response of the streak camera optics, tube, and experimental spectral filtering, then integrated. This yielded a unique emission intensity for a given initial target temperature, allowing the measured intensity at t=100 ps to be directly related to the target temperature at t=0 ps. An absolutely calibrated lamp provided a reference intensity for both optical diagnostics.

The propagation of fast electrons (> 8 keV) within the target was inferred via 2D Cu K_α imaging from a 10 µm Cu fluor layer 1 µm beneath the target rear surface. The fast electrons heat the target via collisions and the return current[13], the thermal emission from the target rear is measured by HISAC. Finally the spatial distribution of the (incoherent) optical transition radiation[14–16] (the prompt emission detected by HISAC) was used to infer the spatial distribution of those electrons which escape the target.

B. Experimental Results

1. Density Scalelength & Target Thickness

The density scalelength (DSL) (L_n) is defined[7] as: $L_n = n\frac{dx}{dn}$, where n is the plasma density and $\frac{dx}{dn}$ the density gradient at n. Typically the density gradient is fitted by a function of the form $n_e = Cexp(-x/L_n)$ where C is a constant, however it was found the three experimentally inferred density gradients along the laser propagation axis were best fitted by a bounded power law function, and were not even approximately exponential in form. The fitted functions and inferred laser parameters are summarised in table I. For the purposes of brevity,

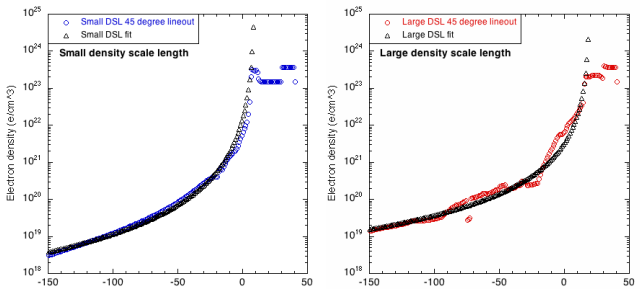

(a) (b)

Figure 1. Plots of target electron density lineouts along the laser axis and the fitted power law functions (see table I) used to describe the density profile in OSIRIS . (a) small DSL, (b) large DSL.

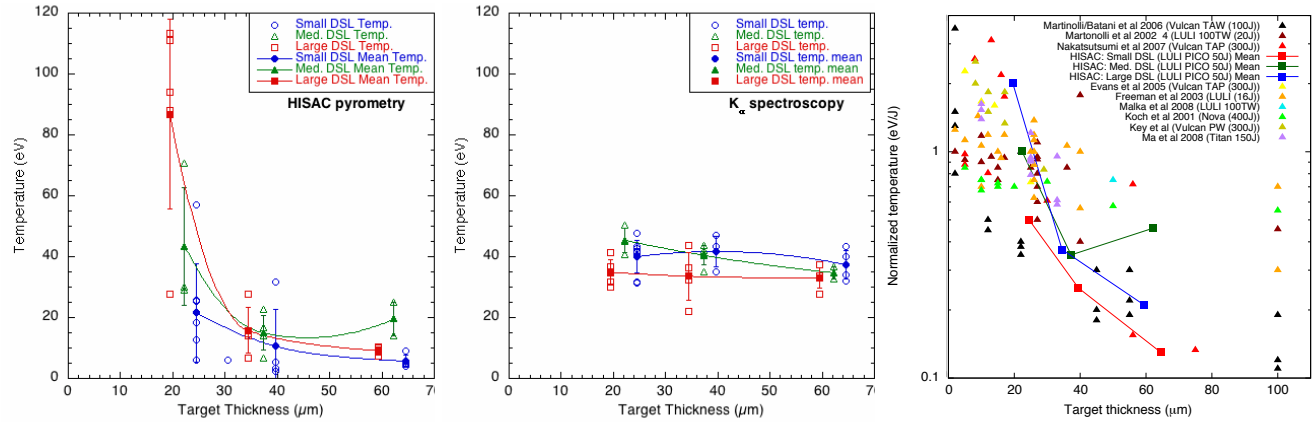

Figure 2. Rear surface temperatures as a function of target thickness for the three experimental density scalelengths: (a) HISAC pyrometry, (b) K_α spectroscopy. Actual data points are shown with hollow symbols, while the errors bars depict the standard deviation from the mean (shown by solid symbols).(c) Comparison of mean pyrometry data from this experiment against previously published experimental results. Note all data on plot (c) is normalised to laser energy on target.

the three experimental density profiles will subsequently be referred to as small, medium, and large density scalelengths, although at no point are scalelength values explicitly assigned to these terms for the above reasons.

The target thicknesses were calculated based on a combination of 2D CHIC radiation-hydrodynamic modelling and 2D3P OSIRIS PIC. The front surface ablation due to ASE was evaluated with CHIC, showing that the target thicknesses were altered for each density scalelength, meaning use of the initial target thickness was incorrect. Furthermore the offset of the critical density surface and the associated density ramp was also greatly affected by the ASE, so to simply use the solid density thickness post ablation would also be wrong. The PIC modelling showed that for each density scalelength, the laser refracted and hole-bored, propagating to a certain distance from the solid target front surface. The final effective target thickness was found by measuring the distance from the target rear to the position of closest approach as shown in figure 6. It should be noted that the initial target thicknesses used in the PIC modelling were the post ablation thicknesses from the radiation-hydrodynamic modelling.

2. Target Rear Surface Temperatures

The initial temperatures measured by pyrometry and spectroscopy are shown in figures 2 (a) and (b) respectively. The error bars depict the standard deviation of the results from the mean. Systematic errors in both measurements were approximately ± 5 eV. The pyrometry dataset indicates a clear increase in the rear surface target temperatures with increased density scalelength, and is most notable for the thinnest targets. The spectroscopically derived temperatures show no clear variation with target thickness or density scalelength.

It can be seen from figure 2 that there is broad quantitative agreement between the two sets of results, however the clear decrease in rear surface temperature with target thickness measured by HISAC, which is particularly evident with the larger density scalelengths is not in agreement with the Cu K_α spectroscopy. The increase in the K_α source size as the fast electrons diverged within the target had to be taken into account in order for accurate interpretation of the Cu K_α spectroscopy. If this was not accounted for, the loss of spectral resolution caused the K_{α_1} and K_{α_2} lines to merge creating a spectrum which was well fitted by a (FLYCHK generated) spectral line corresponding to an unphysically high temperature.

The apparent discrepancy between the spectroscopic and pyrometric (HISAC) results for the larger density scalelengths is attributed to a relative lack of sensitivity of the Cu K_α spectrometer. This is due to the combined effects of spatial and temporal integration, and poor signal-to-noise ratio. Furthermore the synthetic Cu K_α lines vary little over the (pyrometrically inferred) experimental temperature range, while the measured blackbody radiation increases by a factor of 25 over the same range. This lack of sensitivity has been shown on numerous experiments in this temperature regime, this diagnostic does however provide a useful order of magnitude temperature reference.

A comparison of the mean pyrometric experimental data with previous experimental laser-solid target heating data is shown in figure 2 (c). A best fit ($R^2 = 0.625$) to *all* of this data (not shown) was found to be $T(\mathrm{eV/J}) = 1.23e^{-0.018x}$, where x is the target thickness in μm. It should be noted that the vast majority of this data was from Aluminium targets. The rapid increase in rear surface temperature for thin targets with a large density scalelength measured via pyrometry is at the up-

per bound of previous measurements. Comparison of our data with the previous datasets suggests the large variation in the measured temperatures may be largely explained by variations in density scalelength.

3. Fast Electron Divergence

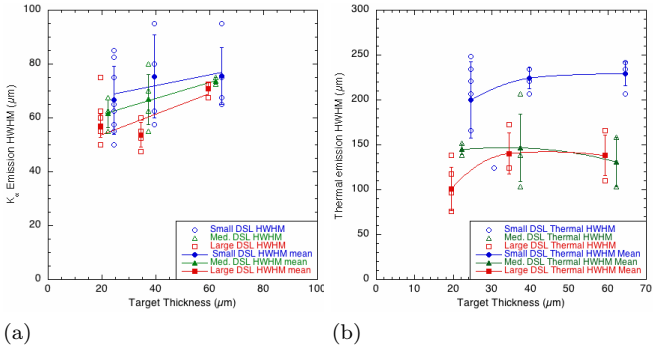

Figure 3. Emission spot size HWHM as a function of target thickness: (a) 2D Cu k$_\alpha$ imager, (b) HISAC thermal emission. The HWHM of both emission regions is reduced with increasing density scalelength, the reduction in the thermal dataset is greater.

The spatial extent of the K$_\alpha$ emission was measured with the 2D Cu K$_\alpha$ imager, as depicted in figure 3 (a) showing the half-width-at-half-maximum (HWHM) as a function of target thickness. This emission is primarily caused by fast electron collisions within the target, although effects such as photo-pumping may cause secondary K$_\alpha$ emission. The HWHM of the signal for various target thicknesses diverges with a 25±7° half angle for all density scalelengths.

The spatial HWHM of the thermal emission region on the target rear surface measured by HISAC is approximately halved for the larger density scalelengths. The mean K$_\alpha$ imager data shows the same trend but the magnitude of the reduction is less.

In both the K$_\alpha$ and pyrometry datasets, an extrapolation of the data to zero target thickness yields an apparent laser spot size *considerably* greater than that measured (∼ 12 µm FWHM). PIC modelling shows that this is due to refraction of the laser beam in the ablated plasma as it approaches the 45° p-polarised target, this causes the laser beam to bend along the target surface meaning absorption occurs over a far larger area than that of the vacuum focal spot. This is discussed in more detail in section C.

4. Integrated Emission

In order to measure the relative absorption of the three density scalelengths, the integrated emission was evaluated from the spatial integral of the HISAC thermal and

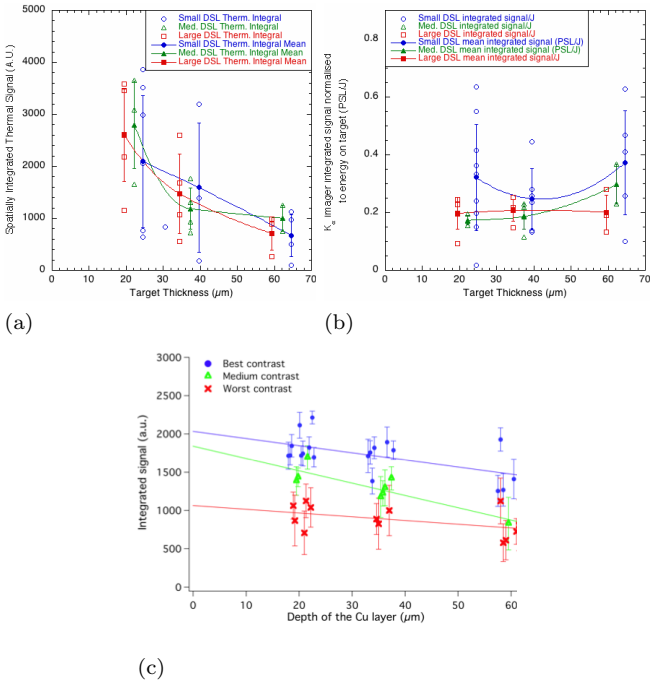

Figure 4. Integrated emission as a function of target thickness and density scalelength: (a) spatial integral of HISAC thermal signal showing no clear trends as a function of density scalelength, (b) the spatially integrated Cu k$_\alpha$ imager signal is enhanced by the small density scalelength, (c) spectrally integrated spectrometer signal, showing the small density scalelength signal is largest. Note to aid comparison, all data has been normalised to a shot energy of 50 J.

spatial integral of the Cu K$_\alpha$ 2D imager, as summarised in figure 4. No clear variation with DSL was visible in the spatially integrated thermal signal, while the spatially integrated Cu K$_\alpha$ imager, and spectrally integrated Cu K$_\alpha$ spectrometer showed an increased signal with smaller density scalelengths.

The OTR signal is measured from the streaked HISAC signal at $t = 0$. It was found that the spatially integrated OTR was clearly increased with the larger density scalelengths and thinner targets, as were the backgrounds of both x-ray diagnostics, as shown in figure 5.

C. Particle-In-Cell Modelling

2D3P PIC modelling was performed using OSIRIS[17] to evaluate the effect of changing the density scalelength. The 2D electron density profiles from the radhydro/interferometry, were fit along the axis of propagation of the laser as shown in figure 1. The fitted functions (see table I) described the front surface plasma density ramp to a distance of 150 µm from the target front solid surface, at the solid surface a step function switched to the solid target density. 45° p-polarisation was implemented by offsetting the density function.

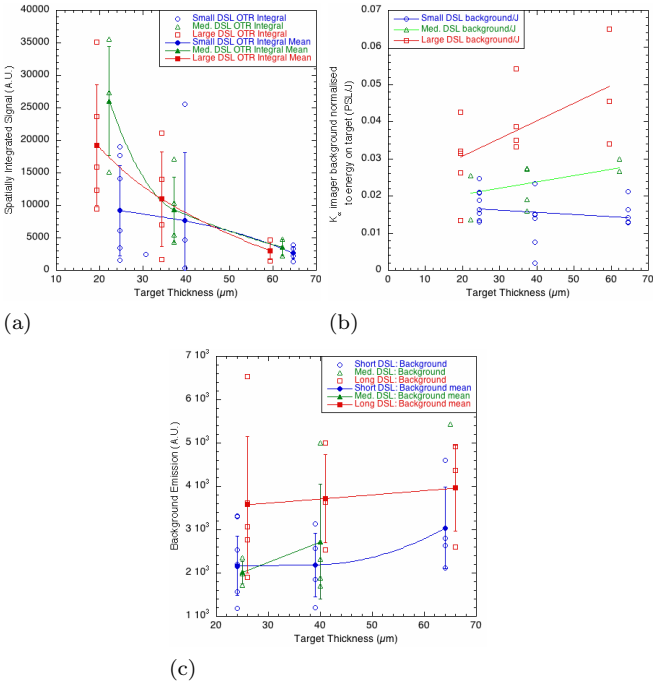

Figure 5. X-ray background as a function of target thickness and density scalelength: (a) Spatially integrated OTR, (b) Cu K_α imager background, (c) Cu K_α spectrometer background.

A grid of 26800 × 10000 cells (16 electrons and 1 ion per cell) were used over a real space of 270 × 100 µm. This resolved the plasma wavelength 19 times at the peak density of 40 times critical (n_c). The time-step satisfied the 2D Courant condition, resolving the peak plasma frequency 27 times per time-step. Each run lasted a real time of 1.5 ps and took 1150 cpu-days. Based on the measured numerical heating effects, all particles of energy less than 250 keV were removed prior to analysis.

The PIC modelling showed that in this density scalelength regime, the variation in density scalelength only caused relatively subtle differences to the dynamics of the laser pulse propagation. The large density scalelength causes enhanced relativistic self-focussing in comparison to the small DSL case, with the initial minimum occurring ∼ 20µm further from the target. In both cases the laser reaches a focal spot FWHM of ∼ 3 µm, after which it diverges slightly before finally refocussing to ∼ 2 µm nearer the critical surface. The laser ponderomotive force initially creates a straight, low density (∼ $0.02n_c$), channel within the underdense plasma. The formation of this channel is not affected significantly by the density scalelength.

The most notable feature of the laser propagation in both density scalelength cases is the refraction of the laser, this is due to the density gradient in combination with the 45° polarisation, as shown in figure 6. This refraction causes the effective focal spot to be greatly enlarged near the target front surface in comparison to the the vacuum focal spot-size. The p1x2 (momentum parallel to, and space transverse to the initial laser propagation axis respectively) phase space (not shown) shows that the refraction also greatly enlarges the transverse fast electron source size. This explains why the experimentally measured fast electron source is consistently so much larger than the laser's vacuum focal spot-size. Modelling of the large DSL run, but with normal incidence (not shown), showed this refraction was prevented, creating a considerably smaller fast electron source size.

The re-emitted laser beam can either reflect specularly or propagate along the target before being refracted away from the front surface by the underdense plasma. Modelling with shorter density scalelengths than those described here, showed that the pulse can hole-bore into the denser plasma creating a depression in the ion population of approximately the width of the focal spot, this tends to partially confine the lateral spread of the laser beam otherwise caused by refraction.

Figures 7 (a) and (b) show the p2p1 (momentum components transverse and parallel to the initial laser propagation axis respectively) phase space plots of the small and large density scalelengths respectively during the underdense interaction shortly before the pulses reach the target front surfaces. At this time, the fast electron population generated by the large density scalelength interaction has a significantly enhanced p1 component. In order to further characterise the fast electron beam, a quantitative analysis of phase space was performed by extracting data from the p2p1 plots, consequently the subsequent analysis is integrated over space.

Figures 8 (a) and (b) show the electron number distribution function (ENDF) and electron energy distribution function (EEDF)[18] respectively at various times during the simulation runs. The data at 1000 ω_p^{-1} is the integral of all the data up to that point in time, while the data at 1370 ω_p^{-1} is the integral of the data from $t = 1000 - 1370\ \omega_p^{-1}$, and so on. These plots show that the fast electron number and energy absorbed into fast electrons is enhanced by the large DSL at early times (during the laser-sub-solid density interaction). Towards the end (the laser-solid interaction) this trend reverses - the small DSL ENDF and EEDF overtake those of the large DSL. This only occurs for the lowest energy electrons, but their numbers are sufficient to dominate the total fast electron number.

The ENDF shown in figure 8 (a) were fitted with Maxwellian distribution functions. It was found that satisfactory fits could only be obtained if two temperatures were used, furthermore the lower temperature component was only well approximated when a non-relativistic Maxwellian was used. The high temperature component was consistently 3× that of the low temperature component. The low temperature component varied as a function of time (the laser beam is gaussian in time) from ∼ 1.5 - 3 MeV, averaging approximately 2.2 MeV. Based on the theoretical peak intensity, this *low* temperature component was best fit by Wilks' scaling, although it is probable that the actual intensities were higher than

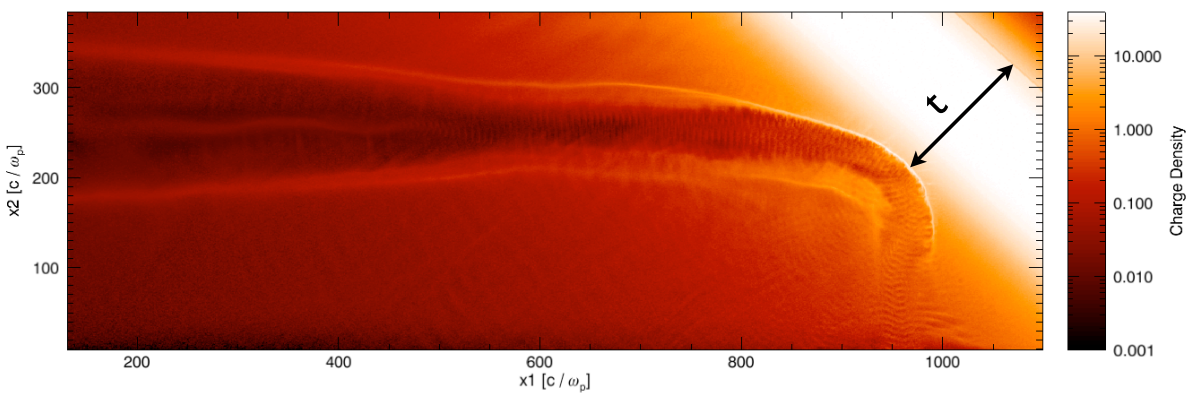

Figure 6. Channelling by, and subsequent refraction of the laser beam in the large density scalelength underdense plasma as it approaches the 45° p-polarised $40n_c$ target (top right). The effective target thickness (t) is depicted. Only part of the simulation box is shown.

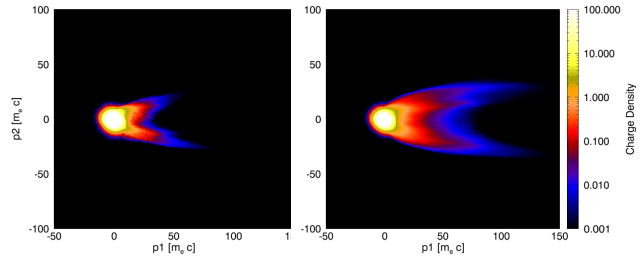

(a) (b)

Figure 7. Phase space plots showing the momentum components parallel (p1), and transverse (p2), with respect to the laser injection axis at time $1035\omega_p^{-1}$ - the pulse is at $0.5n_c$, just 4 μm from n_c: (a) small density scalelength, (b) large density scalelength.

those inferred experimentally due to the dominance of relativistic self-focussing effects in the pre-plasma.

Figure 9 depicts the angular distributions of the fast electron energy - the electron energy angular distribution function (EEADF). At the earliest time 9(a) the laser intensity is too low for the fast electrons to obtain sufficient transverse velocity for the $\mathbf{v} \times \mathbf{B}$ push of the Lorentz force term to be significant, hence the energy distributions are peaked in directions transverse to the laser axis. Subsequently (9(b)) the intensity increases and two lobes of fast electrons at ±20° about 10° off the laser axis (the off axis effect is caused by the target angle) are clearly visible. The energy in the large DSL case is considerably larger than that of the small DSL case. The enhancement in the axial fast electron beam component is also visible in figure 9(c), while by (d) the angular distribution is nearly isotropic. Note varying scales are used for clarity.

The findings shown in figures 8 and 9 indicate that the laser's interaction with the lower density plasma creates a fast electron population with characteristics which are quite distinct to the fast electron population subsequently generated during the laser-solid interaction. Furthermore the number of fast electrons generated within the lower density plasma are enhanced by the larger density scalelength. The population generated within the lower density plasma is subsequently referred to as the fast electron pre-beam, or pre-beam. The main fast electron population is accelerated by the laser from the region of steep plasma gradients close to the target solid surface. This population is *highly* divergent. Subsequently this is referred to as the fast electron main-beam, or main-beam.

Further analysis of the effects of density scalelength on the fast electron pre and main beams, was performed by splitting the fast electrons into two populations based on propagation angle. From figure 9(b), the pre-beam was designated as those electrons which are within a cone

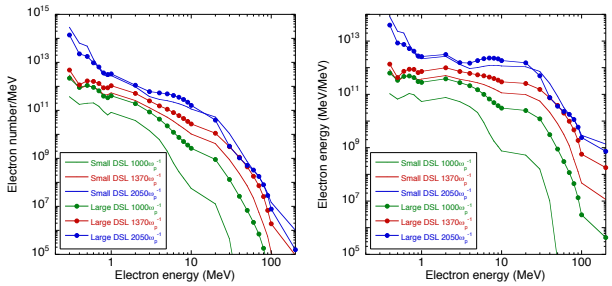

(a) (b)

Figure 8. PIC modelling results: (a) The electron *number* distribution function integrated from the earlier time to the time shown, e.g. the data denoted time $2050\omega_p^{-1}$ is the fast electron number distribution function injected by the laser between 1370 and 2050. At early times the large density scalelength accelerates considerably more electrons to a given energy. Over the whole simulation, the short density scalelength interaction accelerates a higher number of electrons to the lowest energies. (b) Integrals of the electron *energy* distribution function from the previous time to the time shown. Here the trends are similar to those in (a).

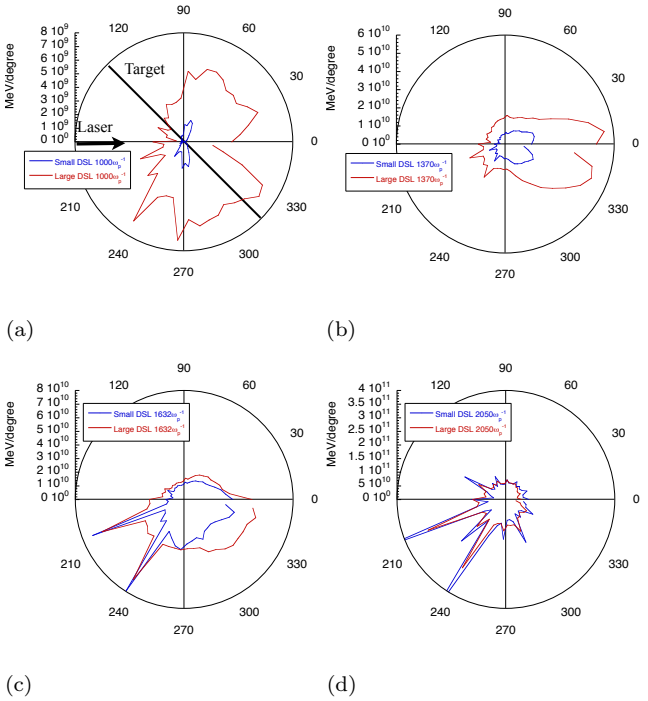

Figure 9. (a)-(d) PIC modelling results showing the angular distribution of the electron *energy* integrated from the earlier time to the time shown, e.g. the data denoted time 1632 ω_p^{-1} is the fast electron energy angular distribution function injected by the laser between 1370 and 1632. 0° is the laser axis, the target plane is shown. At early times (a) the laser $I\lambda^2$ is too low for the electrons to be accelerated forwards by the $\mathbf{v}\times\mathbf{B}$ push. Later (b)-(c) when the laser is more intense and still propagating in the sub-solid density plasma, there is a significant amount of energy peaked either side of the laser axis. This is the 'collimated' fast electron pre-beam component, it is considerably enhanced with the large density scalelength. The electron energy distribution created at late time (d) is near isotropic, this is in part due to the refraction of the laser in the underdense plasma which causes the laser to change direction, accelerating electrons in many directions.

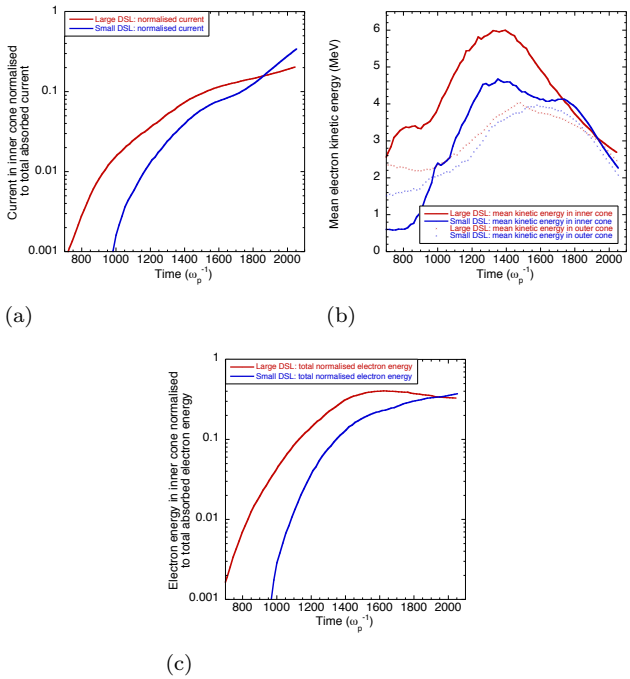

Figure 10. The effect of density scalelength on the fast electron pre-beam: (a) the fast electron current in the pre-beam ($\theta_{1/2} < 30°$) normalised to the total absorbed current ($\theta_{1/2} < 180°$) over the whole small DSL run. The current in the large DSL case is higher during the pre-beam stage, while during the main-beam (laser-solid interaction) the small DSL current is highest, generating the largest total current. The current was found to be basically identical to the electron number. (b) the mean electron kinetic energy in the pre-beam, and that in the forward hemisphere but not in the pre-beam ($30° \leq \theta_{1/2} < 180°$). The large DSL pre-beam is significantly hotter than that of the small DSL pre-beam. The interaction of the laser pulse with the plasma near the target front surface causes the rise in kinetic energy to stagnate then fall. The mean energies of the forward going electrons *not* in the pre-beam are also shown, they are similar for both DSLs and of lower energy than those in the pre-beam - the fast electron mean energy has angular dependance. The peak in the laser intensity occurs at $\sim 1550\omega_p^{-1}$. (c) the energy in the pre-beam normalised to the total absorbed fast electron energy over the whole run. Until the very end of the run there is more energy in the large DSL case (the pre-beam is enhanced). For both DSLs the total energy absorbed into the forward hemisphere of fast electrons was identical.

of half-angle ($\theta_{1/2} < 30°$ measured from the laser axis), while the forward going electrons not in the pre-beam ($30° < \theta_{1/2} < 180°$) were also binned for calculation of the total absorbed population. This binning system is only valid until the laser reaches the front surface ($\sim 1400\omega_p^{-1}$ in both cases) as any fast electrons accelerated subsequently, no matter what their angle, are by definition, part of the main-beam.

The effect of the density scalelength on the fast electron pre-beam is shown in figure 10. Figures 10(a) and (b) show the pre-beam fast electron current and mean kinetic energy (respectively) are considerably enhanced by the large density scalelength. Also of interest in (b) is the angular variation in the fast electron mean energy, furthermore the mean fast electron kinetic energy drops significantly when the laser interacts with the steep plasma density profile near the target front surface. (c) unambiguously shows that with a large DSL more energy is absorbed into the pre-beam fast electrons at early times. Although not shown here, the total absorbed energy in both DSL cases is identical.

Various aspects of the fast electron pre-beam indicate the predominant absorption mechanism of the fast electron pre-beam is $\mathbf{j}\times\mathbf{B}$ acceleration during the underdense/sub-solid density interaction: there are two lobes of electrons either side of p2 = 0 (figures 7 and 9), the electrons are bunched at $\omega/2$ in the x1p1 phase space plots, while the angular dependance of the fast electron temperature is in qualitative agreement with the

classical ejection angle of a fast electron due to $\mathbf{j} \times \mathbf{B}$ acceleration[19].

In summary the PIC modelling shows that the fast electrons accelerated by the laser during the laser-solid interaction when a relatively large density scalelength is present are best described by two distinct populations: those accelerated within the sub-solid density plasma - the fast electron pre-beam, and those accelerated near or at the target front surface - the fast electron main-beam. The pre-beam has considerably lower divergence than that of the main-beam with a half-angle of $\sim 20°$. Depending on the density scalelength, the pre-beam contains approximately 10-30% of the total fast electron energy absorbed into the target. The fast electrons comprising the pre-beam have a higher temperature than those of the main-beam for a given laser intensity. A larger DSL causes the generation of an enhanced pre-beam relative to a smaller DSL, this beam will have higher numbers of fast electrons, increased mean fast electron kinetic energy, and increased fast electron current. During the laser-*solid* interaction, the same large DSL causes the fast electron main-beam, to have a higher fast electron kinetic energy, but lower fast electron number and current (than an equivalent interaction with a smaller DSL). The total energy absorbed into fast electrons was unchanged by the DSL.

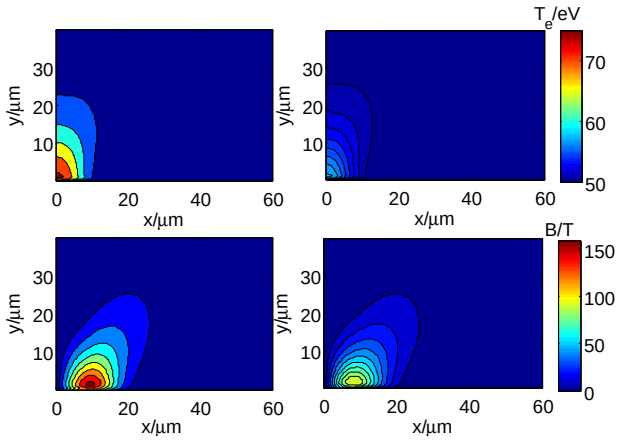

Figure 11. The effects of the fast electron pre-beam, due to symmetry only half of each image is shown: (top) Target electron temperature plots at the end of the pre-beam, the simulation background temperature was set to 50 eV. (left) the large density scalelength fast electron pre-beam heats the target at a depth of 20 µm by ~ 8 eV - considerably less than that observed experimentally (right) the small density scalelength fast electron pre-beam heats the target at a depth of 20 µm by ~ 5 eV. (bottom) magnetic field strength generated within the target at the end of the pre-beam (left) large density scalelength (right) small density scalelength. The magnetic field generated by the large density scalelength pre-beam is significantly larger.

D. Vlasov Modelling

The Vlasov-Fokker-Plank code FIDO[18] was used to evaluate whether the pre-beam has the correct characteristics for the generation of resistive magnetic fields within a solid Aluminium target, as this could potentially explain the reduced divergence and increased target heating observed experimentally.

In order for the pre-beam to effectively collimate the main-beam, the pre-beam must generate a magnetic field of sufficient magnitude to bend the trajectories of a significant proportion of the fast electron main-beam. A simple formula for estimating the magnetic field required to do this for electrons injected at an angle $\theta_{\frac{1}{2}}$ was derived by Bell & Kingham[20]:

$$1 - \cos\theta_{\frac{1}{2}} = 0.06 \frac{R_{\mu\mathrm{m}} B_{\mathrm{MG}}}{[E_{511}(2 + E_{511})]^{1/2}} \qquad (1)$$

This equation shows that in order to collimate 1 MeV electrons injected at 85°, a magnetic field of 4 MG is required, this is the threshold for the complete collimation of the sub-MeV population of the main-beam. Complete collimation would not be expected based on the experimental results. If even a fraction of the electrons were collimated, the increased current density should cause measurable increases in the rear surface temperatures.

For the purposes of these runs, the bulk electron temperature was set to 50 eV in order that the initial Spitzer resistivity value would be a reasonable approximation to that of cold Aluminium. The fast electron number, energy, and angular distribution functions of the injected electrons were based on those from the PIC modelling as shown in figures 9 and 10. A fast electron population representative of the pre-beam was injected for 300 ps then switched to that of the main beam. Three pre-beam regimes were modelled: (1) there was no pre-beam (e.g. if the contrast was ideal), (2) the pre-beam corresponded to that of the small density scalelength interaction, and (3) the pre-beam was that generated by the large DSL interaction.

The spatial characteristics of the PIC fast electron pre-beam number distribution were accurately reproduced, while a highly divergent (basically hemispherical) source was used for the fast electron main-beam. The temporal characteristics of the currents were approximated by switching between the pre and main beam after 300 ps. The magnitudes of the currents were based on the PIC results.

The temperature and magnetic field distributions generated by the two pre-beams (corresponding to those generated by the small and large DSL interactions) are shown in figure 11. It can be seen from figure 11 that the temperature increase due to the pre-beams alone (note the *initial* temperature was 50 eV) are considerably smaller than those observed experimentally for 20 µm targets (experimentally the difference in temperature between the two DSLs was clearest for the 20 µm targets - see figure 2). This implies the extra heating caused di-

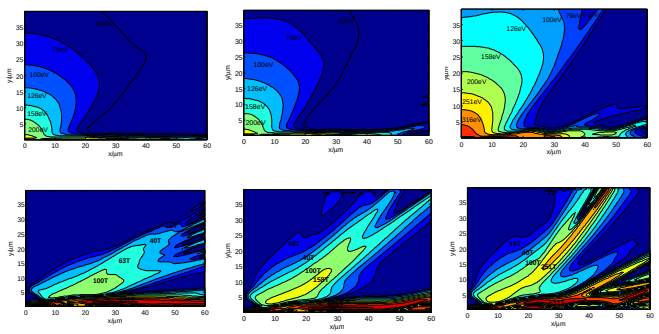

Figure 12. (Top row) Target temperatures 400 fs after the arrival of the fast electron main-beam: (left) no pre-beam, (middle) small density scalelength pre-beam, (right) large density scalelength pre-beam. (Bottom row) The magnetic field within the target 400 fs after the arrival of the main fast-electron beam: (left) no pre-beam, (middle) small density scalelength pre-beam, (right) large density scalelength pre-beam. The temperatures and magnetic fields are both significantly enhanced in the large density scalelength case, in qualitative agreement with the experimental results.

rectly by the enhanced pre-beam due to the large DSL cannot alone explain the experimentally observed temperature increases.

Using the small DSL fast electron pre-beam parameters the magnetic field generated by the end of the pre-beam has a maximum strength of 1.0 MG, while in the large DSL case the pre-beam generated a field of 1.6 MG. Both of these values are less than the 4 MG which was calculated as the minimum value required for complete collimation of the main beam, however some collimation of the lower energy and lower divergence fast electrons will occur. Figure 12, shows that although the magnetic fields were lower than the value required for complete collimation, significant enhancements to the magnetic field and target temperatures have occurred in the large DSL case. This is due to the fact that the partial collimation of the lower energy and lower divergence fast electrons enhances the current density, further increasing the magnetic field, causing the process to self-reinforce, or 'bootstrap'. In the small DSL case, the magnetic field was increased by the bootstrapping process to 1.9 MG, while for the large DSL case the field increased to 4.6 MG.

The modelled temperatures at a depth of 20 µm are greater than those obtained experimentally. This is in part due to the simplified pure Aluminium target used to model the CH-Al-Cu-Al target - the experimental target has a far higher areal electron density. Accounting for this areal electron density effect, it is more accurate to compare the model data at a depth of 40 µm to the experimental targets of $\sim$ 20 µm. Comparing these temperatures and accounting for the 50 eV initial target temperature, shows good quantitative agreement between the modelling and experiment.

In order to establish the effects of resistively generated magnetic fields on target heating, the fast electron pre and main beams' characteristics generated by PIC modelling were used as injection functions for Vlasov modelling. It has been shown that with a pre-beam corresponding to that generated within a small density scalelength, some magnetic field was generated, but the increases in current density were small, causing target temperature increases of $\sim$ 10 eV over the control case with no pre-beam. When the pre-beam corresponded to that from the large DSL interaction, a larger magnetic field was generated, this increased the current density sufficiently to cause the magnetic field to self-reinforce. The temperature rise observed corresponded approximately to that observed experimentally. This indicates that partial collimation of the fast electron main-beam due to magnetic field generation by the pre-beam is a likely explanation for the experimentally observed reduction in fast electron divergence and increase in rear surface temperature as observed with a large density scalelength.

E. Discussion

The observed experimental findings can in large be explained by the fast electron pre-beam which is enhanced by the presence of the large density scalelength and is clearly shown in the PIC modelling. Each of the experimental findings are examined and explained below in light of this.

The experimental data of the total energy reaching the target rear (spatially integrated data) indicates that, if the diagnostic is sensitive to the higher energy electrons (OTR, x-ray background caused by bremsstrahlung), the large density scalelength yields a higher signal, while if the diagnostic is more sensitive to lower energy electrons (Cu K_α imager) the smaller density scalelength yields a stronger signal. The pyrometry (which measures energy deposition by both the high and low energy fast electrons) showed no clear variation with DSL. These findings are fully explained by the results of the PIC modelling as described below.

The fast electrons in the pre-beam have a significantly higher mean kinetic energy than those of the main beam, hence the diagnostics sensitive to the highest energy electrons (OTR, x-ray background caused by bremsstrahlung) will be dominated by the signal of the pre-beam. PIC modelling shows the number, mean kinetic energy, and total energy going into the fast electrons of the pre-beam are enhanced by a large density scalelength, while the instruments sensitive to the higher energy fast electrons also measure a clear enhancement with a large DSL. Hence the signals of the instruments sensitive to the higher energy fast electrons are dominated by the pre-beam which, as has been shown, is enhanced by the large density scalelength.

The Cu K_α imager signal is dominated by lower energy fast electrons as they are dominant in number and have higher collisional cross sections. The PIC modelling clearly shows that the total number of fast elec-

trons absorbed over the whole interaction is significantly enhanced with a small density scalelength, but this dominance is only due to the lowest energy fast electrons. This is in agreement with the spatially integrated Cu K_α imager results - explaining the experimental observations.

Finally the pyrometry observes no clear change in the total energy reaching the target rear as a function of density scalelength. This instrument measures energy deposition at the target rear by both the high and low energy fast electrons via Ohmic and collisional heating. The PIC modelling showed that the total energy absorbed was invariant with density scalelength, thereby explaining the pyrometric experimental observations.

The rear surface temperatures measured by the Cu K_α spectroscopy and pyrometry were of the same order, however the spectroscopy did not show the factor of four temperature increase for the thinner targets and large density scalelength. This was ascribed to the lack of sensitivity of the spectrometer, similar observations have been made over numerous expeirments.

All of the diagnostics found the spot-size HWHM caused by the electron transport within the target was reduced with a large density scalelength. The reduction in the spot-size HWHM was considerably larger in the cases of the thermal and OTR than that of the Cu K_α imager. The reduction is attributed to the more collimated nature of, and increased current in, the fast electron pre-beam generated by the sub-solid density interaction in the large DSL case. The exact mechanism by which this reduction in spot size occurs is discussed in more detail below.

Vlasov modelling showed that the pre-beam only increased the target temperature by ~ 8 eV in the large DSL case - insufficient to explain the pyrometrically observed increases in rear surface temperature.

It was found that the fast electron pre-beam generated by the small density scalelength could generate some magnetic field but it was insufficient to cause significant collimation of the main-beam, and the observed temperatures rises were small. The large density scalelength interaction was sufficient to cause partial collimation of the subsequent fast electron main-beam and resultant increases in rear surface temperatures were of the order of 60 eV - similar to those observed experimentally.

Fast ignition inertial confinement fusion requires the ignition electron beam to have a mean energy of ~ 1 MeV. The enhancement in forward energy flux which has been demonstrated with the large density scalelength pre-plasma is principally due to the creation of a pre-beam of fast electrons of increased number and mean kinetic energy but reduced divergence (in comparison to those fast electrons generated near the solid surface). The fast electron pre-beam does not have the correct characteristics for a fast ignition ICF driver as the mean fast electron kinetic energy is too high and there are insufficient electrons within the pre-plasma, however it may possess useful characteristics with regards to the creation of a magnetic field structure which could collimate (or at least reduce the divergence of) the highly divergent, colder electrons accelerated at the solid-surface (be that an embedded cone or surface of a compressed ICF capsule).

$B \approx \eta j t/R$ approximates the resistively generated magnetic field by a fast electron beam propagating in a solid[21], where B is the magnetic field, j the current density, t the laser duration and R the electron beam radius. This is now applied in a fast ignition relevant scenario. Assuming $\eta = 1.6 \times 10^{-8}\Omega - m$ (Spitzer resistivity for 1 keV D-T), a fast electron beam radius of 10 µm, a laser pulse duration of 1 ps, and a mean fast electron energy of 5 MeV (the temperature of the fast electron pre-beam), the total energy in the electron beam would be required to be ~ 500 J in order to create a 400 T magnetic field which extends 200 µm into the solid, compressed D-T. Within this field the 1 MeV electrons will have a Larmor radius of the order of the magnetic field radius, and hence will be confined by the magnetic field 'structure'. This shows that in principle it is possible to use the initial high energy population of electrons to draw a sufficient resistive return current within a fast ignition relevant scenario in order to generate a magnetic field suitable for the collimation of the bulk electron population.

This scheme is similar to the artificial collimation technique proposed by Robinson et al[21], however it has the advantage that the initial population is of higher temperature and importantly, is more collimated than that of the bulk electron population, hence it may be possible to set up a magnetic field which extends deep into the compressed DT core, guiding the fast electrons within the DT until they deposit their energy.

F. Summary

In conclusion, when a sufficiently large density scalelength exists (see table I), the fast electron beam resulting from the laser-solid interaction is best described by two distinct populations: those accelerated within the sub-solid density plasma - the fast electron pre-beam, and those accelerated near or at the target front surface - the fast electron main-beam.

The fast electron pre-beam has considerably lower divergence than that of the main-beam with a half-angle of $\sim 20°$. Depending on the density scalelength, the pre-beam contains approximately 10-30% of the total fast electron energy absorbed into the target. The fast electrons comprising the pre-beam have a higher temperature than those of the main-beam for a given laser intensity.

A larger DSL causes the generation of an enhanced fast electron pre-beam during the sub-solid density interaction, this beam will have higher numbers of fast electrons, increased mean kinetic energy, and increased current. The same large DSL causes the main-beam generated at or near the solid surface, to have a higher fast electron kinetic energy, but lower fast electron number and current. The total energy absorbed into fast elec-

trons was unchanged by the DSL.

There is strong evidence that with a larger density scalelength, the fast electrons heat a smaller cross sectional area of the target, causing the thinnest targets to reach significantly higher rear surface temperatures. Based on the modelling performed it is most likely this is due to the enhanced fast electron pre-beam associated with the large density scalelength interaction. This generates a magnetic field within the target of sufficient magnitude to partially collimate the subsequent more divergent fast electron main-beam.

The fast electron pre-beam may have suitable properties to generate a magnetic field within the compressed DT core of a fast ignition ICF capsule. This magnetic field structure would act to collimate the subsequent population of highly divergent electrons accelerated from the solid surface. Simple calculations show this is energetically feasible requiring less than 1% of the ignition laser energy. More detailed work is required to accurately assess the viability of such a scheme.

This work has two main findings in the context of fast ignition. Firstly, if it is not possible to generate a magnetic field in the manner described above, higher contrasts are advantageous for fast ignition as they increase the fast electron current and reduce the fast electron's mean kinetic energy. Secondly, the hole boring phase of cone-less fast ignition inertial confinement fusion may be used to generate a fast electron pre-beam with suitable characteristics for the divergence reduction of the fast electron main-beam generated by the laser-solid interaction.

REFERENCES

[1] E. L. Clark *et al.*, Phys. Rev. Lett. **84**, 670 (2000).

[2] R. A. Snavely *et al.*, Phys. Rev. Lett. **85**, 2945 (2000).

[3] A. Maksimchuk *et al.*, Phys. Rev. Lett. **84**, 4108 (2000).

[4] D. Hoarty *et al.*, High Energy Density Phys. **3**, 115 (2007).

[5] M. Tabak *et al.*, Phys. Plamas **1**, 1626 (1994), part 2.

[6] A. J. Kemp, Y. Sentoku, and M. Tabak, Phys. Rev. E **79**, 066406 (2009).

[7] S. C. Wilks and W. L. Kruer, IEEE J. Quantum Electronics **33** (1997).

[8] P.-H. Maire, J. Breil, and S. Galera, International Journal for Numerical Methods in Fluids **56**, 1161 (2008).

[9] A. L. Meadowcroft, C. D. Bentley, and E. N. Stott, Review of Scientific Instruments **79**, 113102 (2008).

[10] H.-K. Chung *et al.*, High Energy Density Physics **1**, 3 (2005), ISSN 1574-1818.

[11] R. Kodama, K. Okada, and Y. Kato, Review of Scientific Instruments **70**, 625 (1999).

[12] N. C. Woolsey *et al.*, Phys. Rev. E **57**, 4650 (1998).

[13] A. R. Bell *et al.*, Plasma Phys. & Controlled Fusion **39**, 653 (1997).

[14] J. J. Santos *et al.*, Phys. Rev. Lett. **89** (2002), fast electron transport in ultraintense laser pulse interaction with solid targets by rear-side self-radiation diagnostics 10.1103/PhysRevLett.89.025001.

[15] J. Zheng *et al.*, Phys. Plamas **10**, 2994 (2003).

[16] S. D. Baton *et al.*, Phys. Rev. Lett. **91**, 105001 (2003).

[17] R. Fonseca *et al.*, in P. Sloot *et al.*, editors, *Computational Science — ICCS 2002*, volume 2331 of *Lecture Notes in Computer Science*, pages 342–351, Springer Berlin / Heidelberg (2002).

[18] M. Sherlock, Phys. Plamas **16**, 103101 (2009).

[19] R. B. Stephens *et al.*, Phys. Rev. E **69**, 066414 (2004), copyright (C) 2008 The American Physical Society Please report any problems to prola@aps.org PRE.

[20] A. R. Bell and R. J. Kingham, Phys. Rev. Lett. **91**, 035003 (2003), copyright (C) 2008 The American Physical Society Please report any problems to prola@aps.org PRL.

[21] A. P. L. Robinson, M. Sherlock, and P. A. Norreys, Phys. Rev. Lett. **100**, 025002 (2008).

An Analytical Model for the Energy of Relativistic Electrons Escaping a Plasma

Contact *m.sherlock@imperial.ac.uk*

M.Sherlock
Blackett Laboratory
Imperial College London
London SW7 2BZ

H.Schmitz
Blackett Laboratory
Imperial College London
London SW7 2BZ

C.P.Ridgers
Blackett Laboratory
Imperial College London
London SW7 2BZ

Introduction

In relativistic laser-plasma interactions, highly energetic electrons are produced which stream through the target plasma. Once these electrons reach the target's rear surface they can in principle leave the target and propagate through the vacuum, where they may be detected by a spectrometer [1]. The energy of the electrons once they reach the spectrometer is not representative of their energy just prior to exiting the target, because the electrons generate an electric field which attempts to pull them back toward the target. It might be argued that the energy of electrons that reach far into the vacuum is less than their energy as they leave, because the field is decelerating. On the other hand it could be argued that only the very highest energy electrons are able to reach far into the vacuum because they are the only ones with sufficient energy to overcome the decelerating fields. An idealised experimental setup depicting this scenario is shown in Fig. 1.

We will show with a simple analytical model that the energy distribution function for electrons that reach far into the vacuum is such that their energy is lower by a factor of about 2. This result is independent of geometry (and hence is valid in 3-dimensions).

The Model

Fig. 2 depicts the model used, which is 1-dimensional. For educational purposes we first treat the electrons as discrete particles, which leave a plasma target with some given forward momentum p_0. As they propagate into the vacuum region, they will set up an electric field which can easily be found from Gauss' Law:

$$\varepsilon_0 E_x A = Q_{left}$$

in which A is the cross-sectional area, E_x is the field and Q_{left} is the amount of charge found to the left of the surface of interest. Q_{left} can be found from the total charge Q_{total} by considering the charge to the right (which includes the target):

$$\varepsilon_0 E_x A = Q_{total} - Q_{right}$$

Since the total charge is zero we have

$$\varepsilon_0 E_x A = -Q_{right}$$

By labeling the electrons with index i=1,2,3…, we know that

$$Q_{right} = -ie$$

and hence the field at particle i is just

$$E_x(x_i) = i\frac{e}{\varepsilon_0 A}$$

This idea predicts a field which rises linearly with particle index, from zero at the front of the electron stream up to some maximum value at the target edge and is valid so long as particles do not decelerate so much as to cross one another's paths. Once this begins to occur (near the plasma edge), the field instead becomes a Debye sheath. Thus ahead of the Debye sheath there is a linear field which we call the "escape sheath".

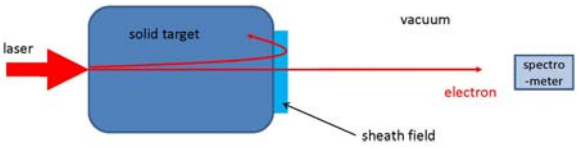

Fig. 1 The idealised experimental setup.

In order to take into account the effect of the escape sheath on particle energies it is preferable to use instead a continuous model for the electron current, which is easily adapted from the discrete model by making the following replacement:

$$E_x(x_i) = i\frac{e}{\varepsilon_0 A} \rightarrow E_x(\tau) = -\int_0^{\tau} \frac{j(t')}{\varepsilon_0} dt'$$

in which the particle index is essentially replaced by τ, the time at which an infinitesimal charge element leaves the target. In this field the particle equations of motion are simply:

$$\frac{dp(\tau,t)}{dt} = p_0 - eE_x(\tau)$$

and

$$x(\tau,t) = \int_0^t \frac{p(\tau,t')}{m\sqrt{1+p(\tau,t')^2}} dt'$$

in which the momentum p is normalized to mc.

For the simple case of a constant current j_0 the parametric solution to these equations is:

$$p(\tau,t) = p_0 - j_0\tau(t-\tau)$$

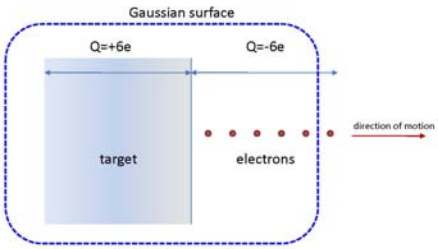

Fig. 2 The application of Gauss' Law.

and

$$x(\tau,t)=\frac{\sqrt{1+p_0^2}-\sqrt{1+p_0^2+j_0^2\tau^2(t-\tau)^2+2p_0j_0\tau(t-\tau)}}{j_0\tau}$$

These solutions are plotted at various times in phase-space in Fig. 3. We are interested in the energy distribution of the bunch of particles that escape. This can be found by considering the solution for the particle momentum:

$$p(\tau,t)=p_0-j_0\tau(t-\tau)$$

and expanding this about τ=0 for small τ and large t:

$$p\approx p_0+const\times\tau$$

which, approximately, gives f(p)=constant for $p<p_0$ and f(p)=0 otherwise. The average energy can then be found simply from

$$\Rightarrow\langle E\rangle=mc^2\int_0^{P_0}(\gamma(p)-1)f(p)dp=\frac{1}{2}(\sqrt{1+p_0^2}-1)+\frac{\operatorname{arcsinh}(p_0)}{p_0}$$

which, in the ultra-relativistic limit, becomes:

$$\frac{\langle E\rangle}{E_{injected}}=\frac{\langle E\rangle}{\sqrt{1+p_0^2}-1}\approx\frac{1}{2}$$

Hence the average energy of electrons that escape far into the vacuum is about half of their energy on leaving the target.

3D effects can be included by considering that, rather than the planar geometry considered here, the most extreme non-planar case corresponds to an electron stream that propagates spherically (filling a hemisphere on the back of the target). Repeating the above calculation in spherical geometry changes the field structure but not the energy of the electrons which reach the detector.

This reduction in energy has been verified with Particle-In-Cell and Vlasov simulations.

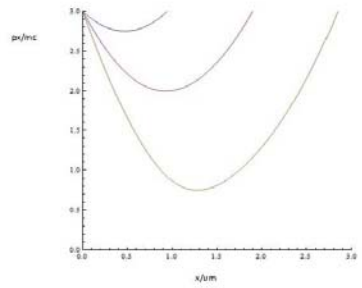

Fig. 3 Particle trajectories in phase-space.

Conclusions

A simple analytical model has been derived for the distribution of energetic particles that leave a plasma target and escape far into the vacuum. The average energy of these particles is about one-half of their initial energy on leaving the target. This result has implications for intense laser-plasma interaction experiments which measure the escaping electron energy spectrum and may explain why some experiments find the vacuum energy to be reduced as compared to the laser-generated (Ponderomotive) energy [1].

References

1. T.Tanimoto *et al*. Phys. Plasmas **16** 062703 (2009).

Numerical simulation of plasma-based laser pulse compression to petawatt powers via Raman amplification

Contact *raoul.trines@stfc.ac.uk*

R.M.G.M. Trines, R. Bingham and P.A. Norreys
Central Laser Facility, STFC Rutherford Appleton Laboratory
Didcot, Oxon, OX11 0QX, United Kingdom

R.A. Cairns
University of St Andrews
St Andrews, Fife KY16 9AJ, United Kingdom

F. Fiúza, R.A. Fonseca and L.O. Silva
GoLP/Instituto de Plasmas e Fusão Nuclear - Laboratorio Associado, Instituto Superior Técnico
1049-001 Lisbon, Portugal

Contemporary high-power laser systems make use of solid-state laser technology to reach petawatt pulse powers. The breakdown threshold for optical components in these systems, however, demands beam diameters up to 1 metre. Raman amplification of laser beams promises a breakthrough by the use of much smaller amplifying media, i.e. millimetre diameter wide plasmas. Through the first large scale multi-dimensional particle-in-cell simulations of this process, we have identified the parameter regime where multi-petawatt peak laser powers can be reached, while the influence of damaging laser-plasma instabilities is only minor. Such powerful laser pulses have many applications in e.g. plasma-based particle acceleration, laser-driven nuclear fusion and laboratory astrophysics.

In Raman amplification of laser pulses, the energy of a long, low intensity pump pulse is transferred to a short probe pulse via the Raman backscatter instability in plasma [1], [2], effectively making it a pulse compression technique. The immediate advantage of this scheme is that it uses plasma as an amplifying medium rather than solid state optics: theoretically, the intensity threshold for plasma-based amplification is 100,000 times larger than the damage threshold for solids at 10^{12} W cm^{-2}. Initial theoretical studies indicated that the probe could be amplified to more than 10^{17} W cm^{-2} and 100 PW, and subsequently focused to 10^{25} – 10^{27} W cm^{-2} [3], [4]. So far, these results have not yet been demonstrated in experiments: while intensities of 10^{16} – 10^{17} W cm^{-2} have been obtained [5], [6], the corresponding spot sizes were only around 15 μm, leading to no more than 10-100 GW output power which is 4 orders of magnitude lower than the most advanced solid-state laser systems in operation today.

Previous studies investigated parameter regimes where high probe intensities could be obtained, while keeping the pump pulse free from premature Raman back- and sidescatter, or inverse bremsstrahlung [7], [8], [9]. However, the theory and simulations presented in those works are all 1-dimensional, and therefore do not model transverse effects like self-focusing or filamentation. Neither can they conclusively demonstrate that the high intenstities obtained via Raman amplification can be maintained across large spot diameters, leading to high powers. A recent systematic numerical investigation into Raman amplification using fully self-consistent multi-dimensional particle-in-cell simulations, revealed that Raman amplification of wide laser pulses to ultrahigh powers (in addition to ultrahigh intensities) is definitely possible, but only for certain combinations of laser and plasma parameters [10]. Through a series of large-scale particle-in-cell simulations, it was revealed that there is a narrow but definite parameter window for which Raman amplification of wide laser pulses is both efficient and free from both longitudinal and transverse instabilities. Outside this window, Raman amplification fails either because of poor efficiency or because of parasitic instabilities destroying the growing probe.

A summary of our simulation results is shown in Table 1. A multitude of nonlinear effects have been encountered, such as probe saturation due to RFS and wakefield generation, breaking of the Raman backscattering (RBS) Langmuir wave that couples pump and probe, parasitic pump RBS and transverse filamentation of both pump and probe pulses in two-dimensional (2D) simulations. In general, it has been found that increasing the pump intensity and/or the plasma density will lead to more efficient amplification, but will also increase the growth of unwanted instabilities of both pump and probe, leading to a poor probe envelope and reduced probe focusability.

I_{pump} (Wcm^{-2})	ω_0/ω_p			
	10	14	20	40
10^{14}	RFS	10^{17}	10^{17}	ineff.
10^{15}	RFS, fil	4×10^{17}	4×10^{17}	ineff.
10^{16}	RFS	RFS	RFS, fil	RFS, ineff.

Table 1: Summary of our simulation results, for various values of the pump intensity and plasma density, and a fixed pump wavelength of 800 nm. The plasma density is expressed as the ratio of the laser frequency ω_0 and the plasma frequency ω_p. For each case where the probe was strongly amplified while retaining a smooth envelope, the FWHM probe intensity is shown in Wcm^{-2}. For each case where the probe was either poorly amplified or did not have a smooth profile, the reason (Raman forward scattering (RFS), filamentation (fil.), low energy-transfer efficiency (ineff.)) is listed. It follows clearly that the pump FWHM intensity should not exceed 10^{15} Wcm^{-2}, while $14 < \omega_0/\omega_p < 20$ is recommended. A higher pump intensity leads to a higher absolute probe intensity, but the highest relative amplification is found for lower pump intensities because probe saturation is postponed in that case.

The simulation results presented in Ref. [10] and depicted in Figure 1 have been obtained used the 2-dimensional particle-in-cell (PIC) codes XOOPIC [11] and OSIRIS [12]. These codes solve Maxwell's equations directly, resolving the electro-magnetic fields down to the laser wavelength and period, without resorting to pulse envelope models or other approximations aimed at bypassing the short temporal and spatial scales of the laser carrier wave. The relativistic Lorentz force is used to calculate the motion of the plasma particles, while relativistic expressions are used to derive the charge and current densities from the positions and momenta of the particles. This approach allows the modelling of laser intensities up to at least 10^{23} W/cm^2, and a number of parasitic instabilities

of the laser pulses, such as Raman forward scattering, pulse modulation or filamentation, and parasitic pump Raman back- and side scattering [13], as well as any effects of trapped particles on the RBS Langmuir wave (Landau damping, wave breaking) are included in the simulations by default. The graphs of the simulation results were prepared using VisXD, the advanced visualization routines of the OSIRIS framework, described in Ref. [14].

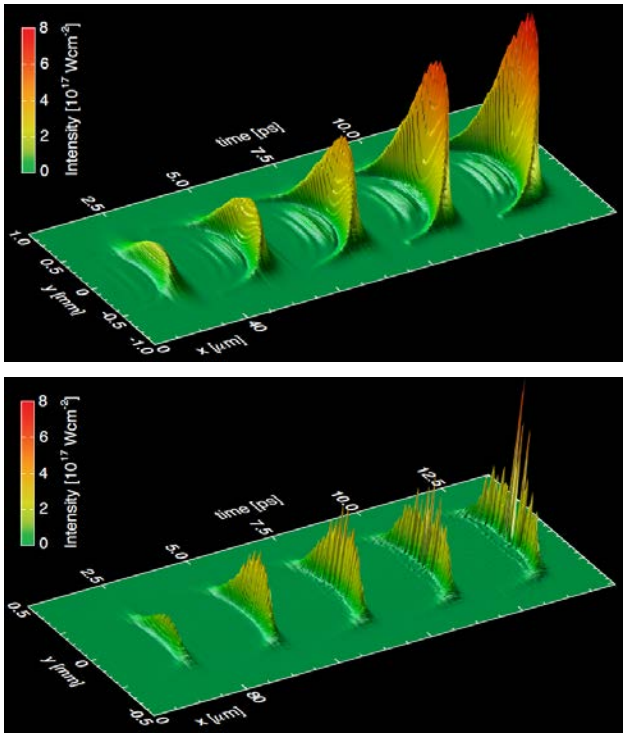

Figure 1: Raman amplification for $\acute{E}_0/\acute{E}_p = 20$ (top) and $\acute{E}_0/\acute{E}_p = 10$ (bottom), all other parameters equal. Shown are five snapshots of the growing probe at 2.5 ps intervals. The x and y scales refer to the local coordinates of the probe pulse itself, and the 'time' scale refers to the probe propagation time. The amplified probe displayed in the top frame has a mostly smooth intensity envelope, as the reduced plasma density keeps probe filamentation and other damaging instabilities in check. The amplified probe in the bottom frame also shows strong and efficient growth, but, at the higher plasma density used in this simulation, uncontrolled filamentation destroys the probe envelope and compromises focusability.

In the top frame of Figure 1, five snapshots of the growing probe are presented corresponding to 0.8, 1.6, 2.4, 3.2 and 4.0 mm of propagation. The plasma density was chosen such that $\acute{E}_0/\acute{E}_p = 20$. This ensures that the probe retains a smooth envelope during the entire simulation. After amplification, the probe has an average intensity of about 4×10^{17} W/cm^2, corresponding to a final probe power, duration and energy of 1.5 PW, 25 fs and 34 J respectively. Since the pump has a power, duration and energy of 4 TW, 25 ps and 96 J respectively, this corresponds to an estimated efficiency of 35%. The amplified probe has sufficient quality that it can be focused down to 1 μm FWHM and 1.0×10^{23} W/cm^2 FWHM intensity. The bottom frame shows the results of a simulation that is similar in all aspects, except that $\acute{E}_0/\acute{E}_p = 10$ instead of 20. The amplified probe in this simulation also shows strong and efficient growth, but, because of the higher plasma density, uncontrolled filamentation destroys the probe envelope and compromises focusability. This emphasizes the importance of considering transverse effects and instabilities when studying Raman amplification, to ensure that the high peak intensity of the amplified probe can be maintained across a large spot size, and that the probe envelope is smooth to preserve focusability.

In conclusion, we have studied Raman amplification of high-power and high-intensity laser pulses in low-density plasma. A 25 ps, 4 TW laser pulse has been compressed to 25 fs and 1.5 PW. It also follows from the simulation results that, for these optimal parameters, Raman amplification can be extended to cm-wide spot sizes, allowing the compression of a 1 PW, 25 ps pump pulse to 300 PW in as little as 30 fs.

Acknowledgements

This work was supported by the STFC Accelerator Science and Technology Centre, by the STFC Centre for Fundamental Physics, by EPSRC through grant EP/G04239X/1 and by FCT (Portugal) through grant PTDC/FIS/66823/2006. We would like to thank W. Mori for discussions, the Plasma Theory and Simulation Group of UC Berkeley for the use of XOOPIC and the OSIRIS consortium for the use of OSIRIS. Simulations were carried out on the Scarf-Lexicon Cluster (STFC RAL), the IST Cluster (IST Lisbon) and the Hoffman Cluster (UCLA).

References

1. G. Shvets et al., "Superradiant Amplification of an Ultrashort Laser Pulse in a Plasma by a Counterpropagating Pump", Phys. Rev. Lett. 81, 4879-4882 (1998).
2. V.M. Malkin et al., "Fast Compression of Laser Beams to Highly Overcritical Powers", Phys. Rev. Lett. 82, 4448-4451 (1999).
3. N.J. Fisch and V.M. Malkin, "Generation of ultrahigh intensity laser pulses", Phys. Plasmas 10, 2056-2063 (2003).
4. V.M. Malkin and N.J. Fisch, "Manipulating ultraintense laser pulses in plasmas", Phys. Plasmas 12, 044507 (2005).
5. J. Ren et al., "A new method for generating ultraintense and ultrashort laser pulses", Nature Physics 3, 732-736 (2007).
6. R.K. Kirkwood et al., "Amplification of an ultrashort pulse laser by stimulated Raman scattering of a 1 ns pulse in a low density plasma", Phys. Plasmas 14, 113109 (2007).
7. D.S. Clark and N.J. Fisch, "Operating regime for a backward Raman laser amplifier in preformed plasma", Phys. Plasmas 10, 3363-3370 (2003).
8. D.S. Clark and N.J. Fisch, "PIC simulations of Raman laser amplification in preformed plasmas", Phys. Plasmas 10, 4848-4855 (2003).
9. V.M. Malkin and N.J. Fisch, "Quasitransient regimes of backward Raman amplification of intense x-ray pulses", Phys. Rev. E 80, 046409 (2009).
10. R.M.G.M. Trines et al., "Simulations of efficient Raman amplification into the multipetawatt regime", Nature Physics 7, 87-92 (2011).
11. J.P. Verboncoeur, A.B. Langdon and N.T. Gladd, "An object-oriented electromagnetic PIC code", Comp. Phys. Comm. 87, 199-211 (1995).
12. R.A. Fonseca, L.O. Silva, R.G. Hemker, et al., "OSIRIS, a three-dimensional fully relativistic particle in cell code for modeling plasma based accelerators", Lect. Not. Comp. Sci. 2331, 342-351 (2002).
13. A.A. Solodov, V.M. Malkin and N.J. Fisch, "Pump side scattering in ultrapowerful backward Raman amplifiers", Phys. Rev. E 69, 066413 (2004).
14. R. A. Fonseca et al., "One-to-one direct modeling of experiments and astrophysical scenarios: pushing the envelope on kinetic plasma simulations", Plasma Phys. Contr. Fusion 50, 124034 (2008).A reference

Use of the Debye-Waller Factor as a Temperature Diagnostic in Strongly Coupled Non-Equilibrium Plasmas.

Contact *thomas.white@physics.ox.ac.uk*

T. G. White, J. Mithen, C. D. Murphy, G. Gregori
Clarendon Laboratory, University of Oxford

D. Hochhaus, P. Neumayer
GSI Helmholtzzentrum fr Schwerionenforschung GmbH

P. Davis, S. H. Glenzer, T. Ma, S. Le Pape
Lawrence Livermore National Laboratory

B. Crowley
AWE, Aldermaston

Introduction

A complete description of the ion dynamics within the warm dense matter (WDM) regime is important for describing many physical phenomena ranging from phase transitions within the interior of large astrophysical objects [1] to temperature relaxation rates during the internal processes of inertial confinement fusion [2]. Recent advances in both experimental and theoretical high energy density physics [3] have permitted these extreme states of matter to be formed in the laboratory and characterization methods are being rapidly developed and improved upon. Here we look at adapting a conventional condensed matter technique to study ion dynamics in the WDM state. This state is characterized by high pressure (≈1 Mbar), temperature (≈1 eV) and approximately solid density [4, 5] and represents a major challenge theoretically, computationally and experimentally. It lies in the regime between traditional solid state and plasma physics where expansion techniques are no longer applicable and neither the kinetic nor the potential energy can be treated perturbatively.

High density plasmas can be parameterized by the ion-ion coupling parameter,

$$\Gamma = \frac{Q^2}{4\pi\epsilon_0 k_B T_i a} \ , \qquad (1)$$

where Q is the ionic charge, $T_{i(e)}$ the ion (electron) temperature, $a=(3/4\pi n)^{1/3}$ the Wigner-Seitz radius (average inter-particle separation) and n the ion number density. Equation (1) expresses the ratio of the pairwise Coulomb interaction to the average kinetic energy. WDM lies in the region where the coupling parameter is of order unity or greater. In this state strongly coupled ions, non-equilibrium species ($T_e/T_i > 1$) and non-negligible electron degeneracy play an important role in defining structural dynamics [6]. At higher ion-ion coupling parameters the influence of the Coulomb interaction is increased and the ions arrange themselves around their equilibrium lattice positions. The ions oscillate around these positions and consequentially the ion acoustic waves present in a less strongly coupled plasma (fluid) are now replaced by phonons which must be treated quantum mechanically.

In the laboratory these non-equilibrium systems can occur when matter is exposed to ultra-intense optical laser radiation. Energy is transferred 'instantaneously' to the electrons in the system and the degree of electron-phonon coupling determines the inter-species temperature relaxation rates. One area that has received considerable attention and is based on these equilibration rates is the process of ultra-fast non-thermal `melting` [7, 8]. Here an ultra intense laser beam can create a strongly perturbed potential surface (due to the excited state of the energetic electrons) causing high carrier density and in some cases exceeding that of the crystal stability limit. The residual motion of the atoms then causes disordering of the crystal on timescales much shorter than the usual propagation of a melt front. Conversely in gold the electron excitation is thought to produce a hardening of the lattice structure [9]. In all cases study into these non-equilibrium processes require simultaneous measurement of the electron and ion temperatures.

Currently many techniques exist to determine the electron temperature in a dense plasma [10]. However diagnosing the ion temperature, particularly at temperatures of a few eV or below, is far more difficult without resorting to interpolation based surface techniques such as emission spectroscopy [11], and interferometery [12, 13]. The method investigated in this report directly measures the ion bulk temperature through x-ray scattering from a strongly coupled plasma. The Debye-Waller (DW) technique has long been used in solid state physics as a way to characterize the displacement of atoms in a crystal from equilibrium through the intensity of elastically scattered radiation (Bragg diffraction) [14]. Here we examine the applicability of this technique to infer ion dynamics and temperature in matter transitioning from cold condensed matter to the WDM state. This is done through a combination of the solid state DW theory (section 1) and large-scale molecular dynamic simulation (section 2). Finally we evaluate the applicability of this technique through experimental results from proton heated highly orientated pyrolytic graphite (HOPG) (section 3).

1. Temperature Dependent Debye-Waller Factor

In the kinematic limit where radiation interacts only weakly with a sample it has been shown that the intensity of scattered radiation at position **R** is proportional to the value of the dynamic structure factor S, the incident power P_0 and the inverse irradiated area A,

$$P_s(\mathbf{R},\omega)d\Omega d\omega \propto \frac{P_0}{A} S(\mathbf{k},\omega) \ , \qquad (2)$$

where ω is the frequency shift of the scattered photon and Ω the solid angle [10]. In the non-relativistic limit for near-elastic scattering, $|\mathbf{k}|=2k_0\sin(\theta/2)$ for incident x-rays with wave vector $|\mathbf{k}_0|=4\pi/\lambda_0$. Here, θ is the scattering angle and λ_0 the probe wavelength. The dynamic structure factor is the spatial and temporal Fourier transform of the dynamic electron density-density auto-correlation function, known as the van Hove function [15]. In effect, the scattered radiation profile from a dense plasma contains information on the motion and position of the particles within.

In a solid it is natural to decompose the motion of the ions into multiple terms, $\mathbf{R}_i$ which represents the equilibrium position of the ions in the lattice as well as $\mathbf{u}_{oi}(t)$ and $\mathbf{u}_{ti}(t)$ which represent the displacement of ions from these points, oscillatory and translational motion respectively. Following the derivation by Gregori [16, 17] we derive a set of equations

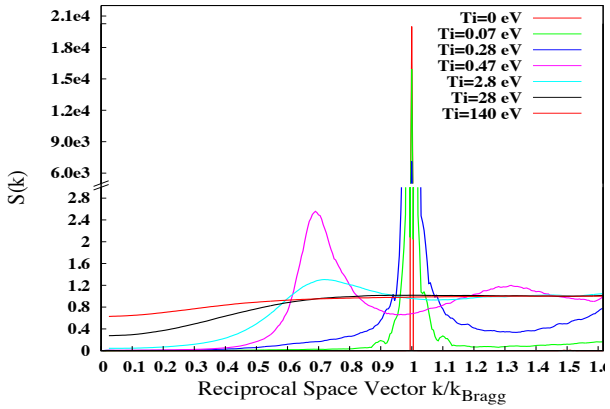

Figure 1. Ion-Ion Static Structure Factor for graphite where k is aligned perpendicular to the planes. Obtained from molecular dynamic simulations performed with LAMMPS (see section 2).

showing the temperature dependence of the ion-ion static structure factor,

$$S(\mathbf{k}) = F_t(\mathbf{k},0)\left(1 - e^{-2W} + e^{-2W}\, b(\mathbf{k})\right), \quad (3)$$

$$F_t(\mathbf{k},t) = \frac{1}{N}\sum_{i=1}^{N}\sum_{j=1}^{N}\langle e^{-i\mathbf{k}.[\hat{\mathbf{u}}_{ti}(0)-\hat{\mathbf{u}}_{tj}(t)]}\rangle_{Ti}, \quad (4)$$

$$b(\mathbf{k}) = \frac{1}{N}\sum_{i=1}^{N}\sum_{j=1}^{N} e^{-i\mathbf{k}.[\mathbf{R}_i-\mathbf{R}_j]}, \quad (5)$$

where $\langle ... \rangle_{Ti}$ denotes an ensemble average of N particles at temperature T_i and $S(k)=\int S(k,\omega)d\omega$. Equation (4) can be thought of a translational structure factor ($\approx$N in a solid) and (5) as the crystal Bragg peak. Eq (3) describes, to first order, the reduction in coherent scattering as the parameter $2W=k^2\langle \mathbf{u}^2_{oi}\rangle$ is increased. In the harmonic approximation [18,19] the displacement of an atom from its equilibrium position can be related to the temperature T_i through,

$$2W = \frac{3k^2\hbar^2}{Mk_BT_D}\left[\left(\frac{T_i}{T_D}^2\right)\int_0^{T_D/T_i}\frac{udu}{e^u-1} + \frac{1}{4}\right], \quad (6)$$

Hence the temperature of the ions can be related to the decreased intensity of the Bragg scattered signal. However, as pointed out by Ernstorfer et al [9] great care must be taken when using (6) in a highly non-equilibrium system. In such cases the electron excitation can impact the Debye temperature, T_D, dramatically and as such T_D should be treated as $T_D(T_e)$. A full *ab-initio* analysis of the phonon density of states at higher electron temperatures is necessary to calculate an exact value of T_D, however this value can be approximated. One method is to use the definition of the Debye temperature in a plasma,

$$T_D = \frac{\hbar}{k_B}\left(\frac{Ze^2n_e}{4\pi\epsilon_0 M}\right)^{\frac{1}{2}}, \quad (7)$$

as given in [20] which is based upon the Bohm-Staver relation in simple metals. Here Z is the ionization, n_e the electron density, and M the ion mass. In such cases the temperature dependence comes in through the degree of ionization $Z=Z(T_e)$. Another method is to extract the Debye temperature from large-scale molecular dynamic simulations (Section 2). In this report we consider both methods of calculating T_D for graphite in the WDM regime.

2. Molecular Dynamics Simulation

An MD simulation was constructed to approximate the conditions of warm dense graphite investigated in section 3. To model the bonds between the layers a screened Coulomb potential (Yukawa) was used,

$$\phi(r) = \frac{Q^2}{4\pi\epsilon_0 r}e^{-k_D r}, \quad (8)$$

where the parameter k_D is related to the screening length by $k_D = 1/\lambda_D$. The advantage of using the screened Coulomb potential is that it can approximate the behavior (in a single reciprocal lattice direction) of both `cold` and `hot` graphite either side of the melting point. Below the melt point the forces between the graphite layers are determined by the delocalization of the single free electron per carbon atom creating the weak inter-planar π-bonds. By choosing the screening length to be $\lambda_D = a/2$ the melt point of the model can be matched to that of graphite [21]. At temperatures above the melt point and while ionization remains low the Thomas-Fermi [22] screening model also produces a value very close to $\lambda_D = a/2$. Hence the screened Coulomb potential is suitable for the temperatures considered.

Large-scale molecular dynamic simulations were run with the LAMMPS MD package [23] using 20000 ions at several temperatures above and below the melt point. In each case the simulation was initiated in a lattice configuration at t=0, then allowed to equilibrate for $1000(1/\omega_{pi})$ with a time step $\Delta\tau = 0.005(1/\omega_{pi})$ during which time temperature rescaling was used to maintain the temperature. ω_{pi} is the ion plasma frequency. It was ensured that in all cases the system reached an equilibrium state before performing calculations of the structure factor for a further $1000(1/\omega_{pi})$ in the microcanonical ensemble. These results are shown in *figure 1*. The change in the static structure factor for various temperatures is shown in *figure 2* for two different k values. The value of the structure factor for $k=k_{Bragg}$ at low T approaches Eq. (5) which for an infinite perfect crystal ($N\rightarrow\infty$) is a Dirac-delta function. However for any finite crystal the actual maximum value is given by the fourier transform of a top hat function (a *sinc* function) describing the extent of the crystal. The relative intensity between two temperatures however is not affected since this analysis was done at constant volume.

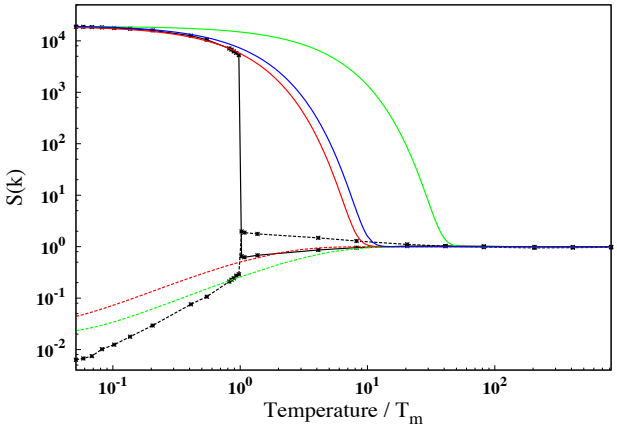

Figure 2. Bragg Intensity vs Ion Temperature from MD simulation (black lines), DW theory `cold` T_D=950K (green lines), DW theory using Eq. (7) T_D=677K (blue lines) and DW theory `fitted` T_D=620K (red lines). Produced at $k=k_{Bragg}$ (solid lines) and $k=(3/4)k_{Bragg}$ (dashed lines).

Table 1. Comparison between MD results and DW theory for different values of the Debye temperature, T_D.

Method	T_D	$S_{MD}/S_{DW}(0.5T_M)$	$S_{MD}/S_{DW}(0.9T_M)$
Cold Graphite	950K	0.75	0.5
Equation (7)	677K	0.94	0.78
Fitted function	620K	1.02	0.92

Of interest to this work is the reduction in the Bragg scattering (solid lines) with increased temperature. *Table 1* shows the ratio between the DW theory and the MD results at 50% and 90% of the melt temperature. The discrepancy between the two is clearly apparent when T_D is set to 950 K [24] the graphite inter-plane solid state value. This high T_D models a crystal with stronger and more rigid bonds than seen in the MD simulation, this is the source of the increased structure factor at high T. Using a higher value for T_D=677 K obtained from Eq. (7) the discrepancy between the models can be reduced and at 90% of T_m there is an improvement from 0.5 to 0.78 in the structure factor ratio. If the model is fitted to the data a slightly lower Debye temperature of T_D=620 K is obtained leading to an even better agreement between the two models. The improvement seen in *Table 1* shows the degree to which the DW theory can capture the ion behavior at ion temperatures up to T_m given the correct value for the Debye temperature. The small difference when T=0.9T_M can be attributed to the motion of the ions no longer being described within the harmonic approximation of equation (6). This inconsistency can be reduced at these high temperatures by modifying the underlying assumptions of the DW factor and including additional anharmonic terms. This additional terms are neglected here due to the uncertainty already present in the experimental results.

It is interesting to note the increase in scattering at angles not equal to the Bragg angle i.e. $k \neq k_{Bragg}$. This is shown in *figure 2* by the dashed lines. Scattering at these angles is known as thermal diffuse and represents incoherent scattering from the thermal motion of the ions (phonons) and to first order represents the density of states of the phonons [18]. As this scattering has a smaller cross section it can be neglected in this analysis of the coherent Bragg scattering.

3. Experimental temperature inference in warm dense HOPG

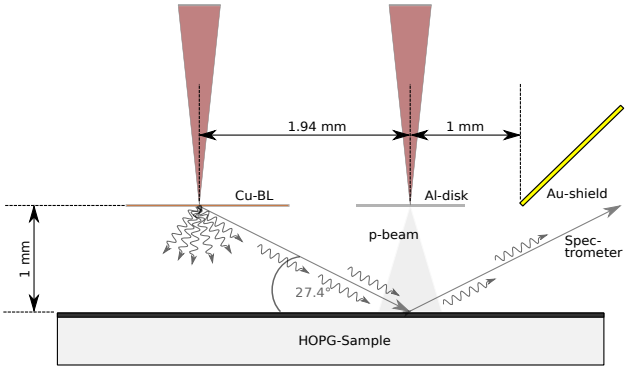

Figure 3. A schematic of the experimental setup used on the Titan Laser at the Jupiter Laser Facility, Lawrence Livermore National Laboratory (USA).

In this section we will describe an experiment performed at the Titan Laser at the Jupiter Laser Facility, LLNL (see Fig 3). The 150 J, 10 ps long Titan west beam (at the fundamental frequency λ_0=1054 nm) was split into two arms in a 30/70 pump-probe configuration. To heat the graphite sample 30% of the energy was focused onto a thin aluminum foil creating an intense proton beam through the Target Normal Sheath Acceleration (TNSA) mechanism [24,25]. The remaining energy was focused 225 ps later onto a copper disk to create an intense Cu-Kα 8 keV x-ray probe. An image plate was placed 300 mm away from the graphite sample at 27.4° to detect the Bragg diffracted light. The magnification of the setup was 138.

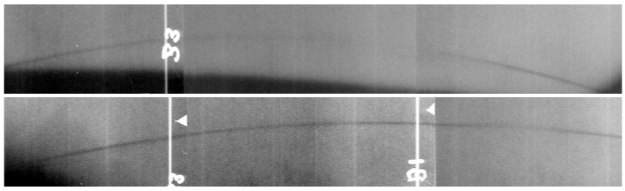

Figure 4. Bragg scattering signal on image plate from proton heated (top) and unheated (bottom) sample.

The proton beam forms a spot size of ~0.5 mm on the sample, which is magnified to 75 mm onto the image plate detector. The sample consisted of 50 μm thick HOPG covered with 15 or 30 μm of plastic (PP), increasing the purity of the proton beam reaching the sample and stopping low energy protons. This helps to achieve a more homogeneous heating of the sample. The thickness of 50 μm for the HOPG sample was chosen to be considerably less than the penetration depth of the expected protons (up to 1000 μm) and of the Cu-Kα radiation (1285 μm). This ensures total heating of the sample and prevents unheated regions being probed. *Figure 4* shows an example of two image plates from an unheated and heated sample. The heated area is clearly visible through a reduction in the Bragg peak. By integrating the intensity of scattered radiation along the Bragg scattering signal and normalizing to the cold scattering signal either side of the heated region we used the model developed above using T_D=620K to infer the temperature of the ions.

In order to validate our temperature diagnostics we have also compared our measurements with the predicted heating from the proton beam [25, 26, 27]. This was done by assuming that the laser produced protons with a Boltzmann-like distribution of the form,

$$\frac{dN}{dE} = \frac{A}{E^{\frac{1}{2}}} exp\left(-\left(\frac{2E}{T_p}\right)^{\frac{1}{2}}\right) \qquad E < E_{max}\,, \tag{9}$$

with the proton temperature T_p≈0.5 MeV, a cutoff energy of E_{max}≈15 MeV and a conversion efficiency of 0.16% for protons with energy greater than 4 MeV. A linear relationship between E_{max} and angle was used to approximate the spatial dependence of the beam, as suggested in ref. [27].

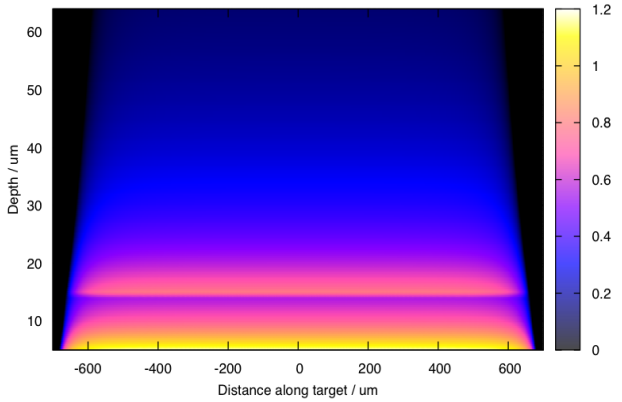

Figure 5. Target temperature (eV) approximated from the theoretical proton spectrum from ref [26] and the known stopping power of PP and graphite [28].

From the assumed proton distribution and its spatial variation using the known stopping power in cold PP and graphite the estimated deposited energy at a given depth in the sample was calculated. An example for 15 μm of PP is given in *figure 5* with the resulting heating profiles shown for the different cases in *figure 6. Figure 6* also shows the temperatures obtained for three different shots using the DW theory for 15 μm of PP (a), 30 μm of PP (b) and no proton beam (c). The similarity between the temperatures obtained using the theoretical spectrum and those obtained using the DW theory coupled with the experimental results is promising. Further analysis of the proton spectrum using RCF and proton spectrometers present at the experiment should allow for improvement between the predicted and the measured temperatures in the sample. This analysis should help to evaluate the validity of the spatial features of the heated sample present in our results.

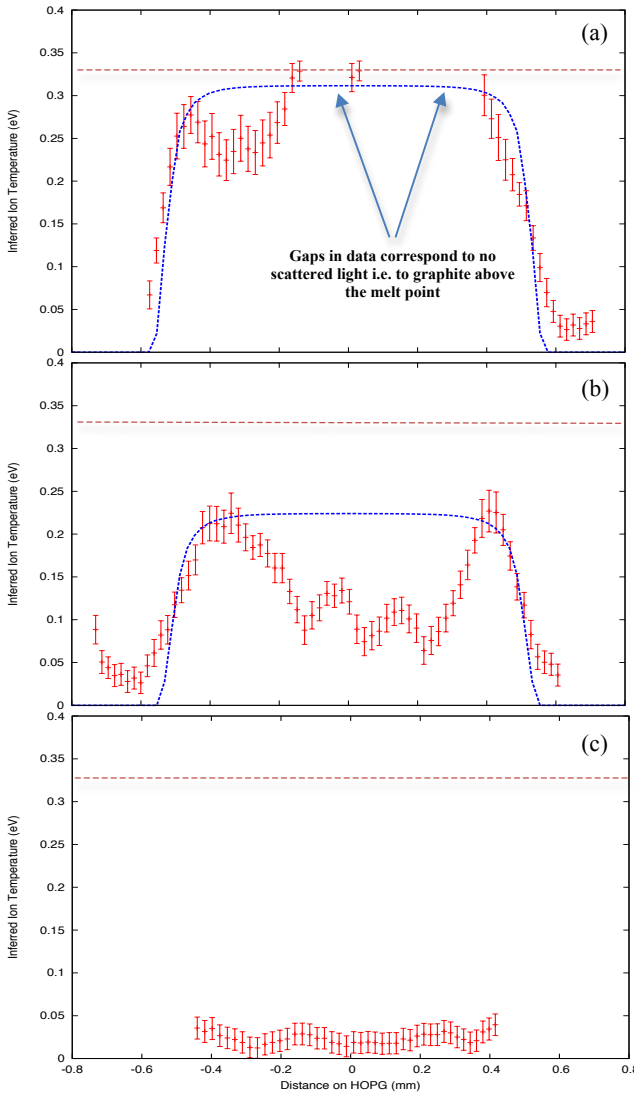

Figure 6. Inferred ion temperature from the DW model (red lines) and expected temperature from the theoretical proton spectrum (blue lines) for 15 μm of PP (a), 30 μm of PP (b) and no heating (c). The red dashed line indicates the equilibrium melt temperature of graphite ~0.33 eV.

Conclusions

In this report we present an overview of the Debye-Waller (DW) technique to characterize the displacement of atoms in a crystal from the equilibrium positions. We show how within the harmonic approximation this displacement can be linked to the ion temperature through eq. (6) provided that T_D is known. Using a classical simulation we have shown that when a fitted T_D is used the DW theory agrees with MD simulation extremely well up to 90% of the melt temperature, T_m. However when using the solid state result we obtained a large (~50%) discrepancy at these higher temperatures. We also showed that for temperatures below $0.5T_m$ using the value of T_D obtained from the the Bohm-Staver relation (7) is also comparatively accurate (<5%).

Finally we evaluate the validity of this technique through experimental results in an equilibrium system by inferring the ion temperature in warm dense graphite (HOPG) and have shown that the results obtained from the DW theory compare favorably with an approximate proton spectrum and known energy deposition in graphite.

Acknowledgements

The work in this report was supported by funding from AWE. The author would also like to thank all the staff at the Jupiter Laser Facility, LLNL for their support.

References

[1] J. Daligault and S. Gupta, Astrophys.J. 703, 994 (2009).

[2] M. Matzen, M. Sweeney, R. Adams, and J. Asay, Physics of Plasmas (2005).

[3] R. Drake, High-energy-density physics, fundamentals, inertial fusion, and experimental astrophysics (Springer Verlag, 2006).

[4] R. Davidson, D. Arnett, J. Dahlburg, and P. Dimotakis, Frontiers in high energy density physics (Frontiers, 2002).

[5] R. Drake, Physics Of Plasmas 16, 055501 (2009).

[6] G. Gregori and D.O. Gericke. Physics Of Plasmas. 16, 5 (2009)

[7] C.W. Siders, Science 286, 1340 (1999).

[8] A. M. Lindenberg, Science 308, 392 (2005).

[9] R. Ernstorfer et al, Science 323, 5917 (2009) .

[10] S.H. Glenzer and R. Redmer, Reviews Of Modern Physics 81, 1625 (2009).

[11] P. Patel et al, Physical Review Letters 91, 12, (2003).

[12] A. Mancic et al, High Energy Density Physics 6, 21 (2010).

[13] G.M. Dyer et al, Physical Review Letters 101, 1, (2008).

[14] T.H. Metzger, Journal of Applied Crystallography 19, 200 (1986).

[15] J.P. Hansen and I. R. McDonald, Theory of Simple Liquids, Third Edition, 3rd ed. (Academic Press, 2006).

[16] G. Gregori, S. Glenzer, W. Rozmus, R. Lee, and O. Landen, Physical Review E 67, 026412 (2003).

[17] G. Gregori, S. H. Glenzer, and O. L. Landen, Physical Review E 74, 026402 (2006).

[18] J. Als-Nielsen, Elements of Modern X-Ray Physics (Wiley, John & Sons, Incorporated, 2001).

[19] R. Mossbauer and W. Wiedemann. Kernresonanzabsorption Nicht Doppler-Verbreiterter Gammastrahlung in Re-187. Z Phys. 159, 1 (1960).

[20] G. Gregori et al, High Energy Density 3, 99 (2007).

[21] S. Hamaguchi, R. Farouki, and D. Dubin, Physical Review E 56, 4671 (1997).

[22] D. Salzmannn, Atomic Physics in Hot Plasmas (Oxford University Press, 1998)

[23] http://lammps.sandia.gov/

[24] W. DeSorbo, The Specific Heat of Graphite from 13° to 300°K. J. Chem. Phys. 21, 1660 (1953).

[25] P. Mora, Plasma Expansion into a Vacuum. Physical Review Letters. 90, 18 (2003).

[26] J. Fuchs et al, Laser-driven proton scaling laws and new paths towards energy increase. Nat Phys. 2, 48–54. (2006).

[27] F.Nuernberg, M. Schollmeier, E. Brambrink, et al. Radiochromic film imaging spectroscopy of laser-accelerated proton beams. Rev Sci Instrum. 80, 3 (2009)

[28] http://physics.nist.gov/PhysRefData/Star/Text/PSTAR.html

A new VFP-PIC hybrid code to model fast electron transport with hydrodynamic response

Contact *brennig.williams08@imperial.ac.uk*

B. E. R. Williams and R. J. Kingham
Imperial College of Science Technology and Medicine
London, SW7 2AZ

Introduction

The interaction of a high-intensity laser beam with a solid target generates a large number of fast-electrons with long mean free paths. The study of these fast-electrons is still the subject of active research, given their relevance to Tabak's proposed fast-ignition (FI) approach to inertial confinement fusion [1]. Modelling of these electrons from the region in which they are generated to the dense fuel core is not a trivial task given the range of plasma conditions experienced by the electrons.

Conventional methods for simulating this FI system fall into two categories: kinetic and hybrid codes. Kinetic codes, such as Vlasov Fokker-Planck (VFP) and Particle in Cell (PIC) codes, provide an almost complete description of the system, but are often computationally expensive and have strict constraints on the time-step. Thus, these codes can struggle to model picosecond timescales when hydrodynamics of the background is expected to be significant. VFP codes work best in collision-dominated plasmas. As for PIC codes, there is some debate about their ability to reproduce the results of classical transport theory, which can play a significant role in beam-plasma systems. Furthermore, PIC codes can struggle to accurately represent the fast-electron beam in a solid density background as most of the particles in a cell will be used to model the background.

Hybrid codes [2] often consist of a PIC code, which accurately models the fast-electrons, and a simple fluid code to model the response of the background. While hybrid codes are computationally light, the description of the background is often rudimentary. This reduced description of the background allows probing of longer time-scales and larger spatial-scales. This description of the background is sometimes as simple as

$$\mathbf{E} = \eta \mathbf{j}$$

where η is the Spitzer resistivity. However, η should be a tensor when magnetic fields are present [3]. Also this simple treatment neglects many terms present in the full Ohm's law. More advanced hybrid codes still rely on the fluid treatment of the background plasma. However this treatment is only valid in the case of Maxwellian background distribution functions and also in the absence of steep number density and temperature gradients. Both non-Maxwellian distributions and steep gradients are expected to be present in fast ignition scenario.

Novel Hybrid Code

We present a new approach to modeling fast ignition type scenarios. This novel hybrid code offers a good description of the fast-electrons (PIC), and an improved description of the background (VFP) compared to conventional hybrid codes. The VFP code used (IMPACT [4]) is suited to describing magnetized transport in the presence of steep temperature and number density gradients. Furthermore, it can model magnetic field generation and includes the displacement current in Ampere's law. IMPACT solves the VFP equation by making use of a Cartesian tensor expansion in velocity space

$$f = f_0 + \mathbf{f}_1 \cdot \frac{\mathbf{v}}{v} + \ldots$$

In order to truncate this expansion, IMPACT utilises the diffusion approximation, which neglects terms in *f* of higher order than 1. This approximation is valid for a collisional plasma, and limits the hybrid approach to systems with small beam to background ratios (just as in a conventional hybrid code). The PIC code and VFP code are linked via their current contributions to Ampere's law.

Filamentation instability

To test the VFP-PIC interaction we considered the filamentation instability in a 1d2*v* system. The mechanism for this instability is essentially a feedback between the generation of a magnetic field due a transverse perturbation of the beam current, and the enhancement of this current due to the Lorentz force of the perturbed magnetic field [5]. Due to the novel set up of the hybrid scheme it was necessary to derive a dispersion relation in the VFP-PIC system. We used the approach of Epperlein [6] as a template. We consider the distribution function of the background electrons to be a shifted Maxwellian evolving under the f_0 and f_1 equations. The beam electrons are initially monokinetic with velocity v_h and evolve under the collisionless Vlasov equation. Considering wavelike perturbations, and using Ampere's law and Faraday's law we find a cubic dispersion relation of the form given in figure

$$\sum_{i=0}^{3} a_i \gamma^i = 0$$

where

$$a_0 = (\omega_h \tau_{th})^2 v_h^2 k^4$$

$$a_1 = 0$$

$$a_2 = -(\omega_h \tau_{th})^2 k^2 - k^4 c^2$$

$$a_3 = 12\pi k^2 (\omega_c \tau_{th})^2 \int \partial_v f_0^0 v^6 dv \quad ,$$

and γ is the growth rate, k is the wavenumber of the instability, ω_h is the hot electron plasma frequency, ω_c is the background electron plasma frequency, τ_{th} is the collision time of a thermal electron in the background, f_0^0 is the initial isotropic part of the distribution function for the background electrons. The real parts of the roots of the above cubic are shown in figure 1 for a system with a beam to background ratio of 0.01, $v_h = 10\ v_{th}$, where v_{th} is the thermal velocity in the background, with the background at a temperature of 50 eV and an electron density of and $5*10^{21}$ /cm^3.

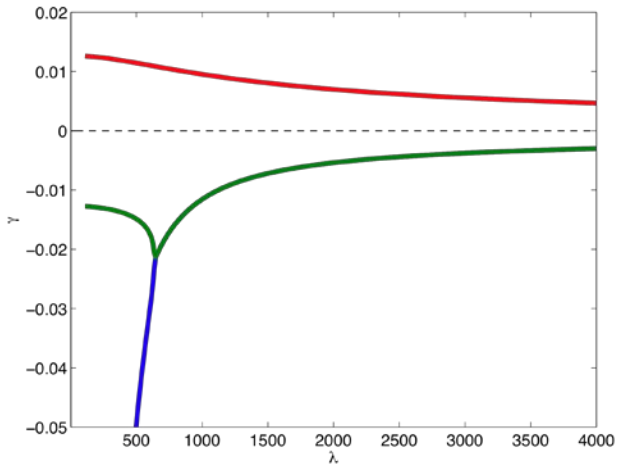

Fig. 1: Real part of roots of the dispersion relation. Wavelength is normalized to the thermal electron mean free path, and the growth rate is normalized to the collision frequency for a thermal electron.

As we are considering the growth of the instability, we consider the positive real part. We see that at low wavelengths, the growth rate is saturated as the generation of the perturbed magnetic field is balanced by the resistive diffusion of the field. At larger wavelengths the growth rate tends to zero due to the decrease in the magnitude of the perturbed magnetic field (generated by the curl of the total current). As IMPACT utilises the diffusion approximation, it is useful to consider the effect of including f_2 in the background. The first order correction to the dispersion relation is plotted in figure 2. We see that the contribution of f_2 to the growth rate is only significant for background drift speeds greater than the thermal velocity. We see also that this contribution is greatest for low wavelength perturbations. This is due to the increased importance of collisionless phenomena in the background for wavelengths close to the mean free path of a thermal electron. The agreement of the two models for $\lambda < 100$ is due to lack of higher order anisotropic terms in the model.

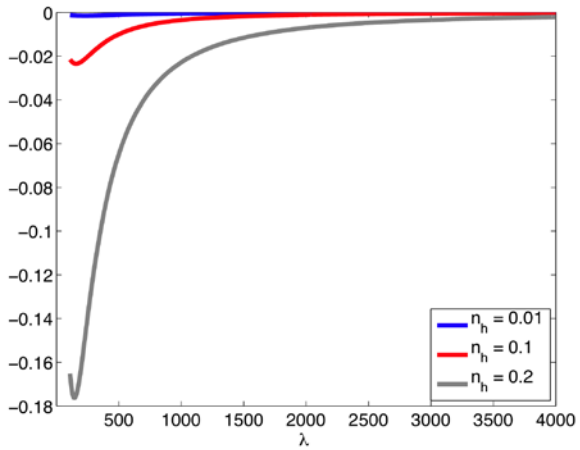

Fig. 2: Fractional difference between growth rates without and with f_2 contribution for beam to background ratios of 0.01 (blue), 0.1 (red), and 0.2 (grey).

Code comparison

Figure 3 shows the dispersion relation predicted by theory and by the hybrid code for the system parameters mentioned above. The growth rate for an initial perturbation of 0.1% differs from theory by less than 20%, and the growth rate for the smaller perturbation of 0.0001% differs by less than 10%. The smaller the perturbation the closer the instability resembles the linear analysis, as expected. This test confirms that the PIC and VFP codes interact correctly.

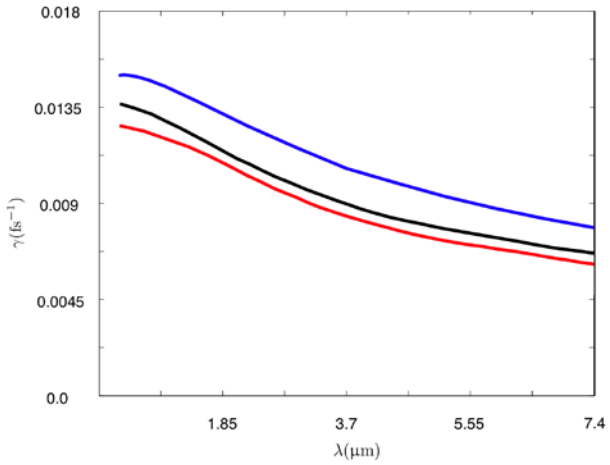

Fig. 3: Comparison of the growth rates predicted by the code with a 0.1% initial perturbation (blue), with a 0.0001% initial perturbation (black), to the growth rate predicted by the linear instability analysis (red).

Conclusions and Future work

We have constructed a novel VFP-PIC hybrid code to study fast electron transport in fast-ignition type scenarios. A linear theory of the filamentation instability has been developed to test the interaction of the VFP and PIC codes. A good agreement has been found for the dispersion relations predicted by the code and by the linear theory.

The inclusion of hydrodynamic response in IMPACT makes the hybrid code well suited to study fast electron transport on picosecond timescales. We hope to offer an improved description on phenomena such the as re-collimation effects of the fast-electron beam due to PdV cooling in the background plasma [7],[8].

References

1. Tabak M *et al*, Phys. Plasmas **1** 1626A (1994)
2. Davies J R *et al*, Phys. Rev. E **59** 6032 (1999)
3. Braginksii, *Reviews of Plasma Physics* (Constants Bureau, NY) **1**, 201 (1965)
4. Kingham R. J. & A. R. Bell, J. Comp. Phys. **194** (2004)
5. Fried B. D., Phys. Fluids **2**, 337 (1959)
6. Epperlein E. M., Plas. Phys. Contr. Fusion **27**, 9 (1985)
7. Kingham R J *et al*, J. Phys. Conf. Ser. **244** 022042 (2010)
8. Bush I A *et al*, Plasma Phys. Control. Fusion **52** 125007 (2010)